R&D aspects of cryogenic bolometer development for neutrinoless double beta decay search in ^{124}Sn

By

Abhijit Garai

PHYS01201404008

Bhabha Atomic Research Centre, Mumbai–400 085

A thesis submitted
to the Board of Studies in
Physical Sciences

In partial fulfillment of requirements
For the Degree of

DOCTOR OF PHILOSOPHY
of
HOMI BHABHA NATIONAL INSTITUTE

March, 2019

Homi Bhabha National Institute

Recommendations of the Viva Voce Committee

As members of the Viva Voce Committee, we certify that we have read the dissertation prepared by Abhijit Garai entitled “R&D aspects of cryogenic bolometer development for neutrinoless double beta decay search in ^{124}Sn" and recommend that it may be accepted as fulfilling the thesis requirement for the award of Degree of Doctor of Philosophy.

Chairman - Dr. G. Ravikumar **Date:**

Guide / Convener - Prof. V. Nanal **Date:**

Examiner - Dr. V. Ganesan **Date:**

Member 1 - Prof. S. Ramakrishnan **Date:**

Member 2 - Prof. R. G. Pillay **Date:**

Member3 - Dr. K. Dasgupta **Date:**

Final approval and acceptance of this thesis is contingent upon the candidate’s submission of the final copies of the thesis to HBNI.

I hereby certify that I have read this thesis prepared under my direction and recommend that it may be accepted as fulfilling the thesis requirement.

Date:

Place: **Prof. V. Nanal (Guide)**

STATEMENT BY THE AUTHOR

This dissertation has been submitted in partial fulfillment of requirements for an advanced degree at Homi Bhabha National Institute (HBNI) and is deposited in the library to be made available to borrowers under rules of the HBNI.

Brief quotations from this dissertation are allowable without special permission, provided that accurate acknowledgement of source is made. Requests for permission for extended quotation from or reproduction of this manuscript in whole or in part may be granted by the Competent Authority of HBNI when in his or her judgment the proposed use of the material is in the interests of scholarship. In all other instances, however, permission must be obtained from the author.

Abhijit Garai

DECLARATION

I hereby declare that the investigation presented in the thesis has been carried out by me. The work is original and has not been submitted earlier as a whole or in part for a degree/diploma at this or any other Institution/University.

Abhijit Garai

List of Publications arising from the thesis

Publications in Refereed Journal

Published

1. Development of NTD Ge Sensors for Superconducting Bolometer, **A. Garai**, S. Mathimalar, V. Singh, N. Dokania, V. Nanal, R. G. Pillay, S. Ramakrishanan, A. Shrivastava, K. C. Jagadeesan. S. V. Thakare, Journal of Low Temp. Phys. **184** (2016) 609.

2. Specific heat of Teflon, Torlon-4203 and Torlon-4301 in the range of 30 - 400 mK, V. Singh, **A. Garai**, S. Mathimalar, N. Dokania, V. Nanal, R. G. Pillay, S. Ramakrishnan, Cryogenics **67** (2015) 15.

Communicated

1. Study of the effect of external noise pickups on the performance of a cryogenic bolometer, A. Garai, A. Reza, A. Mazumdar, H. Krishnamoorthy, G. Gupta, V. Nanal, R. G. Pillay, and S. Ramakrishnan, arXiv:1908.00002 (Submitted to RSI).

2. Systematic studies of a sapphire bolometer with phonon pulses in the temperature range of 10-100 mK A. Garai, A. Mazumdar, A. Reza, H. Krishnamoorthy, G. Gupta, V. Nanal, R. G. Pillay and S. Ramakrishnan (Submitted to JLTP).

Others

1. New limit for the half-life of double beta decay of ^{94}Zr to the first excited state of ^{94}Mo, N. Dokania, V. Nanal, G. Gupta, S. Pal, R. G. Pillay, P. K. Rath, V. I. Tretyak, **A. Garai**, H. Krishnamoorthy, C. Ghosh, P. K. Raina and K. G. Bhushan, Eur. Phys. J. **A 53** (2017) 74.

2. Estimation of low energy neutron flux (E_n ≤15 MeV) in India-based Neutrino Observatory cavern using Monte Carlo techniques, N. Dokania, V. Singh, S. Mathimalar, **A. Garai** , V. Nanal, R. G. Pillay and K. G. Bhushan, Journal of Instrumentation **10** (2015) T12005.

Proceedings

1. A pulse height analysis technique for cryogenic bolometers, **A. Garai**,

A. Mazumdar, A. Reza, H. Krishnamoorthy, G. Gupta, V. Nanal, R. G. Pillay, Proceedings of the DAE-BRNS International Symp. on Nucl. Phys. **63** (2018) 1140.

2. The neutron induced γ-ray background in ^{124}Sn, G. Gupta, H. Krishnamoorthy, **A. Garai**, A. Mazumdar, V. Nanal, A. Shrivastava, R.G. Pillay, Proceedings of the DAE-BRNS International Symp. on Nucl. Phys. **63** (2018) 232.

3. Design and development of a front-end preamplifier for bolometric detector, A. Reza, **A. Garai**, A. Mazumdar, V. Vatsa, H. Krishnamoorthy, G. Gupta, M.S. Pose, S. Mallikarjunachary, V. Nanal, R.G. Pillay, Proceedings of the DAE-BRNS Intl. Symp. on Nucl. Phys. **63** (2018) 1124.

4. Modeling of an electrically cooled HPGe detector, G. Gupta, H. Krishnamoorthy, **A. Garai**, A. Mazumdar, A. Reza, V. Nanal, R.G. Pillay, Proceedings of the DAE-BRNS International Symp. on Nucl. Phys. **63** (2018) 1142.

5. Muon Induced Neutron measurement setup at TIFR (MINT), H. Krishnamoorthy, G. Gupta, **A. Garai**, A. Mazumdar, A. Reza, S. Pal, V. Nanal, R.G. Pillay, A. Shrivastava, Proceedings of the DAE-BRNS International Symp. on Nucl. Phys. **63** (2018) 1146.

6. Assessment of borated rubber for neutron shield, H. Krishnamoorthy, G. Gupta, **A. Garai**, A. Mazumdar, S. Pal, V. Nanal, R.G. Pillay, A. Shrivastava, Proceedings of the DAE-BRNS International Symp. on Nucl. Phys. **63** (2018) 1148.

7. Radiopurity studies of tin-lead and tin-bismuth alloys for the development of a cryogenic bolometer, A. Mazumdar, G. Gupta, **A. Garai**, H. Krishnamoorthy, A. Reza, V. Nanal, R. G. Pillay, A. Shrivastava, A. Thamizhavel, Proceedings of the DAE-BRNS International Symp. on Nucl. Phys. **63** (2018) 1152.

8. Radiopurity studies of indium-doped tin alloys for TIN.TIN, A. Mazumdar, G. Gupta, J. Raval, **A. Garai**, H. Krishnamoorthy, V. Nanal, R.G. Pillay, A. Shrivastava, A. Thamizhavel, R. Mondal, Proceedings of the DAE-BRNS Symp. on Nucl. Phys. **62** (2017) 1118.

9. Radiopurity Study of CsI and CsI(Tl) detectors for the mini-DINO, G. Gupta, H. Krishnamoorthy, **A. Garai**, A. Mazumdar, V. Nanal, R.G. Pillay, S. Saha, S. Ghosh, S.G. Singh, Shashwati Sen, S.C. Gadkari, Proceedings of the DAE-BRNS Symp. on Nucl. Phys. **62** (2017) 998.

10. Study of radioactive impurities in NTD Ge sensors for mK thermometry, **A. Garai**, G. Gupta , H. Krishnamoorthy, N. Dokania, V. Nanal, R. G. Pillay , A. Shrivastava , K.C. Jagadeesan and S.V. Thakare, Proceedings of the DAE-BRNS Symp. on Nucl. Phys. **61** (2016) 1068.

11. Estimation of Neutron flux in TIFR Low background Experimental Setup (TiLES), Harisree Krishnamoorthy, **A. Garai**, G. Gupta, N. Dokania, V. Nanal, R. G. Pillay and A. Shrivastava, Proceedings of the DAE-BRNS Symp. on Nucl. Phys. **61** (2016) 1014.

12. Improvements to Tifr Low background Experimental Setup (TiLES),G. Gupta, N. Dokania, H. Krishnamoorthy, **A. Garai**, C. Ghosh , M. S. Pose,

V. Nanal and R.G. Pillay, Proceedings of the DAE-BRNS Symp. on Nucl. Phys. **61** (2016) 1026.

Abhijit Garai

DEDICATED TO

My family and friends

ACKNOWLEDGEMENTS

I would like to thank my supervisor Prof. Vandana Nanal for constant guidance and help. I appreciate the amount of time devoted by her to the research work and the attention paid in every little details. Her enthusiasm, energy and positive outlook towards life and work kept me going throughout the course of my Ph.D. I express my deepest gratitude to Prof. R. G. Pillay for his in depth insights and suggestions. I admire his love towards experimental physics and his passion in indigenous developments. He inspired me to think critically and have systematic approach towards solving any problem. I would like to thank the members of my doctoral committee - Dr. G. Ravikumar, Prof. S. Ramakrishnan, Prof. R. G. Pillay and Dr. K. Dasgupta for keeping track of my progress and feeding key inputs for the improvement of the thesis. Experimental work is never easy without a tireless effort of a group of encouraging lab mates. I am deeply grateful to Dr. Vivek Singh who had been a senior, lab mate, friend, mentor for me when I joined the lab. Also, I would like to thank Dr. S. Mathimalar and Dr. Neha Dokania for being inspirational seniors in the lab during the initial phase of my Ph.D and guiding me throughout the course of work. I had a enjoyable time while discussing exotic physics ideas with Chandan Ghosh. His company in lab was very delightful for me. I thank all my junior colleagues in the group- Aparajita Majumdar, G. R. Gupta, Harisree Krishnamoorthy and Vishal Vasta for their time to time help in the experiments. I would like to thank Dr. Ashif Reza for his valuable suggestions and consistent help during the experiments. I am very thankful to Mr. S Mallikarjunachary, Mr. M. Pose, Mr S. Pal, Mr. J. N. Karande, Ms. P. S. Dhumal, Mr. M. Sawant, Mr. A. Shinde, Mr. Abdul Q. Momin, Mr. L. V. Kamble and all other PLF LINAC staff for their support and help in setting up the experiment. They all were always available as helping hands during the experiment even on a very short notice. Thanks to Mr. Anil Kumar, Prof. M. Deshmukh, Prof. S.S. Prabhu, Prof. A. Bhattacharya, Prof. A Thamizhavel and their lab staff for assistance during the sensor fabrication. I thank Dr. A. Shrivastava, Mr. K. C. Jagadeesan. Mr. S. V. Thakare, Dhruva reactor staff and NPD, BARC for helping with the neutron irradiations of Ge. I wish to express my gratitude to all the teachers who taught me during my course work at TIFR - Prof. G. Majumdar, Prof. S. Datta, Prof. S. Umasankar, Prof. S. Banerjee, Prof. N. K. Mondal, Dr. B. Satyanarayana, Mr. K.V. Srinivasan, Mr. K. S. Gothe and Mr. S. Upadhya. I thank Prof. V. Datar whose interest and positive thinking for my thesis was very captivating for me. I would like to thank Yuvaraj, Dipankar, Pathaleswar, T. T. S. Singh, M. Saraf, Nagaraj P, Pavan Kumar and R.R. Shinde for their support. Thanks to my colleagues Apoorva Bhatt, Md. Nizam, Divya Divakaran and Manas Kumar Khatua with whom I had fruitful discussions during the course work. I wish to thank my friends Aman and Archana who made my early days at TIFR a memorable experience. Special thanks to my friend Neha for her constant support, continuous encouragement, motivation and help throughout the process of research and writing this thesis. Last but not the least, I thank my family members for their unconditional love and support which kept me determined.

Contents

List of Figures

List of Tables

List of Abbreviations

α	Alpha
β	Beta
γ	Gamma
still	^{3}He distiller
ADC	Analog to Digital Converter
AMoRE	Advanced Mo based Rare process Experiment
AuGe	Germanium,Compound with gold(1:1)
CDMS	Cryogenic Dark Matter Search
CFDR	Cryogen Free Dilution Refrigerator
CMN	Cerium Magnesium Nitrate
COSINUS	Cryogenic Observatory for SIgnatures seen in Next-generation Underground Searches

Co	Cobalt
CRESST	Cryogenic Rare Event Search with Superconducting Thermometers
CUORE	Cryogenic Underground Observatory for Rare Events
CUPID	CUORE Upgrade with Particle IDentification
DAC	Digital to Analog Converter
DAQ	Data Acquisition
DBD	Double Beta Decay
DM	Dark Matter
EDELWEISS	Experiment for direct detection of WIMP dark matter
EMI	Electro Magnetic Interference
FFT	Fast Fourier Transform
FPD	Fixed Point Device
GERDA	Germanium Detector Array
Ge	Germanium
GHS	Gas Handling System
GM cooler	Gifford-McMahon cooler
HBNI	Homi Bhabha National Institute
He	Helium
HPGe	High Pure Germanium

IH	Inverted Hierarchy
IVC	Inner Vacuum Chamber
JUNO	Jiangmen Underground Neutrino Observatory
KamLAND	Kamioka Liquid Scintillator Antineutrino Detector
KIDS	Kinetic inductance detectors
Li	Lithium
LNGS	Gran Sasso National Laboratory
LUCIFER	Low-background Underground Cryogenic Installation For Elusive Rates
LUMINEU	Luminescent Underground Molybdenum Investigation for NEUtrino mass and nature
MC	Mixing Chamber
MeV	Mega Electron Volt
MKID	Microwave Kinetic Inductance Detector
MMC	Magnetic Calorimeters
NbTi	Niobium Titanium
NDBD	Neutrinoless Double Beta Decay
NH	Normal Hierarchy
NI	National Instruments
NOVA	NuMI Off-axis ν e Appearance

NTD	Neutron Transmutation Doping
NTME	Nuclear Transition Matrix Element
OVC	Outer Vacuum Chamber
PCB	Printed Circuit Board
PID	Proportional-Integral-Derivative
PMNS	B. Pontecorvo, Z.Maki, M. Nakagawa and S. Sakata
Po	Polonium
PT	Pulse tube cooler
PXI	PCI extensions for Instrumentation
R&D	Research and Developement
Ref	Reference
ROI	Region of Interest
RuO_2	Ruthenium dioxide
Sb	Antimony
SMD	Surface Mount Devices
SM	Standard Model
SSP	Single Side Polish
STJ	Superconductive Tunnel Junctions
T2K	Tokai to Kamioka

TeO_2	Tellurium dioxide
TES	Transition Edge Sensors
TIFR	Tata Institute of Fundamental Research
TiLES	TIFR Low background Experimental Setup
Tin.Tin	The India-based Tin detector
TiO_2	Titanium dioxide
VRH	Variable Range Hopping
Y2L	Yangyang Underground Laboratory
Zr	Zirconium

Synopsis

Neutrino is a chargeless lepton in the standard model of elementary particles and interacts only via weak interaction. Understanding the properties of neutrinos has been one of the prime interests in the field of nuclear and particle physics research. Neutrinos exist in three different flavors: electron neutrinos (ν_e) muon neutrinos(ν_μ) and tau neutrinos (ν_τ), associated with the respective charged leptons. Experiments in recent years have conclusively shown that neutrinos oscillate in the flavor states implying that neutrinos have a non-zero finite mass [1, 2]. However, it should be noted that from the neutrino oscillation data only the differences in mass squares can be extracted. The absolute mass and the true nature of neutrinos, i.e. whether neutrino and antineutrino are same (Majorana particle) or different (Dirac particle), is still an open question. This has long standing implications in understanding matter-antimatter asymmetry and can also be important for explaining the smallness of the neutrino mass.

The Double beta decay (DBD) is a second order spontaneous nuclear transition where a nucleus (A,Z) decays to an isobar (A,Z+2) by emitting two electrons along with two antineutrinos.

$$(A, Z) \rightarrow (A, Z + 2) + 2e^{-} + 2\bar{\nu}_e$$

The DBD is favoured when the single beta decay is energetically forbidden or spin forbidden. If the neutrinos are Majorana particles, there is a finite probability that neutrinos virtually annihilate each other leading to a neutrinoless double beta decay (NDBD or $0\nu\beta\beta$). The decay rate, i.e. the inverse of the half-life of the NDBD process is given by Equation 1 as,

$$(T_{1/2}^{0\nu})^{-1} = G_{0\nu}(Q_{\beta\beta}, Z)|M_{0\nu}|^2 < m_{\beta\beta} >^2 \tag{1}$$

where $G_{0\nu}(Q_{\beta\beta}, Z)$ is the phase space factor, $M_{0\nu}$ is the nuclear transition matrix element (NTME) and $m_{\beta\beta}$ is the effective Majorana mass of the electron neutrino [3]. At present, NDBD is perhaps the only viable experiment, which can reveal the true nature of neutrino and also measure the absolute effective mass of neutrino. A peak at the Q value in the sum energy spectrum of the two electron would be an experimental signature of the NDBD process. If the peak is observed after a measurement time t $<< T_{1/2}^{0\nu}$ the half-life can be expressed as

$$T_{1/2}^{0\nu} = \frac{iN_A M t \epsilon}{A N_{0\nu\beta\beta}} \tag{2}$$

where $iN_A M/A$ equates to the number of parent atoms in the source material of mass M having isotopic abundance i, N_A is the Avogadro number, ϵ is the detector efficiency and $N_{0\nu\beta\beta}$ is the number $0\nu\beta\beta$ events observed. If no peak is observed a lower limit on the half-life can be placed depending on the background fluctuation at the region of interest (ROI) as

$$T^{0\nu}_{1/2} > \frac{iN_A\epsilon}{Af}\sqrt{\frac{Mt}{N_{bkg}\Delta E}} \tag{3}$$

where ΔE is the energy resolution at the Q value, f is the number of standard deviation corresponding to a given confidence level and N_{bkg} is the normalized background event rate per unit energy, per unit mass and per unit time, referred to as background index. From above equation, it is evident to achieve a high sensitivity ($\geq 10^{24}$ yrs), it is essential to have high Q value, high detection efficiency, low background (~0.01 counts/kg/keV/year)and large mass detector (∼100-1000 Kg) with high isotopic abundance and very good energy resolution. Further, NTME calculations involve large uncertainties and hence it is important to pursue NDBD in different nuclei. The DBD is allowed in the standard model and has been experimentally observed in 12 different nuclei with half-life ranging from 10^{18} to 10^{24} years [4]. In contrary to that, $0\nu\beta\beta$ is a lepton number violating process and not yet observed. A worldwide effort is underway to search for this rare decay in different nuclei. Till date the best $T^{0\nu}_{1/2}$ limit is reported by KamLAND-Zen on ^{136}Xe as 1.07×10^{26} year at 90% C.L. [5]. Other two major experiments, namely, GERDA and CUORE have reported $T^{0\nu}_{1/2}$ limits (at 90% C.L) for ^{76}Ge and ^{130}Te as 8.0×10^{25} year [6] and 1.5×10^{25} years [7] respectively.

Given its importance, an experiment to search for NDBD in ^{124}Sn (*Tin.Tin*) has been initiated in India [8]. Moderate isotopic abundance (5.8 %) and reasonably high Q-value of 2292.6 ± 0.39 keV makes ^{124}Sn a suitable isotope for this experiment. Since tin becomes superconducting at T_C =

3.17 K it can be made into a bolometric detector with very good energy resolution. It is envisaged to house an array of tin bolometers ($3 \times 3 \times 3$ cm^3) operating at $\sim$ 10 mK at the upcoming underground facility of the India-based neutrino observatory [9]. Bacrania *et.al* have reported tin micro-calorimeter with very good energy resolution [10]. However, large mass superconducting tin bolometer has not yet been made.

At mK temperatures, various extraneous factors (vibration noise, electronic noise, micro-phonics etc.) limits the bolometer energy resolution [11]. Assessment and minimization of the contribution of these factors is of utmost importance to improve the bolometer resolution operating at mK temperature. In this thesis, work related to the development of a tin bolometer is presented. A low noise electronics readout with NI based data acquisition system has been set up. Improvements to the fabrication of indigenous NTD Ge sensors and characterization of these sensors have been performed [12]. A comparative study of the heat capacity of polymers (Teflon, Torlon 4203 and Torlon 4301) is done in the temperature range of 30-400 mK in order to choose a low heat capacity material for support structure in the bolometer [13]. Using a Mathematica based program, implementing macroscopic thermal model, a sapphire bolometer is designed and made. A detailed noise characterization, investigation of various noise sources and its mitigation to improve the performance of the bolometer detector is performed. The sapphire bolometer is tested with heater pulses (0.3–10 MeV) and alpha pulses ($\sim$ 5 MeV), in order to understand the systematic effects relevant for the performance of bolometer at mK temperature. Preliminary studies have been carried out on a moderate size Sn sample (0.6 g) mounted on the Sapphire platform.

CFDR 1200 setup for cryogenic bolomter

A custom made high cooling power (1.4 mW at 120 mK) cryogen free dilution refrigerator (CFDR1200) is installed at TIFR [14] to facilitate R&D related to cryogenic bolometer operating at mK temperatures. The cryogen free design is chosen to carry out uninterrupted measurement over a long duration in an underground laboratory. In the CFDR 1200, the 40 K and the 3 K stages are cooled with the help of a two stage pulse tube cryocooler (Cryomech-PT415). The compressor for the PT is placed in a separate room at a distance ~ 20 m from the cryostat to minimize the acoustic noise. The valve motor control unit is detached from the PT and mounted on a vibration damper, situated on the top of the tripod supporting the cryostat, using a 65 cm long swan neck shaped bellow. It should be mentioned that the pulse tube valve control motor can be powered by a linear drive unit (LNX-G from Precision Motion Control 19 , Inc.), in lieu of the standard stepper motor drive resulting in less noise at temperature T < 100 mK. The CFDR1200 has a large cylindrical sample space (30 cm diameter and 30 cm height) capable of supporting ~100 kg mass at the mixing chamber (MC) and is provided with 300 readout wires enabling simultaneous measurement of 75 sensors in four wire readout scheme. A provision is also made for mounting electronics at 50 K plate for ultra-low noise applications. The CFDR is placed inside a Faraday cage. The PT and various vacuum gauges are interfaced with the PC via an optically isolated RS232 adapter. The temperature of the MC is measured using a Carbon Speer sensor calibrated against a CMN (Cerium Magnesium Nitrate) thermometer, which in turn is calibrated using a superconducting fixed point device (FPD).

The CFDR1200 had a major problem when the ^{3}He circulation line developed a choke. The dilution unit comprising the 800 mK *still*, 50 mK heat exchanger and the MC, was completely dismantled to perform a systematic diagnosis. The choke was located in the secondary impedance below the *still* and was repaired. The dilution unit was reassembled with a new generation *still* containing pressure dependent primary impedances. Subsequently, a leak in the ^{3}He circulation line was located in the solder joint of the sintered silver heat exchanger just below the 50 mK plate and was repaired. Diagnosis and repair of the dilution unit has been a part of the thesis work. After repairs, a detailed assessment of the CFDR was carried out by cooling power measurements. A cooling power of 1.36 mW at 120 mK was recorded with an optimum *still* heater current of 35 mA.

Improvements to NTD Ge sensor fabrication

Neutron transmutation-doped (NTD) Ge sensors are widely used as low-temperature sensors owing to high sensitivity, low specific heat and reasonably fast rise time. Development of NTD Ge sensors for use in *Tin.Tin*, i.e. with tin bolometer at 10 mK, was initiated [15]. Initial attempts have shown good performance down to 75 mK. The performance of NTD sensor at mK temperature depends on several factors like thermal contact to the heat bath, strain/stress in the sensor mounting arrangement, electrical contacts and external noise. Further, minimization of radioactive background arising due to neutron irradiation in NTD Ge fabrication is of paramount importance. This makes the fabrication and testing of NTD Ge sensors, intended for rare decay studies with bolometer operating at mK temperature, very challenging. As a part of the thesis work, various improvements in NTD Ge fabrication have been carried out. Several irradiations (13 batches) were carried out at Dhruva reactor, BARC, Mumbai with an aim to achieve the desired neutron fluence of $\sim 4\times10^{18}/\mathrm{cm}^2$, which was shown to be the optimum dose suitable for NTD sensors in 10-100 mK range [12]. In some cases, an independent estimate of the thermal neutron flux was obtained using a monitor sample of ^{nat}Zr. The irradiated ^{nat}Zr samples have been studied in TILES (Tifr Low background Experimental Setup) and the thermal neutron flux is estimated from the activity of ^{95}Zr. In some cases, internal impurity of ^{123}Sb in the device grade Ge sample (119 ± 7 ppt), is also used to estimate the thermal neutron flux. Neutron irradiation of the Ge sample leads to significant levels of long-lived radioactive impurities on surface and could be removed by chemical etching $\sim 50\mu m$ of the NTD Ge [16]. In the present work, it is shown that the etching of the Ge samples prior to irradiation resulted in reduction of the surface impurity levels by 40-80%. To improve the surface quality of the irradiated wafer, optical finish polishing is done at the final stage, i.e., after post-irradiation chemical etching. A 25 μm thick Al wire is wedge bonded to AuGe contact pads on the sensor for making an electrical readout connection. The mask for depositing AuGe is modified for a wrap around contact, which ensures parallel electric field inside the sensor. This mask can be used for a batch fabrication of upto ~ 150 sensors.

The electronic heat capacity of NTD Ge sensor varies linearly with temperature ($c = \gamma$ T) and can contribute significantly at mK temperature [17] when used in a small size bolometer. Hence, the reduction of the sensor size is very important for such bolometers, to achieve a better energy resolution. Hence, fabrication and characterization of smaller size sensors ($1\times 1\times 1$ mm^3) was carried out. A ~500 nm Au layer is deposited on the two opposite sides for electrical contact. These sensors are ~ 20 times smaller in mass than the earlier sensors ($3\times 6\times 1$ mm^3) and are expected to result in reducing the heat capacity addendum in a bolometer setup by a similar amount.

NI DAQ setup

Commercially available *AC* resistance bridge is capable of low noise measurement of thermistors with resistances only upto 2 MΩ. Typical resistance of NTD Ge sensors at T <50 mK is ~100 MΩ to few GΩ. Very low noise and low excitation (fA to pA) is required to minimize self heating while measuring the resistance of a NTD Ge sensor. A NI based data acquisition system, suitable for bolometer R&D, is developed using LabView software [18]. The data acquisition system (DAQ) consists of a multi-function I/O Module (NI PXI-6281) housed on NI PXIe 1082 chassis. The PXI-6281 has two single ended 16 bit DAC output channels and 8 differential 18 bit ADC input channels. The chassis is interfaced with the PC via a high-speed optical fiber. The output of a DAC channel is supplied to a pair of bias resistors connected in series with the NTD Ge sensor. The voltage across the sensor is amplified using a low noise (5.5 $nV/\sqrt{Hz}$), variable high gain (20 dB to 80 dB), high input impedance (1 TΩ) differential amplifier (Femto DLPVA-100-F) and the output of the amplifier is acquired using an ADC channel in PXI-6281. Measurements of current vs voltage (I-V) characteristics of the sensors at low temperatures (10-400 mK) are performed using customized data acquisition programs developed on the LabView platform. For acquisition over prolonged periods, software has a provision to automatically start a new file after preset interval (0.5 hour was used). A typical noise of $V_{PP} \sim 10$ mV is obtained in the amplified sensor output with 60 dB gain at temperature T < 50 mK.

Results

NTD Ge sensor characterization

NTD Ge sensors having different dopant concentrations are characterized in 10–400 mK temperature range. The temperature dependence of these sensors is shown to be in good agreement with the variable-range hopping mechanism ($R = R_0 exp(\sqrt{T_0/T})$) in this temperature range. The extracted T_0 values show the expected dependence on doping density, but are higher compared to the data in Ref [19]. Data over a wider range of neutron fluence are required for detailed comparison. The improved NTD Ge sensor (as per procedure described in earlier section) is shown to be useful down to

10 mK temperature. However, it should be mentioned that at T < 30 mK, deviations from Mott behaviour are observed.

A set of 6 smaller dimension sensors (four of size $1 \times 1 \times 1$ mm^3 and two of size $2 \times 2 \times 1$ mm^3) are fabricated in a single batch from the M wafer ($N_d = 4.2 \times 10^{18} cm^{-2}$). These sensors are found to have similar Mott behaviour for R-T, in temperature range of 40 mK to 400 mK with ± 15 % variation in T_0 as shown in Fig.0.1.

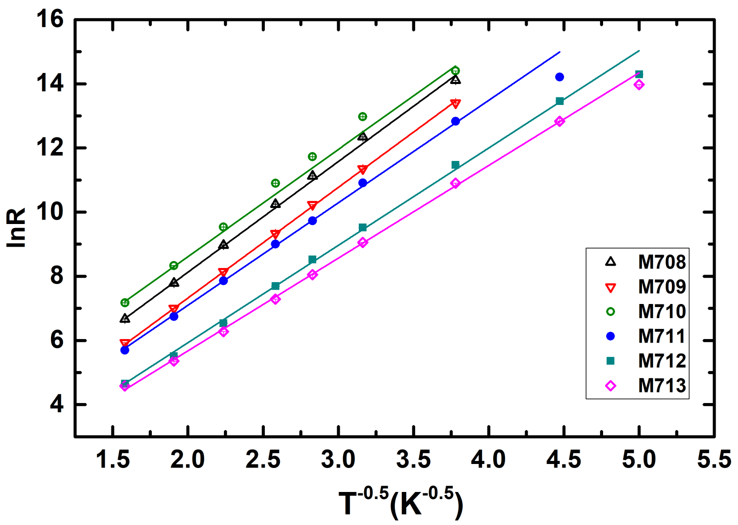

FIGURE 0.1: ln R versus $T^{-0.5}$ together with fits to Mott's curve for M sensors in the temperature range 40–400 mK

Heat capacity measurement of polymers

Amorphous organic polymers are widely used for structural applications at cryogenic temperatures, as these polymers offer high strength to weight ratio and low thermal conductivity. Some of the polymers, which do not form dielectric glasses, can also exhibit low heat capacity at cryogenic temperatures and are suitable for the use as structural supports in the low temperature detectors. While thermal conductivity determines the decay time of the detector, a material with high heat capacity can severely deteriorate the resolution of the detector. It is known that approximately one third of the heat capacity of the thermal link would contribute to the total heat capacity of the calorimetric detector [20]. Hence the heat capacity and the thermal conductivity of these materials are very important to be known. However, there is little or no such data for most of the polymers at the detector operating temperature (typically few tens of mK). This motivated us to measure the specific heat of Teflon (PTFE, virgin grade), Torlon 4203 and Torlon 4301 (polyamideimide; Solvay Advanced Polymers) in the temperature range of 30–400 mK. Measurements are performed employing thermal relaxation calorimetric technique and the results (see Fig. 0.2) are consistent with the tunneling state models used to explain the observed unusual low temperature specific heat of amorphous polymers. While this work reports the specific heat of Torlon 4301 for the first time, it extends the calorimetric data to lower temperatures for Teflon and Torlon 4203 down to 30 mK. The specific heat of Teflon is significantly smaller than Torlon 4203 (about 3 times) and Torlon 4301 (about 10 times) below 100 mK. The data for Teflon is in excellent agreement with the values reported by Boyer et al. from 0.3 K to 20 K. Among Torlon, the specific heat of Torlon 4203 (3% TiO 2 and 0.5% fluorocarbon) is appreciably lower than Torlon 4301 (12% graphite powder and 3% fluorocarbon) over the entire temperature range investigated in this work. Teflon is more suitable for cryogenic applications which require low heat capacity materials and are not strongly constrained by mechanical design of the support structures. However, Torlon exhibits higher tensile and compressive strength and would be preferable for applications with large mechanical load. In such cases, Torlon 4203 would be a suitable material compared to Teflon and Torlon 4301.

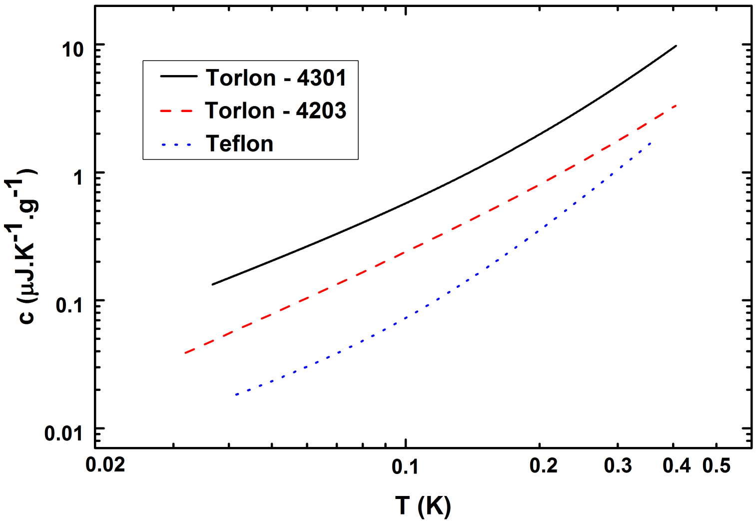

FIGURE 0.2: Comparison of the specific heat of Torlon 4301, Torlon 4203 and Teflon

Tests with a sapphire bolometer

A macroscopic thermal model based on Mathematica [21] is formulated to simulate transient thermal response of a bolometer to an incident heat pulse at mK temperature. This is used to design sapphire bolometer components to obtain optimal performance. The sapphire possesses very low specific heat (20 fJ/K/g at 10 mK), since Debye temperature is large (1042 K) and has been tested at temperature as high as 1.5 K as a bolometer[22]. The sapphire bolometer ($20 \times 20 \times 0.4$ mm^3) is weakly coupled to the CFDR mixing chamber stage by means of four low temperature Araldite glue spots (dia ~ 1 mm and height 0.1 mm). Two NTD Ge sensors and a heater is mounted on the sapphire using a thin layer of Araldite. The heater element is made by evaporating a 100 nm Au meander on a Si substrate. The resistance of the heater element, as measured using an AC resistance bridge AVS-47B, is found to be 0.6 kΩ at 1 K and remains constant over the temperature range of 1 K down to 10 mK. With this setup the effect of external noise is studied in detail and the response to heat pulses (i.e. phonons) as well to alpha particles is investigated. Phonon pulses were generated using a LabView based program, where periodic voltage pulses of width 200 μs were supplied to the heater using a DAC output and the amplified output of the NTD Ge sensor was recorded in an ADC channel with a sampling rate of 50 kHz.

Pulse height analysis program for bolometer

Unlike other particle detectors (e.g., Scintillator detector, HPGe detector), the response time of a bolometric detector is comparatively slow. Typically the rise time of a large mass (~ 100 g) bolometer is ~ 10 ms and decay time ~ 0.1 - 1 s [11]. A software tool in desirable for shaping and analysis of the pulses. A ROOT based C++ program is developed for off-line pulse shape analysis of the bolometer signal. The program consists of two parts. In the first part, smoothened signal (S0), first derivative (S1) and second derivative (S2) of the digitally sampled raw pulse (S) are derived by applying Savitzky-Golay technique [23, 24] as illustrated in Fig. 0.3 (*left*). In the second part, when S1 crosses a certain preset threshold, various pulse shape parameters are extracted and are used to filter out spurious pulses. The pulse height is extracted by integrating the derivative of the signal, and hence it is immune to any slow baseline variations. Also it takes into account the variation in the rise time. Further, the pileup pulses are well separated in S1, yielding efficient pileup rejection as shown in Fig. 0.3 (*right*). A rectangular gate was applied on the mean versus RMS distribution of the baseline of width 100 ms (both before and after the pulse), to reject pulses having unstable baseline. This analysis procedure is applied to both heater pulses and pulses generated due to radiation like α particles, muons etc.

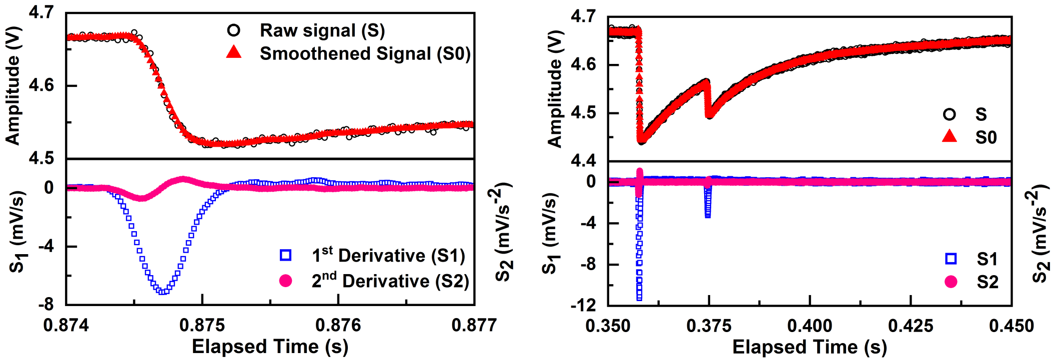

FIGURE 0.3: An example of the pulse processing (*left*) and pile up rejection (*right*).

Effect of external noise

Minimization of external noise originating from the cryogenic system and the associated electronics is very essential in order to achieve a good resolution in the bolometer. Noise induced due to the mechanical vibrations is one of the major drawbacks in a pulse tube based cryogenic system. The effect of mechanical vibrations can propagate to the lowest temperature stage and result in heating of the sensor, thereby affecting the performance of the bolometer. In addition to acting as an additional thermal load, these vibrations can also couple to the signal lines causing microphonic noise pickup in the readout signal. The sapphire bolometer was tested in a conventional wet dilution refrigerator [25] to assess the impact of vibration due to pulse tube cooler. Efforts have been made to reduce the contribution of the pulse tube induced vibrational noise by implementing special vibrational damping measures during the design of the cryostat [14]. Other major contribution in the external noise sources involves the intrinsic noise of the mK thermometer and that induced by the front-end electronics. Apart from these widely known external factors, there can be system specific noise sources like vacuum pumps and measurement electronics. An efficient and proper ground connection of the system is necessary in order to minimize the ground loops, which otherwise can result in noise pickups in the operating frequency range. These various sources of pickups can have a detrimental effect on the overall performance of the bolometer and therefore, it is essential to investigate and eliminate the same. With this motivation, the various noise source and its influence on the sapphire bolometer in the CFDR1200 system at TIFR [14] is studied. The detailed noise measurements in the frequency span of DC – 25 kHz have been carried out for the entire setup including the system related diagnostics, control systems, and the readout including NI-based data acquisition system (DAQ). The latter consists of multiple channels of high precision DAC and ADC, distribution boards, high input impedance-high gain preamplifier, multi-core twisted pair cables as well as the multi- channel twisted pair wiring internal to the cryostat. An efficient grounding configuration is implemented to minimize the ground loops in the system. Several measures are taken to minimize or eliminate unwanted pickups originating from various control and diagnostic modules of the cryogenic system, mainly the vacuum pumps and vacuum gauges. It is shown that the presence of ground loops can worsen the performance of bolometer significantly (~30%). Due to efficient grounding an improvement in the base temperature of the MC (5 mK as compared to 6.7 mK with sub-optimal grounding) was observed. Consequently, the resistance of the NTD Ge sensor (DB27) had improved to ~500 MΩ as compared to ~80 MΩ in sub-optimal ground condition.

Response to phonon pulses

As mentioned earlier, in order to understand various systematics affecting the bolometer performance, the response of the sapphire bolometer in the temperature range of 10-100 mK is measured with phonon pulses generated by a heater. An understanding of the systematics will be useful to study superconducting tin bolometer. Energy resolution (σ) of the sapphire bolometer is measured with heater pulses of equivalent energy of 0.3-10 MeV in the temperature range 10 -100 mK. At each temperature pulse height vs bias current measurement was done and an optimum bias current (20 nA-1 μA) was chosen for the energy calibration measurement. The rise time and the decay time of the bolometer signal at 10 mK are ~1 ms and ~ 15 ms, respectively.

- Though the energy calibration is linear at low energy (< 3 MeV), a deviation of ~8 % is observed at higher energy (10 MeV).
- It is found that energy resolution (σ_0) decreases as function of the MC temperature. However, in the range of 10-25 mK the energy resolution is found to be nearly independent of the temperature.

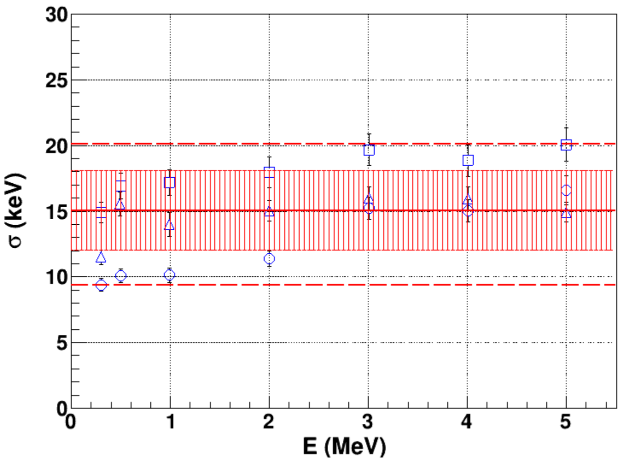

FIGURE 0.4: Energy resolution of the sapphire bolometer at 15 mK with phonon pulses in three different sets of measurements

- The energy resolution in this temperature range was repeated over three different thermal cycles. A good reproducibility is observed and data are shown in Fig. 0.4.

- It can be seen that the energy resolution of the bolometer(σ_0) is nearly constant ~ 15 ± 3 keV over the energy range of 0.3-5 MeV.
- Measurements were also performed with heater energy ranging upto 10 MeV where a non linear dependence of resolution (σ_0 at 10 MeV = 30 keV ± 2 keV) with energy could be seen for energies E>3MeV.
- A moderate size tin sample of mass 0.6 g was mounted on the sapphire substrate using N-Grease and the energy resolution (σ_{Sn}) in the temperature range of 15 - 25 mK is compared with that for the blank sapphire. No significant difference could be noted on the decay time and the linearity of the energy calibration. It is observed that for E<3 MeV, the σ_{Sn} is comparable to σ_0 but at higher energies σ_{Sn} increases with E. This is surprising as thermal noise is temperature dependent and not energy dependent. Also, most of other external noise factors are expected to be independent of energy.

Response to alpha pulses

For tests with alpha particles, a weak ^{239}Pu-^{241}Am alpha source (~ 10 dps) electroplated on a SS disk is mounted with a brass collimator (1 mm dia). The mounting setup is shown in Fig. 0.5. Expected energies form the two major peaks are 5.156 MeV and 5.485 MeV [26]. The energy spectrum of the source with the collimator was recorded using a silicon surface barrier detector for reference. The alpha pulses were acquired for a duration of ~ 6-10 hours at different MC temperatures of 15 mK, 20 mK and 25 mK. A LabView program was used to record the amplified voltage signal in

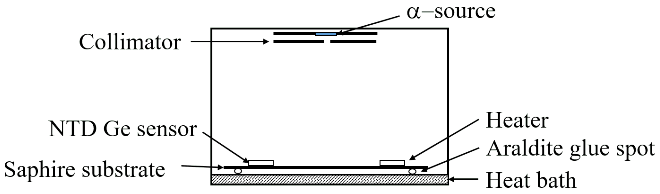

FIGURE 0.5: A schematic of the sapphire bolometer setup with the alpha source

leading edge trigger mode with a sampling rate of 50 kHz. The acquired data was analyzed using the analysis technique as described earlier and the spectrum is shown in Fig. 0.6. Although two peaks are visible, they are not very well separated. The peak at low energy (pulse height ~ 0.035 V) can arise due to energy deposition of cosmic muons. It is puzzling to note that E_α estimated from the heater calibration, namely, 3.3 MeV and 3.6 MeV, are significantly lower than the actual source energies (5.156 MeV and 5.485 MeV, respectively). Discrepancy in the heater calibration and radiation energy was earlier reported in Ref [27], but has not been understood. The resolution σ ~ 70-180 keV estimated from the energy difference in peaks Δ E = 330 keV and is considerably worse than the σ_0. It

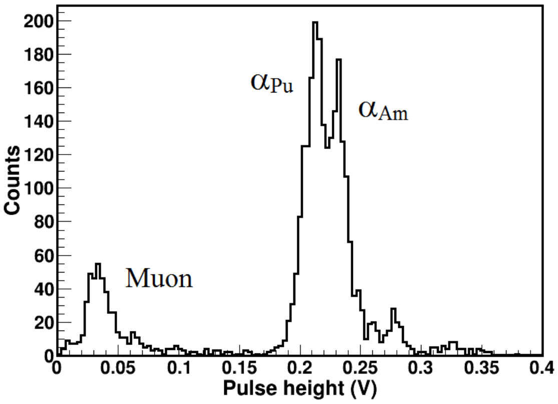

FIGURE 0.6: Pulse height spectrum obtained with the alpha source

should be mentioned that baseline/peak drifts over larger acquisition period could contribute to worsening of the resolution. Further investigation with γ sources and/or muons will be required.

To summarize, the first test of a cryogenic sapphire bolometer with indigenously made NTD Ge sensor is carried out. Response of the sapphire bolometer is studied with phonon pulses and a energy resolution of 15 keV ± 3 keV is obtained in the temperature range of 15 – 25 mK. Compared to CUORE TeO_2 bolometer, this is worse by about a factor of 5. The energy resolution of the sapphire bolometer with a Sn of mass $\sim$ 0.6 g does not show appreciable change below 3 MeV. The spectrum of alpha particles is also measured with the cryogenic bolometer. This work provides key inputs for the fabrication of tin superconducting bolometers to be used in the *TinTin* experiment.

Chapter 1

Introduction

According to the standard model (SM) of elementary particles, the basic building blocks of matter consist of three generations of quarks and leptons which interact via three fundamental forces of nature: electromagnetic, weak and strong forces mediated by their corresponding gauge bosons. Neutrinos, neutral, spin $\frac{1}{2}$, fundamental particles, form a part of a doublet with the corresponding charged leptons, namely: electron, muon and tau. Neutrinos were predicted to be massless in the SM, but recent experiments have conclusively shown that neutrinos have non-zero finite mass [1, 2]. Despite phenomenal progress in the field of neutrino physics, fundamental properties like mass and nature of neutrinos (whether neutrino is it's own antiparticle or not) remain unknown. Neutrinoless double beta decay (NDBD or $0\nu\beta\beta$), a lepton number violating process, proposed as an extension of physics beyond the SM, holds the key to address some of these issues. Given it's extensive significance in the fundamental understanding of the universe at large, an worldwide campaign to search for this rare decay process is continuing. In India, an initiative has been undertaken to search of NDBD in ^{124}Sn using a cryogenic tin bolometer. Various aspects related to R&D of the indigenous development of a cryogenic bolometer are presented in this thesis.

1.1 Brief history of neutrinos

Neutrinos have been enigmatic ever since they came into existence. It was very puzzling for physicists in the early twentieth century to comprehend the continuous energy spectra of the electron emitted in a radioactive beta decay observed. During that period the beta decay was believed to be a two body decay and a discrete energy spectrum was expected as observed in alpha or gamma decay. To solve this mystery, W. Pauli postulated the existence of the neutrino in 1930 [28]. He proposed that in addition to the electron, a chargeless light particle is also emitted escaping the detection but carries the missing energy. Following which Fermi proposed the theory of beta decay assuming the neutrinos to be Dirac particle [29]. The experimental observation came two decades later when Reines and Cowan experimentally observed neutrino originating from a nuclear reactor near Savannah River, South Carolina in 1956 [30]. It took almost half a century since then, to confirm that neutrinos oscillate from one flavour to another as they propagate. Consequently, the flavour eigenstates $(\nu_e, \nu_\mu, \nu_\tau)$ are represented as a super position of three mass eigenstates (ν_1, ν_2, ν_3) with mass m_1, m_2 and m_3.

$$|\nu_l\rangle = \sum_i U_{li}^* \nu_i \tag{1.1}$$

here $l = e, \mu, \tau$ are the flavour eigenstates and $i = 1, 2, 3$ are the mass eigenstates. The mixing matrix U is known as the PMNS matrix in the honor of B. Pontecorvo, Z.Maki, M. Nakagawa and S. Sakata and has the form

$$U = \begin{bmatrix} c_{12}c_{13} & s_{12}c_{13} & s_{13}e^{-i\delta_{13}} \\ -s_{12}c_{23} - c_{12}s_{23}s_{13}e^{i\delta_{13}} & c_{12}c_{23} - s_{12}s_{23}s_{13}e^{i\delta_{13}} & s_{23}c_{13} \\ s_{12}s_{23} - c_{12}c_{23}s_{13}e^{i\delta_{13}} & -c_{12}s_{23} - s_{12}c_{23}s_{13}e^{i\delta_{13}} & c_{23}c_{13} \end{bmatrix} \times \mathrm{diag}(e^{i\lambda_1}, e^{i\lambda_2}, e^{i\lambda_3}) \tag{1.2}$$

where c_{ij} and s_{ij} are $\cos\theta_{ij}$ and $\sin\theta_{ij}$, respectively, θ_{ij} s are the mixing angles and λ_i are the Majorana phases and are non-zero only if neutrinos are Majorana in nature. The data from neutrino oscillation experiments in solar, atmospheric, accelerator and nuclear reactor neutrinos have determined the matrix U with a reasonable precision [31]. The probability that a neutrino ν_α of energy E will oscillate into ν_β after traversing a distance L can be expressed as

$$\begin{aligned} P_{\nu_\alpha \to \nu_\beta}(L, E) = \delta_{\alpha\beta} - 4 \sum_{i>j} \mathrm{Re}\,(U^*_{\alpha i} U_{\beta i} U_{\alpha j} U^*_{\beta j}) \sin^2\left(\frac{\Delta m^2_{ij}\, L}{4E}\right) \\ +2 \sum_{i>j} \mathrm{Im}\,(U^*_{\alpha i} U_{\beta i} U_{\alpha j} U^*_{\beta j}) \cos\left(\frac{\Delta m^2_{ij}\, L}{2E}\right) \end{aligned} \tag{1.3}$$

It can be seen from Eqn. 1.3 that the neutrino oscillations are sensitive only to the difference of the squared masses $\Delta m^2_{ij} \equiv m^2_i - m^2_j$. Two mass square differences have been measured and the global fit values are shown in Table. 1.1 However, the sign of Δm^2_{32} is not yet known.

TABLE 1.1: Globally fit neutrino oscillation parameters from Ref. [31].

Parameter	Best Fit ($\pm 1\,\sigma$)	$2\,\sigma$ range	$3\,\sigma$ range
$\Delta m^2_{21} [10^{-5}\text{ eV}^2]$	$7.55^{+0.20}_{-0.16}$	7.20–7.94	7.05–8.14
$\left\vert\Delta m^2_{31}\right\vert [10^{-3}\text{ eV}^2]$ (NH)	2.50 ± 0.03	2.44–2.57	2.41–2.60
$\left\vert\Delta m^2_{31}\right\vert [10^{-3}\text{ eV}^2]$ (IH)	$2.42^{+0.03}_{-0.04}$	2.34–2.47	2.31–2.51

Depending on this sign two different mass hierarchy are possible, i.e., normal hierarchy (NH) if it is positive with $m_1 < m_2 < m_3$ or inverted hierarchy (IH) if it is negative with $m_3 < m_1 < m_2$. Currently, accelerator based long-baseline experiments (NOVA [32] and T2K [33]) and reactor based medium-baseline experiments (JUNO [34]) are progressing, aiming to determine the neutrino mass hierarchy.

1.2 Dirac and Majorana neutrinos

A spin 1/2, free fermion of mass m can be represented with a 4-component spinor field ψ which satisfies the the Dirac equation

$$(i\gamma^\mu \partial_\mu - m)\psi = 0 \tag{1.4}$$

Here the 4×4 γ-matrices are $\gamma^0 = \begin{pmatrix} I & 0 \\ 0 & -I \end{pmatrix}$, $\gamma^i = \begin{pmatrix} 0 & \sigma_i \\ -\sigma_i & 0 \end{pmatrix}$ and $\gamma^5 = \begin{pmatrix} 0 & I \\ I & 0 \end{pmatrix}$,

σ_i being the 2×2 Pauli Matrices. The γ-matrices satisfies the anti-commutation rule $\{\gamma^\mu, \gamma^\nu\} = 2g^{\mu\nu}$ and $\{\gamma^\mu, \gamma^5\} = 0$ where $g^{\mu\nu}$ is the Minkowski space-time metric $(+1, -1, -1, -1)$. The four independent component of the field ψ represents the particles and antiparticles with two possible helicities ($\mathcal{H} = \pm 1$). The Lagrangian density for the Dirac field in the equation 1.4 can be written as

$$\mathcal{L} = i\overline{\psi}\gamma^{\mu}\partial_{\mu}\psi - m\overline{\psi}\psi \tag{1.5}$$

It should be noted from the above equation that the mass for a spin 1/2 particle is obtained from the term of the form $\overline{\psi}\psi$. It is possible to represent ψ in the chiral basis as $\psi = \psi_L + \psi_R$ where ψ_L and ψ_R are the left-handed and right-handed projections of the spinor ψ as given below

$$\psi_L = P_L\psi = \frac{1}{2}(1-\gamma^5)\psi \ ; \ \psi_R = P_R\psi = \frac{1}{2}(1+\gamma^5)\psi. \tag{1.6}$$

Where the P_L and P_R are the projection operators and they obey the following relations.

$$P_L\, P_R = P_R\, P_L = \ 0 \text{ and } P_L \ + \ P_R = I. \tag{1.7}$$

Using the above relations the mass term in the equation 1.5 takes the form

$$\mathcal{L}_D = -m_D\overline{\psi}\psi = -m_D(\overline{\psi_L}+\overline{\psi_R})(\psi_L+\psi_R) = -m_D(\overline{\psi_L}\psi_R+\overline{\psi_R}\psi_L) \tag{1.8}$$

where m_D is the Dirac mass of the particle. Thus in order for the neutrinos to have a Dirac mass, right handed neutrinos (ν_R) and left handed antineutrinos ($\overline{\nu_L}$) would be required. Since, in the SM only the left handed neutrinos (ν_L) and right handed antineutrinos ($\overline{\nu_R}$) exist, neutrinos are massless in the SM. Further, the weak interaction acts only on the ν_L and $\overline{\nu_R}$ hence, ν_R and $\overline{\nu_L}$ would be non interacting or sterile. The fact that there is no evidence of ν_R or $\overline{\nu_L}$, there should be a different mechanism by which neutrinos get their mass.

Since neutrinos are charge less, it possible to construct a field $\psi = \psi_L + \psi_L^c$ such that $\psi = \psi^c$, which means that the neutrinos are equivalent to its antiparticle, also known as Majorana fermions. The Majorana mass term can then be written as

$$\mathcal{L}_M = -\frac{m_L}{2}(\overline{\psi_L}\psi_L^c + \overline{\psi_L^c}\psi_L) - \frac{m_R}{2}(\overline{\psi_R}\psi_R^c + \overline{\psi_R^c}\psi_R) \tag{1.9}$$

Here, m_L and m_R are the Majorana masses for neutrinos. The Majorana mass term directly couples particle and antiparticle which violates charge conservation. Hence, only the neutrinos in the SM can have Majorana mass. The most general mass term for neutrinos can be expressed as

$$\begin{aligned}\mathcal{L}_n &= -m_D(\overline{\psi_L}\psi_R + \overline{\psi_R}\psi_L) - \frac{m_L}{2}(\overline{\psi_L}\psi_L^c + \overline{\psi_L^c}\psi_L) - \frac{m_R}{2}(\overline{\psi_R}\psi_R^c + \overline{\psi_R^c}\psi_R)\\ &= -\frac{1}{2}\begin{pmatrix}\overline{\psi_L^c} & \overline{\psi_R}\end{pmatrix}\mathcal{M}\begin{pmatrix}\psi_L\\ \psi_R^c\end{pmatrix} + h.c\end{aligned} \tag{1.10}$$

where the mass matrix $\mathcal{M}$ is given by

$$\mathcal{M} = \begin{pmatrix}m_L & m_D\\ m_D & m_R\end{pmatrix} \tag{1.11}$$

If it is assumed that $m_L = 0$ and $m_R \gg m_D$, then the matrix $\mathcal{M}$ can be diagonalized with two eigenvalues m_R and $\frac{m_D^2}{m_R}$. This is known as the see-saw model which predicts a light and a heavy Majorana neutrino, and provides an explanation to the smallness of the neutrino mass as compared to m_D which is expected to have a mass similar to the charged Dirac fermions.

1.3 Double beta decay and neutrinoless double beta decay

Maria Goeppert-Mayer in 1935 proposed the idea of double beta decay (DBD or $2\nu\beta\beta$) [35]. In DBD, an even Z - even N nucleus (A,Z) decays to an isobar (A,Z+2) by emitting two electrons and two antineutrinos.

$$(A, Z) \rightarrow (A, Z + 2) + 2e^{-} + 2\bar{\nu}_e \tag{1.12}$$

This is a second order spontaneous nuclear transition and is feasible only for isotopes in which the single beta decay is either energetically forbidden or spin forbidden. A schematic representation of this is shown in Fig. 1.1. Maria Goeppert-Mayer also derived an expression for the decay rate and

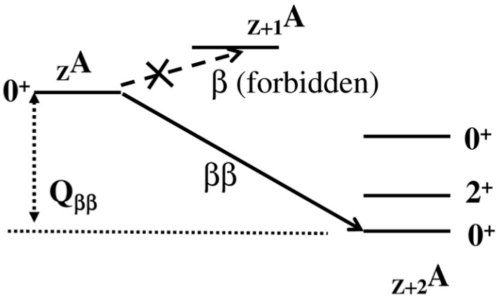

FIGURE 1.1: A schematic of the energy level diagram for DBD, taken form Ref. [36]

estimated a half-life $\sim 10^{17}$ years. The idea of DBD was motivated by the presence of few naturally occurring even-even nuclei even billion years after the formation, which otherwise were believed to be candidates for beta decay and should have become extinct through radioactive disintegration. Soon after Majorana put forward his symmetric theory of particles and antiparticles [37], Racah suggested another mode of double beta decay, where no antineutrinos are emitted in the final state, known as neutrinoless double beta decay (NDBD or $0\nu\beta\beta$) [38]. The NDBD is a lepton number violating process ($\Delta L = 2$) and possible only if neutrinos are Majorana particles. The Feynman diagram for the two processes is shown in Fig. 1.2. The first calculation of the rate for $0\nu\beta\beta$ decay was performed by

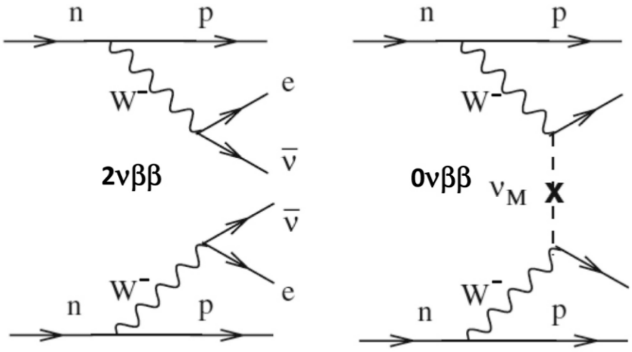

FIGURE 1.2: Feynman diagram for DBD (*left* and NDBD *right*), taken form Ref.[3]

W. H. Furry in 1939 [39]. At that time decay rate of $0\nu\beta\beta$ was predicted to be 10^6 faster than the decay rate of $2\nu\beta\beta$ due to increased phase space in the former as the virtual neutrinos in the $0\nu\beta\beta$ can have states upto 100 MeV following the Heisenberg uncertainty principle, whereas in $2\nu\beta\beta$ the states are limited only by the Q value of the decay. The NDBD decay rate is suppressed as it is proportional to the tiny neutrino mass in the decay rate (equation 1.13). Primakoff calculated the energy and angular momentum distribution of the electron providing an useful tool to distinguish between $2\nu\beta\beta$ and $0\nu\beta\beta$ processes [40]. The decay rate, i.e. the inverse of the half-life of the NDBD process is given by Equation 1.13 as,

$$(T^{0\nu}_{1/2})^{-1} = G_{0\nu}(Q_{\beta\beta}, Z)|M_{0\nu}|^2 < m_{\beta\beta} >^2 \tag{1.13}$$

where $G_{0\nu}(Q_{\beta\beta}, Z)$ is the phase space factor, $M_{0\nu}$ is the nuclear transition matrix element (NTME) and $m_{\beta\beta}$ is the effective Majorana mass of the electron neutrino [3]. The NTME calculations involve large uncertainties and hence it is important to pursue NDBD in different nuclei [41]. At present, NDBD is perhaps the only viable experiment, which can reveal the true nature of neutrino and also measure the absolute effective mass of neutrino.

1.4 Experimental considerations for NDBD

There are 35 nuclei which are potential candidates for the DBD [42]. The first geochemical observation of DBD was reported in 1950 [43].The first direct detection of DBD occurred in 1987 in ^{82}Se [44]. Since then it has been observed in 12 different nuclei with half-life ranging from 10^{18} to 10^{24} years [4]. A peak at the Q value in the sum energy spectrum of the two electron would be an experimental signature of the NDBD process as depicted in the Fig. 1.3. If the peak is observed after a measurement time

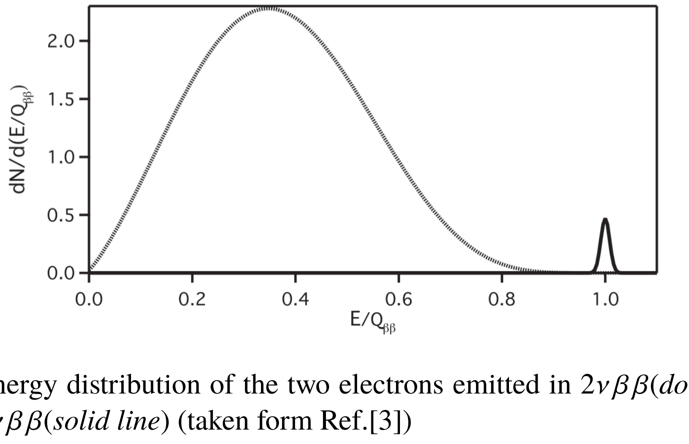

FIGURE 1.3: Energy distribution of the two electrons emitted in $2\nu\beta\beta$(*dotted line*) and $0\nu\beta\beta$(*solid line*) (taken form Ref.[3])

t << $T^{0\nu}_{1/2}$ the half-life can be expressed as

$$T^{0\nu}_{1/2} = \frac{iN_A M t \epsilon}{A N_{0\nu\beta\beta}} \tag{1.14}$$

where $iN_A M/A$ equates to the number of parent atoms in the source material of mass M having isotopic abundance i, N_A is the Avogadro number, ϵ is the detector efficiency and $N_{0\nu\beta\beta}$ is the number $0\nu\beta\beta$ events observed. If no peak is observed a lower limit on the half-life can be placed depending on the background fluctuation at the region of interest (ROI) as

$$T^{0\nu}_{1/2} > \frac{iN_A \epsilon}{A f} \sqrt{\frac{Mt}{N_{bkg} \Delta E}} \tag{1.15}$$

where ΔE is the energy resolution at the Q value, f is the number of standard deviation corresponding to a given confidence level and N_{bkg} is the normalized background event rate per unit energy, per unit mass and per unit time, referred to as background index. Considering the equation 1.15, the following aspects are important to be noted in a $0\nu\beta\beta$ experiment.

Choice of isotope - The phase space factor for NDBD varies as $Q^5_{\beta\beta}$, hence isotopes with high $Q_{\beta\beta}$ values are highly desirable. Also the background arising due to the natural radioactivity is less for $Q_{\beta\beta} >$ 2.6 MeV. Isotopes with higher natural abundance or having possibility of enrichment would be beneficial for increasing the sensitivity.

Low background - The ultimate sensitivity is limited by the background in the experiment. An underground facility is required for shielding cosmic muons. All the materials used in the experiment including the source and the surroundings should have minimal radioactive contamination. Muon induced background gamma or neutral background should also be considered.

Good energy resolution - Very good energy resolution is a fundamental requirement for the presence of unavoidable background from the tail of the $2\nu\beta\beta$ events.

High detection efficiency - NDBD is a very rare process. High detection efficiency is very crucial. Assuming same background, a detector with double the efficiency would require 4 times less mass to achieve the same sensitivity.

Large exposure - Detectors of mass few tons are required to be operated for few year to a reach the sensitivity that can probe inverted mass hierarchy region. Current experiments are mostly of the size of ~10 kg to ~100 kg. The detector technology should have provision for easy upscaling of size.

A worldwide effort is underway to search for this rare decay in different nuclei employing different cutting edge detection technologies and a detailed overview can be found in Ref [45]. Till date the best $T^{0\nu}_{1/2}$ limit is reported by KamLAND-Zen on ^{136}Xe as 1.07×10^{26} year at 90% C.L. [5]. Other leading experiments which have very recently reported half-life limits > 10^{25} years are GERDA(8×10^{25} year [6]), MAJORANA(1.9×10^{25} year [46]), EXO-200(1.8×10^{25} year [47]) and CUORE(1.5×10^{25} year [7]). However, no NDBD signal is observed as yet.

1.5 The Tin.Tin experiment

Given its importance, an experiment to search for NDBD in ^{124}Sn (*Tin.Tin*) has been initiated in India [8]. Moderate isotopic abundance (5.8 %) and reasonably high Q-value of 2292.6 ± 0.39 keV makes ^{124}Sn a suitable isotope for this experiment. Since tin becomes superconducting at T_C = 3.7 K it can be made into a bolometric detector with very good energy resolution. It is envisaged to house an array of tin bolometers ($3 \times 3 \times 3$ cm^3) operating at $\sim$ 10 mK at the upcoming underground facility of the India-based neutrino observatory. Tin micro-calorimeter with very good energy resolution have been reported earlier [27, 10]. However, large mass superconducting tin bolometer has not yet been made. This thesis focuses on the various aspects related to the development of a cryogenic bolometer for the TinTin experiment.

1.6 The cryogenic bolometer detector

Cryogenic bolometer is a low temperature calorimetric detector in which the energy deposition due to an impinging radiation is measured from the temperature rise in an absorber. These detectors are very attractive for applications in nuclear, particle and astroparticle physics experiments where a very low energy threshold or very good energy resolution is required. Conventional calorimetric detectors measure the energy deposited by a particle in the form of ionization energy loss or scintillation light. Energy resolution of such detectors is limited by the statistical fluctuation in the total number of charge carriers or photoelectrons generated in an event and the best achieved energy resolution with such detectors is already very close to the theoretical limit. A large fraction of the total energy deposited is available in the form of the heat, which remains unaccounted in such detectors. Cryogenic bolometer measures the total energy deposition by detecting the phonons or quasi-particles (in superconductor). Hence, energy quanta for cryogenic bolometers are at least 100 times smaller than the other detectors allowing them to have much higher resolution and very small energy threshold.

1.6.1 Brief history

Historically, the bolometer was first introduced by S. P. Langley when he used a Wheatstone's bridge with two metal strips as virtual arms to measure the infrared spectrum of solar radiation and the solar constant in the year 1878 [48]. Simon suggested to use bolometer at low temperature as a calorimetric device to achieve better sensitivity exploiting the reduced heat capacity at low temperature in 1935 [49]. Implementing his idea D.H. Andrews, R.D. Fowler and M.C. Williams made the first cryogenic bolometer in 1949, using a superconducting strip of NbN mounted on a copper holder and reported the detection of α-particles from a Po source [50]. The design of a composite bolometer i.e., using an absorber thermally coupled with a separate temperature sensor was used by N. Coron, G. Dambier and J. Leblanc in 1972 [51]. T. Niinikoski and F. Udo proposed the idea of using cryogenic bolometers for detecting neutrinos in 1974 [52]. A decade later, Fiorini and Niinikoski realized the potential use of bolometers in neutrinoless double beta decay experiments [53].

1.6.2 Basic principle of a cryogenic bolometer

A cryogenic bolometer mainly consists of three parts: an absorber, a temperature sensor and a thermal link weakly coupled to a heat bath. When a particle or radiation deposits energy in the absorber the temperature of the absorber increases which is measured with the help of a temperature sensor, strongly coupled to the absorber. A particle interaction produces phonons that are far from the equilibrium. These phonons lose their energy by electron-phonon, phonon-phonon interactions and interaction with lattice irregularities and come to an approximate equilibrium distribution. This thermalization time can vary from few μs to few 10 ms depending of the size of the absorber, which limits the count rate of cryogenic bolometer to few Hz to few kHz. The temperature profile of an absorber with heat capacity C for an energy deposition of E at a base temperature of T_0 can naively be represented as

$$T(t) = T_0 + \frac{E}{C}\frac{\tau_d}{\tau_d - \tau_r}\left[exp\left(-\frac{t}{\tau_d}\right) - exp\left(-\frac{t}{\tau_r}\right)\right] \tag{1.16}$$

Here τ_r and τ_d are related to the rise time and decay time of the pulse. While the τ_r is related to the thermalization time in the absorber material, τ_d is given by

$$\tau_d = \frac{C}{G} \tag{1.17}$$

G being the thermal conductance of the thermal link. The temperature rise after complete thermalization of the deposited energy is

$$\Delta T = \frac{E}{C} \tag{1.18}$$

From equation 1.18 it is evident that materials with low specific heat at low temperature are desirable for absorber. The specific heat for non-magnetic solids at low temperature can be generalized to have two contributions namely the electronic, vibrations of the atoms or phonons specific heat.

$$c \ = \ c_e \ + \ c_{ph} \tag{1.19}$$

For crystalline insulators the most dominant contribution comes from the phonons. Applying the Debye model, the specific heat of a pure insulating crystal can be expressed as

$$c_{insulator} = c_{ph} = \beta \left(\frac{T}{\theta_D} \right)^3 \tag{1.20}$$

here $\beta = \frac{12\,\pi^4}{5} \cdot N_A k_B = 1944$ J mol^{-1} K^{-1} and θ_D is the Debye's temperature of the crystal [54]. In metals, in addition to the lattice vibrations, thermally excited electrons also contribute to the specific heat

$$c_{metal} = c_{ph} + c_e = \beta \left(\frac{T}{\theta_D} \right)^3 + \gamma T \tag{1.21}$$

γ is Sommerfeld constant and it depends on the material. As the electronic specific heat varies linearly, at temperature <1 K the lattice contribution becomes negligible compared to the electronic counterpart. In superconductor, due to formation of cooper pairs, the thermally excited electrons across the energy gap of the super conductor starts to decrease drastically and the specific heat due to quasi-particles decreases exponentially as given below.

$$c_{sc} = c_{ph} + c_e = \beta\left(\frac{T}{\theta_D}\right)^3 + 9.17\gamma\, T_c exp\left(-\frac{1.5T_c}{T}\right) \tag{1.22}$$

Therefore, at $T \ll T_c$ specific heat of superconductor is dominated by lattice vibrations, which makes it a favourable absorber material for making a cryogenic bolometer.

1.6.3 Temperature sensor

Resistive thermometers, like semiconducting thermistors [19] and superconducting transition edge sensors (TES) [55] are commonly used as a thermometer where the resistance varies as a function of temperature. Sensitivity of such sensor are compared with the dimensionless quantity

$$\alpha = \frac{\mathrm{d\,logR}}{\mathrm{d\,log}T} = \frac{T}{R}\frac{\mathrm{d}R}{\mathrm{d}T} \tag{1.23}$$

These sensors are incorporated in a bias electronic circuit and the temperature rise is extracted as a voltage signal. In TES, a thin film or strip is made from a superconducting material and is operated in the narrow temperature range between normal and superconducting phase where the resistance varies from zero to R_N (resistance at normal conducting state) with very high sensitivity of $\alpha \sim 1000$.

A heavily doped semiconductor with dopant concentration slightly below the metal insulator transition is used as a semiconductor thermistor. The temperature dependence of the resistance of such sensors at low temperature (<~ 10 K) is well explained by the phonon assisted electron hopping mechanism or commonly known as "variable range hopping" (VRH) [56] and is given by the formula

$$R = R_0 \, exp \sqrt{\frac{T_0}{T}} \tag{1.24}$$

Homogeneous doping and good reproducibility are essential for the semiconductor thermistor. This can be achieved by either ion implantation or neutron transmutation doping (NTD). Ge wafers are irradiated with thermal neutrons to fabricate NTD Ge sensor. In ^{nat}Ge samples, thermal neutron capture by various isotopes leads to production of Ga, As, Se and results in p-type Ge. The doping concentration is controlled by the neutron fluence. Since the neutron capture cross-section is small for Ge it leads to a uniform and controlled doping [57]. Compared to TES, NTD Ge has two order magnitude less sensitivity. However, the readout and temperatures stability is simpler in NTD. Moreover, NTD can be used continuously over a wide range of temperature allowing it to study many thermal properties of the detector as a function of temperature.

Apart from NTD and TES other devices that are commonly used as temperature sensors are Microwave Kinetic Inductance Detector (MKID), Magnetic Calorimeters (MMC) [58] and Superconductive Tunnel Junctions (STJ) [59]. MMC and KIDS are magnetic thermometers and are non-dissipative as these sensors do not require readout power.

The intrinsic energy resolution of a cryogenic bolometer arises from the fluctuation in the number of phonons in the absorber and is given by [60]

$$\Delta E = \sqrt{k_B T^2 C} \tag{1.25}$$

It can be seen that the intrinsic energy resolution is independent of the incident energy. In practical scenario the fundamental limit on the energy resolution is extremely small as compared to the contribution from external sources of noise e.g., Johnson noise of the load resistor, the amplifier noise, vibrational noise, micro-phonics, EMI pickups etc [11, 61, 62].

1.6.4 Applications of cryogenic bolometer

In addition to the unprecedented energy resolution with extremely low energy threshold, wide choices on the absorber material and high detection efficiency makes the cryogenic bolometer suitable choice for versatile experiments e.g., X-ray astronomy, beta-gamma spectroscopy, heavy ions physics, low energy neutrino detection using coherent scattering, NDBD and dark matter (DM) search etc. [63, 64]. Recent advances in the application of cryogenic bolometer in various fields can be found in Ref. [65, 66] and references therein. Depending on size of the absorber the bolometer is characterized into two categories, microbolometer (mass$\lesssim$1 mg) and macrobolometer of mass (mass$\gtrsim$1 mg). The largest bolometer, reported by Cardiani *et al.,* [67], is a 2.13 kg TeO_2 bolometer with energy resolution of 3.9 keV (at 145 keV) to 7.8 keV (at the 2615 keV). Macrobolometers are best suited for rare event searches like NDBD or DM detection. The direct detection of DM [68] requires measuring the kinetic energy (few keV) of the recoiling nucleus, for which a low energy threshold and high efficiency detector, like a cryogenic bolometer is needed. Various experiments that are using cryogenic bolometer for NDBD or dark matter search are summarized in Table 1.2.

TABLE 1.2: Dark matter and NDBD experiments experiments with macrobolometer

Experiment	Application	Location	Absorber	Size	Sensor
Super CDMS [69]	DM	Soudan	Ge	0.6 kg	TES
EDELWEISS [70]	DM	France	Ge	0.8 kg	NTD Ge
CRESST [71]	DM	LNGS Italy	$CaWO_4$	0.3 kg	TES
COSINUS [72]	DM	LNGS Italy	NaI	66 g	NTD Ge
CUORE [7]	NDBD	LNGS Italy	TeO_2	750 g	NTD Ge
CUPID [73]	NDBD	LNGS Italy	TeO_2	435 g	NTD Ge
LUCIFER [74]	NDBD	LNGS Italy	ZnSe	430 g	NTD Ge
LUMINEU [75]	NDBD	LSM France	Li_2MoO_4	0.3 kg	NTD Ge
AMoRE [76]	NDBD	Y2L S Korea	$CaMoO_4$	340 g	MMC

Since, the T_c for Sn is 3.7 K, it is possible to make Sn bolometers with very good energy resolution when operated at temperature $\sim$ 10 mK. Hence, a Sn bolometer is considered to be a suitable detector to search for NDBD in ^{124}Sn. In this thesis, work related to the development a mK cryogenic bolometer for the Tin.Tin experiment is presented. Currently, NTD Ge sensors are used for the R&D on the cryogenic bolometer for the Tin.Tin detector. These sensors are made by irradiating Ge wafers from the Dhruva reactor BARC, Mumbai. The preliminary results are reported in Ref. [15]. Several improvements in NTD Ge sensor fabrication are carried out as a part of the thesis. Characterization of NTD Ge sensor with different carrier concentration in the temperature range of 100–400 mK to obtain an optimized dopant concentration [12] is done. Performance of NTD Ge sensors is studied down to 10 mK.

The thermal link plays a key role in obtaining an optimum response of a cryogenic bolometer. In practical scenario $C = C_{total} = C_{absorber} +$

$C_{addendum}$ is the total heat capacity of the detector. Bachmann et al. [20] have shown that about one third of the heat capacity of the thermal link contributes to C_{total} as addendum. Hence, it is very important to chose the material for making the thermal link such that the addendum is minimal. Few polymers, which do not form dielectric glasses, can also exhibit low heat capacity at cryogenic temperatures. This polymers are mostly used as support structure for the detector which also acts as the weak thermal link. Heat capacity data for most of this polymers were not available close to the detection operating temperature ($\sim$ 10 mK). With this motivation a comparative study on the heat capacity of polymers (Teflon, Torlon 4203 and Torlon4301) is studied in the temperature range of 30-400 mK [13].

A macroscopic thermal model for designing a sapphire test bolometer is formulated. A LabView based NI based DAQ is setup with a low noise electronics is setup. A ROOT and C++ based pulse shape analysis program for bolometer is made [77]. Testing of a cryogenic sapphire bolometer with indigenously developed NTD Ge sensor is carried out. As discussed earlier, various extraneous factors (vibration noise, electronic noise, micro-phonics etc.) limits the bolometer energy resolution at mK temperature. Assessment and minimization of the contribution of these factors is of utmost importance to improve the bolometer resolution operating at mK temperature. A detailed noise characterization, investigation of various noise sources and its mitigation to improve the performance of the bolometer detector is performed [78]. The sapphire bolometer is tested with heater pulses (0.3–10 MeV) and alpha pulses ($\sim$ 5 MeV), in order to understand the systematic effects relevant for the performance of bolometer at mK temperature. Preliminary studies have been carried out on a moderate size Sn sample ($\sim$ 0.6 g) mounted on the Sapphire platform.

In the second chapter, the mK thermometry setup at TIFR for the development of a cryogenic bolometer is explained. Chapter 3 describes characterization of NTD Ge sensors. A comparative study on the heat capacity of polymers (Teflon, Torlon 4203 and Torlon4301) in the temperature range of 30-400 mK is presented in Chapter 4. In chapter 5, studies related to a cryogenic sapphire bolometer is presented. A future outlook on improving the bolometer resolution and making a large size tin bolometer for the TinTin experiment is given after summarizing the thesis in chapter 6.

CHAPTER **2**

Experimental setup for low temperature thermometry at TIFR

2.1 Introduction

The cryogenic bolometer detectors are mostly operated at temperature ∼ 10 mK. The evaporative cooling of liquid helium is limited by the low vapour pressure below certain temperature. The lowest temperature that can be obtained by evaporative cooling of ^{4}He and ^{3}He are ∼ 1 K and ∼ 0.3 K respectively. Continuous cooling below 0.3 K is achieved in a dilution refrigerator by using mixture of ^{3}He and ^{4}He. This was first proposed by H. London, G. R. Clarke, and Eric Mendoza in 1962 [79] following H. London's idea [80]. Two years later Das *et al.* built the first dilution refrigerator and obtained a lowest temperature of 0.22 K [81]. Frossati has reported the lowest ever temperature recorded by a dilution refrigerator of ∼2mK in 1992 [82]. A custom designed cryogen free dilution refrigerator (CFDR1200), with cooling power of 1.4 mW at 120 mK, has been installed at TIFR for carrying out R&D on cryogenic bolometer [14]. In this chapter, after briefly discussing the basic working principle of a dilution refrigerator, the CFDR1200 setup is described. Maintenance and troubleshooting of CFDR1200 operation has been an integral part of the dissertation. Diagnosis and subsequent repair of few of the major issues are presented. The problem faced with the blockage in the helium gas circulation line and replacement of the *still* is discussed. An electronics readout and a NI based DAQ that has been set up for the development of a cryogenic bolometer using NTD Ge sensors is described.

2.2 Basic principle of a ^{3}He/^{4}He dilution refrigerator

It is well known that the pure ^{4}He has a nuclear spin of I = 0 and obeys Bose statistics. It undergoes a transition to superfluid at 2.177 K. With the addition of ^{3}He, the transition temperature of ^{3}He/^{4}He mixture decreases. Eventually, the superfluid transition of the mixture is completely suppressed at a ^{3}He concentration of $x = 67.5$ % and it meets a triple point at 0.87 K as depicted in Fig. 2.1 [54]. Below this temperature the mixture separates into two phases: a concentrated phase rich in ^{3}He and a dilute phase rich in ^{4}He. The concentration of ^{3}He in the dilute phase varies with temperature as

$$x = 0.066\,(1 + 8.3\,T^2) \tag{2.1}$$

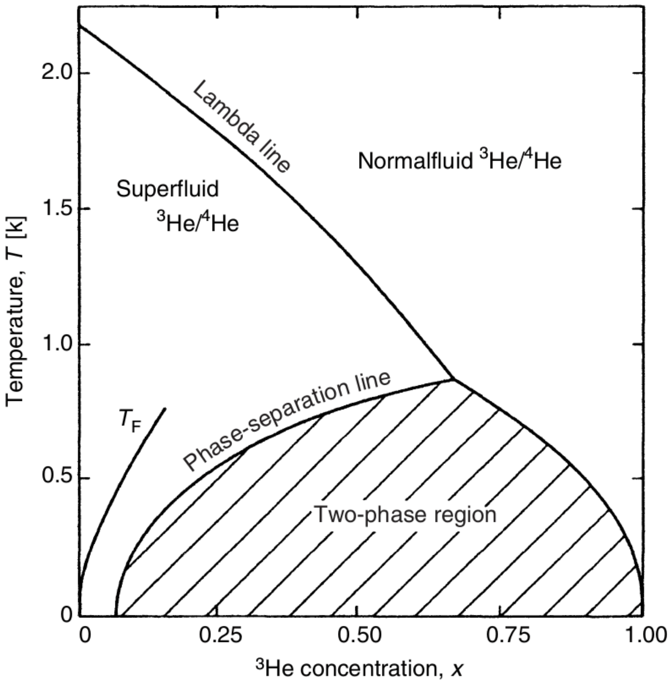

FIGURE 2.1: Phase diagram of a ^{3}He/^{4}He mixture at saturated vapour pressure [54]

Even at lowest temperature ($T \rightarrow 0$) there exists a finite solubility of ^{3}He of ~6.6%, which is the key element for the working of a dilution refrigerator. The ^{3}He rich phase floats on top of the dilute phase due to its low density. The viscosity, entropy and specific heat of superfluid ^{4}He is almost zero at $T < 0.5K$ with infinite thermal conductivity. Hence, it acts as an inert solvent for the ^{3}He in diluted phase. Also, the ^{3}He atoms in the diluted phase acts as a Fermi gas. If the ^{3}He atoms can be preferentially removed from the dilute phase, then ^{3}He atoms from the concentrated phase migrate into the dilute phase to maintain the equilibrium. This is analogous to the evaporation of ^{3}He liquid. Since the enthalpy of ^{3}He in dilute phase is larger than that of pure ^{3}He, it results in cooling. The cooling power can be expressed as

$$\dot{Q} = \dot{n}_3 \Delta H = 84 \dot{n}_3 T^2 \tag{2.2}$$

here ΔH is the difference in enthalpy between ^{3}He in dilute phase and pure ^{3}He and n_3 is the number of ^{3}He that crosses the phase separation line and dissolves into the dilute phase. A schematic representation of a ^{3}He/^{4}He dilution refrigerator is shown in Fig. 2.2 [54]. The mixing chamber (MC) is connected to a ^{3}He distiller (*still*) as shown in Fig. 2.2. The gas mixture is chosen such that the phase separation occurs at the MC and the pure ^{3}He liquid surface lies in the *still*. This is very crucial for a dilution refrigerator. A high throughput vacuum pump, typically

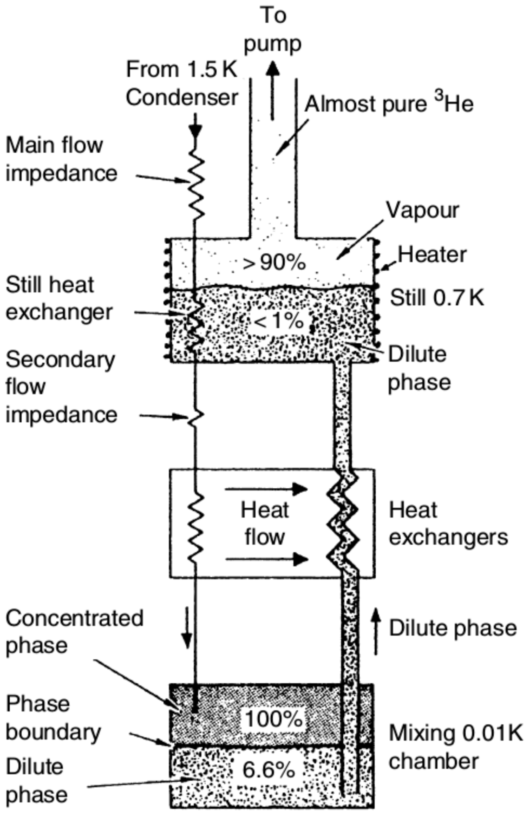

FIGURE 2.2: A schematic representation of a ^{3}He/^{4}He dilution refrigerator [54]

a turbomolecular pump backed by a roots pump, is used to pump the *still*. Since the vapour pressure of ^{4}He is significantly lower than the ^{3}He, mostly ^{3}He evaporates from the *still*. The room temperature gas is then purified via activated charcoal traps and added back to the concentrated phase in the *still* after liquefaction. The concentration of ^{3}He decreases in the concentrated phase when the *still* is pumped. This creates an osmotic pressure difference, which allows predominantly ^{3}He in the concentrated phase to reach the *still*. This process is repeated in a closed loop system for a continuous cooling. A heater is placed inside the *still* to control the ^{3}He flow rate. The circulation rate increases with *still* heater power, which in turn increases the cooling power following Eq.2.2. However, if the *still* temperature is too high, the ^{4}He vapour pressure becomes significant and the cooling power decreases. Typically the *still* temperature is maintained at 0.7 K - 0.8 K, which results in ~90% of ^{3}He in the circulation. The outgoing cold ^{3}He is used to cool the incoming ^{3}He via very efficient heat exchanger. A sintered silver heat exchanger is used below 50 mK and tube-in-tube heat exchangers is used for higher temperature.

2.3 CFDR 1200 setup for cryogenic bolomter

The dilution refrigerators can be classified into two categories a) Conventional Wet Dilution Refrigerator b) Cryogen Free Dilution Refrigerator (CFDR) [54]. While a liquid ^{4}He bath and 1 K pot is used in a wet refrigerator, a 3K heat exchanger followed by Joule-Thomson heat exchanger is employed in CFDR systems for condensing the helium gas mixture. The

3 K stage is maintained by means of a cryocooler. The CFDR was first made by Uhlig *et al.* employing Gifford-McMahon cooler (GM cooler) in 1993 [83]. The vibrational noise is significantly reduced when a pulse tube cryocooler is used instead of GM cooler. Soon after Uhlig's demonstration in 2002 [84], the pulse tube based CFDR bacame very attractive for underground experiments [85, 70, 69] with long runtime, owing to its easy, automatic and uninterrupted operation, and cost effectiveness as compared to wet refrigerator. Batey *et al.* have reported the lowest temperature of 3.253 ± 0.016 mK in 2014 [86] with CFDR. Review and details of development of CFDR can be found in Ref [87]. In spite of the above listed advantages, CFDR suffer from the vibrational noise induced by the pulse tube [88]. Several techniques have been developed to reduce pulse tube induced noise significantly [62, 89, 62, 90, 91, 92, 93, 94, 95, 96] and the CFDR is routinely used for bolometric application down to 10 mK.

A custom made high cooling power (1.4 mW at 120 mK) cryogen free dilution refrigerator (CFDR1200) is installed at TIFR [14] to facilitate R&D related to cryogenic bolometer operating at mK temperatures. The CFDR1200 setup at TIFR is shown in Fig. 2.3. The cryogen free design is chosen to carry out uninterrupted measurement over a long duration in an underground laboratory. In the CFDR 1200, the 40 K and the 3 K stages are cooled with the help of a two stage pulse tube cryocooler (Cryomech-PT415). The PT is rigidly mounted on room temperature, 40 K and 3 K plates. The compressor for the PT is placed in a separate room at a distance ~ 20 m from the cryostat to minimize the acoustic noise. Inlet pressure variation of the PT, between 100 and 300 psi with a frequency of

FIGURE 2.3: The CFDR1200 setup at TIFR.

1.4 Hz, is realized by a remote valve motor control unit which is mounted on a vibration damper and is rigidly fixed on top of a leg supporting the main cryostat. The valve motor control unit is detached from the PT and mounted on a vibration damper, situated on the top of the tripod supporting the cryostat, using a 65 cm long swan neck shaped bellow. It should be mentioned that the pulse tube valve control motor can be powered by a linear motor drive unit (LNX-G from Precision Motion Control 19 , Inc.), in lieu of the standard stepper motor drive resulting in less noise at temperature T < 100 mK. The linear motor drive ramps up the micro step current linearly instead of abruptly changing it, resulting less noise. In the CFDR 1200, the mixing chamber stage is protected from the radiation heat load by graded shielding at 50 mK, *still*, 3K and 50 K stage. The 50 K and the 3K shield is made up aluminum wrapped with multilayer mylar. The 3K shield is mounted with a kapton gasket which also forms the inner vacuum chamber (IVC). The volume between the room temperature container and the 3 K shield is referred as outer vacuum chamber (OVC). The *still* and 50 mK shields are fabricated using gold plated copper. The CFDR1200 has a large cylindrical sample space (30 cm diameter and 30 cm height) capable of supporting ∼100 kg mass at the mixing chamber (MC) and is provided with 300 readout wires enabling simultaneous measurement of 75 sensors in four wire readout scheme. The readout wires inside the cryostat are passed through ECCOSORB [97] and anchored at various places to reduce EMI noise and vibrational noise. A provision is also made for mounting electronics at 50 K plate for ultra-low noise applications. The CFDR1200 is placed inside a Faraday cage. The PT and various vacuum gauges are interfaced with the PC via an optically isolated RS232 adapter. It should be mentioned that the CFDR1200 is provided with a probe insert for quick sample changes. This is used for testing various sensors, heaters and measurement setups. A radiation shield is used in the absence of the probe insert. The temperature of the MC is measured using a Carbon Speer sensor calibrated against a CMN (Cerium Magnesium Nitrate) thermometer, which in turn is calibrated using a superconducting fixed point device (FPD). The materials used in the FPD and the corresponding tradition temperatures are given in Table. 2.1. The electronics setup for the control and diagnostics of the CFDR is shown in Fig. 2.4. The mixing chamber (MC) temperature is stabilized with a automatic PID (Proportional-Integral-Derivative) controller with a temperature stability of 0.1 %.

TABLE 2.1: Materials used in the FPD and corresponding transition temperatures.

Material	T_c (mK)
In	3300
Al	1175
Zn	840
Cd	520
$AuIn_2$	208
$AuAl_2$	161
Ir	97
W	15

FIGURE 2.4: The electronics setup for the control and diagnostics of the CFDR1200.

2.3.1 Operating procedure for the CFDR1200

Before starting the cool down procedure the IVC and OVC is evacuated to a vacuum level of $< 5 \times 10^{-2}$ mbar and $< 5 \times 10^{-3}$ mbar and flushed with pure ^{4}He and pure nitrogen respectively. The *still* and the condenser line is evacuated and flushed atleast three times with residual helium gas existing in the circulation line. After a base vacuum of $< 1 \times 10^{-4}$ mbar in the *still* is achieved, a throughput test is performed to assess the flow rate of the primary impedances. If high pressure gas is applied at the input of main flow impedance (see Fig. 2.2), then the still pressure would increase depending on the impedance of the condenser line. In normal operating condition it takes about 15 s for the still pressure to increase from 0.1 mbar to 1 mbar when about 1.3 bar of gas is applied at the input of the primary impedance. The liquid nitrogen pre-cooling and the PT cooling is started, after filling the IVC with pure ^{4}He gas of ~10 mbar. The system takes about 6-8 hours to reach ~ 85 K before the liquid nitrogen supply can be stopped. The 3 K stage reaches a temperature ~3 K in about another 6-8 hours. At this time the IVC vacuum is ($< 1 \times 10^{-4}$ mbar) due to cyo-pumping, due to which the still and the MC stage gets thermally isolated from the 3 K stage and remains at ~ 10 K. A current of 30 mA is applied to the sorb heater which deteriorates the IVC vacuum to $\sim 5-7\times10^{-2}$ mbar and helps the MC and the still to equilibrate with the 3 K stage. The sorb heater is them turned off for the IVC vacuum to recover. Once the IVC vacuum is $< 1 \times 10^{-4}$ mbar, the 4He and 3He gas is condensed. It takes about two hours to complete the condensation procedure. A complete thermal cycle, i.e., cooling down to mK temperature and vice versa is possible in the CFDR system within 48 hours, which makes it very elegent for R&D work.

2.3.2 Issues with CFDR1200 and repair

The CFDR1200 had a major problem when the ^{3}He circulation line developed a choke. It was observed during the throughput test that the *still* was taking almost few minutes to reach from 0.1 to 0.2 mbar only. The dilution unit comprising the 800 mK *still*, 50 mK heat exchanger and the MC, was completely dismantled to perform a systematic diagnosis. The choke was located in the secondary impedance below the *still*. To repair this, ~13 bar of ^{4}He gas was applied at the inlet of the secondary and the flow was monitored by observing the bubbling at the outlet as shown in the Fig. 2.5a. After the blockage was cleared, the dilution unit was reassembled with a new generation *still* containing pressure dependent primary impedances. A picture of the old and the new *still* is shown in Fig. 2.5b and Fig. 2.5c, respectively. After repairs, a detailed assessment of the CFDR was carried out by cooling power measurements. A cooling power of 1.36 mW at 120 mK was recorded with an optimum *still* heater current of 35 mA as shown in Fig. 2.6. After a few months of operation, it was found that the IVC


(a) (b) (c)

FIGURE 2.5: (a) Arrangements for diagnosing the blockage in the secondary impedance and subsequent repair, (b) The old *still* and (c) the new *still* showing the pressure dependent impedances

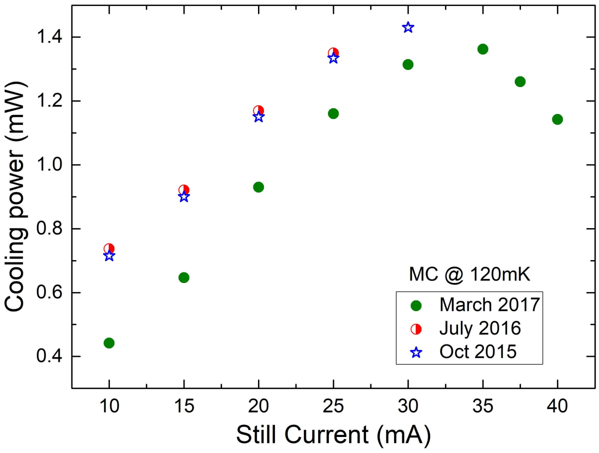

Figure 2.6: Cooling power vs *still* current before (green solid circle) and after (red half filled circle and blue star) the repair.

pressure increases during condensation and a leak in the ^{3}He circulation line was suspected. A systematic leak tests at room temperature was conducted to locate the leak in the *still* and condenser lines after removing the charcoal. The helium leak detector was connected at the exhaust of the turbo pump (S1) as shown in Fig. 2.7. The leak detector was operated in

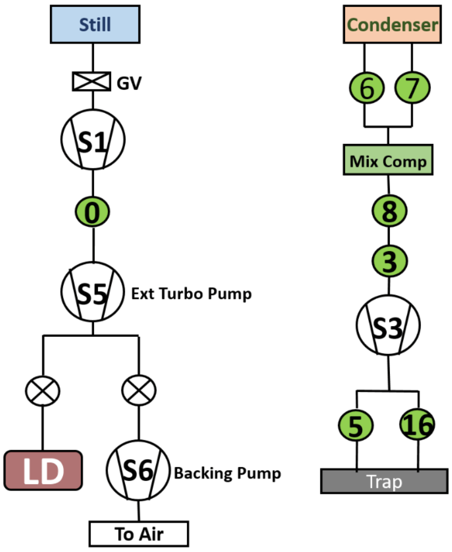

Figure 2.7: The configuration of the *still* and the condenser line used for the leak test

the vacuum mode with a background level of 8×10^{-7} mbar-l/s. When the IVC is filled with 15 mbar of He gas, the background rises rapidly to 1.3×10^{-6} mbar-l/s. A major Leak ($> 10^{-5}$ mbar-l/s) is found on the solder joint of the condenser line entering the sintered silver heat exchanger (see Fig. 2.8).

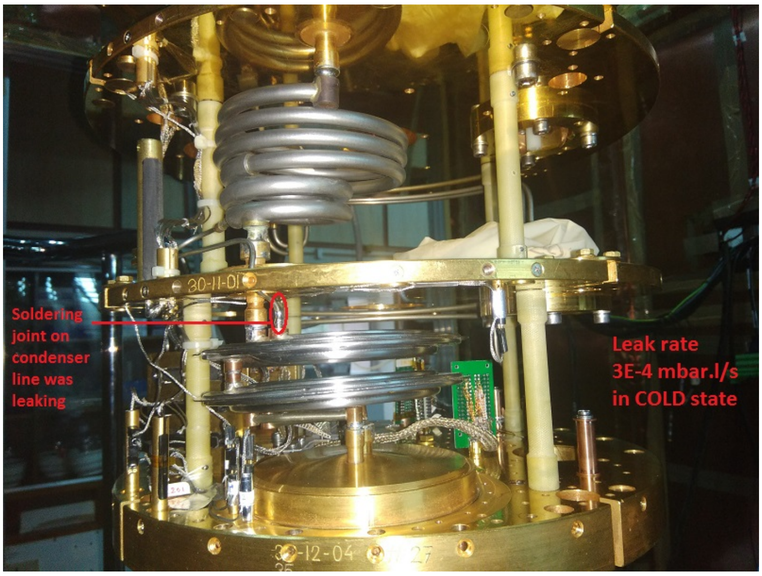

FIGURE 2.8: The dilution unit below the *still* showing the location of the leak

To repair the leak the solder joint was touched up with using a 50 W soldering iron. When the leak test was repeated, the background was found to be stable at 6×10^{7} mbar l/s even with 650 mbar He filled in the IVC.

2.4 Electronics readout and DAQ

Currently it is planned to use NTD Ge thermistors for measuring the temperature rise in the TinTin bolometers. For this, NTD Ge have been fabricated by irradiating high purity Ge wafer with thermal neutron in Dhruva reactor BARC, Mumbai [15]. Typical resistance of NTD Ge sensors at T <50 mK is ~100 MΩ to few GΩ. A commercially available *AC* resistance bridge AVS47B is used for measuring thermistor resistances upto 2 MΩ [98]. A very low noise and low excitation (fA to nA) electronics readout and DAQ is setup for measuring NTD Ge sensors of resistance $> 2M\Omega$. The readout electronics is shown in Fig 2.9. A NI based data

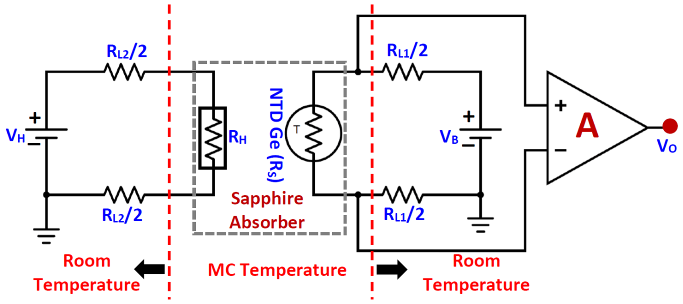

FIGURE 2.9: Electronics readout for cryogenic bolometer employing NTD Ge sensor

acquisition system, suitable for bolometer R&D, is developed employing LabView software [18]. The data acquisition system (DAQ) consists of a multi-function I/O Module (NI PXI-6281) housed in a NI PXIe 1082 chassis. The PXI-6281 has two single ended 16 bit DAC output channels and 8 differential 18 bit ADC input channels. The chassis is interfaced with the PC via a high-speed optical fiber. The output of a DAC channel is supplied to a pair of bias resistors connected in series with the NTD Ge sensor. The voltage across the sensor is amplified using a low noise (5.5 $nV/\sqrt{Hz}$), variable high gain (20 dB to 80 dB), high input impedance (1 TΩ) differential amplifier (Femto DLPVA-100-F) and the output of the amplifier is acquired using an ADC channel in PXI-6281. Measurements of current vs voltage (I-V) characteristics of the sensors at low temperatures (10-400 mK) are performed using customized data acquisition programs developed on the LabView platform. For acquisition over prolonged periods, software has a provision to automatically start a new file after preset interval (0.5 hour was used).A typical noise of $V_{PP} \sim 10$ mV is obtained in the amplified sensor output with 60 dB gain at temperature $T < 50$ mK.

2.4.1 Summary

The CFDR1200 setup at TIFR is described. Diagnostics and repair of the CFDR1200 for two major issues, a blockage and a leak in the helium circulation line is elaborated. After repair detailed assessments are performed. A cooling power of 1.36 mW is measured after the repair. A low noise (V_{PP} $\sim$ 10 mV) readout is setup with commercially available amplifier. A DAQ system suitable for bolometer R&D is developed employing LabView.

CHAPTER 3

NTD Ge sensors for *Tin.Tin*

3.1 Introduction

NTD Ge sensors are widely used as low temperature sensors owing to high sensitivity, low specific heat, good reproducibility. These sensors are preferred for a wide dynamic range and relatively simpler readout compared to other temperature sensors like TES or MMC. As mentioned in the first chapter, many experiments studying rare decays like neutrinoless double beta decay and dark matter studies using large arrays of calorimetric detectors have employed NTD Ge as the temperature sensor. NTD Ge is produced by irradiating high purity Ge wafers with thermal neutrons in a nuclear reactor. In ^{nat}Ge samples, thermal neutron capture by various isotopes leads to production of Ga, As, Se and results in p - type Ge [99] as shown in the Table 3.1. As compared to conventional metallurgical methods, more uniform and precise doping can be achieved in the NTD technique due to the moderate neutron capture cross section of Ge. An

Table 3.1: Natural isotopes of Germanium and n-capture products [26], [100].

Isotope	Abun. (%)	σ_c (barn)	Product	$T_{1/2}$
^{70}Ge	20.4	3.43	^{71}Ga	11.43d
^{72}Ge	27.3	0.98	^{73}Ge	stable
^{73}Ge	7.8	15.0	^{74}Ge	stable
^{74}Ge	36.7	0.51	^{75}As	82.78m
^{76}Ge	7.8	0.16	^{77}Se	11.3,38.8h

overview of properties of NTD Ge sensors can be found in Ref. [19]. The variation of resistance of NTD Ge sensor at low temperatures is well explained by the variable range hopping mechanism and expressed as [56]

$$R = R_0 \, exp \left[\frac{T_0}{T} \right]^{\alpha} \tag{3.1}$$

where R_0 depends on intrinsic properties of Ge, T_0 depends on the doping level and constant [101] $\alpha \sim 0.5$. The performance of NTD Ge sensor at ultra-low temperature depends on several factors like thermal contact to the heat bath, strain/stress in the sensor, mounting arrangement, surface quality, and electrical contacts. Further, minimization of radioactive background arising due to neutron irradiation of impurities in NTD Ge fabrication is of paramount importance. This makes the fabrication and testing of NTD Ge sensors, intended for rare decay studies with bolometer operating at mK temperature, very challenging. The fabrication of ohmic contact at the metal semiconductor junction at mK temperature is very essential for the functioning of NTD Ge sensors. Li [102] describes different techniques for ohmic contact formation in semiconductors. Boron ion implantation followed by Au film deposition is commonly used for making electrical contacts in NTD Ge sensors owing to low contact noise [103]. While this is desirable for mass production, alloying or evaporation is simpler and faster at R&D stage.

As mentioned earlier, in India, development of NTD Ge sensors for use in TIN.TIN has been initiated [8, 15]. The preliminary results for indigenously fabricated NTD Ge sensors have been reported by Mathimalar et al. [15]. As a part of this thesis work, various improvements in NTD Ge fabrication have been carried out. Several irradiations (13 batches) were carried out at Dhruva reactor, BARC, Mumbai with an aim to achieve the desired neutron fluence of $\sim 4 \times 10^{18}/\mathrm{cm}^2$, which was shown to be the optimum dose suitable for NTD sensors in 10-100 mK range [12]. In some cases, an independent estimate of the thermal neutron flux was obtained using a monitor sample of ^{nat}Zr. The irradiated ^{nat}Zr samples have been studied in the TIFR Low background Experimental Setup (TiLES) [104] and the thermal neutron flux is estimated from the activity of ^{95}Zr. In some cases, internal impurity of ^{123}Sb in the device grade Ge sample (119 ± 7 ppt), is also used to verify the thermal neutron flux [16]. Neutron irradiation of the Ge sample leads to significant levels of long-lived radioactive impurities on surface and could be removed by chemical etching $\sim 50\mu m$ of the NTD Ge [16]. In the present work, effect of etching of the Ge samples prior to irradiation is studied. To improve the surface quality of the irradiated wafer, optical finish polishing is done at the final stage, i.e., after post-irradiation chemical etching. The mask for depositing AuGe is modified for a wrap around contact, which ensures parallel electric field inside the sensor. This mask can be used for a batch fabrication of upto $\sim$ 150 sensors. Fabrication and testing of NTD Ge sensors of smaller dimensions (2×2 mm^2 and 1×1 mm^2) which are expected to have less heat capacity contribution to the bolometer absorber is performed. Details are described in the following sections.

3.2 Neutron irradiation of Ge

Ge samples (< 100 > n - type, 1 mm thick) from two manufacturers with different purity level have been irradiated with thermal neutrons at Dhruva reactor BARC to fabricate NTD Ge sensors. The device grade Ge (5N purity) is from M/S University Wafer (Grade-I) [105] and is single side polished (SSP), while the detector grade (13N purity) is from M/S Umicore(Grade-II) [106] and is not polished on either side to study the effect of surface impurities due to polishing. The Ge samples were cleaned with HF (40 %) to remove the oxide layer, rinsed with de-ionized water and finally blow dried with dry N_2 prior to thermal neutron irradiation. Typically, 10 mm × 30 mm samples are cut from a 2" wafer and wrapped in an aluminum foil for the irradiation. The thermal neutron fluence estimated from the reactor power (ϕ_R) of different samples is given in Table. 3.2

TABLE 3.2: Thermal neutron fluence estimated from the reactor power.

Sample	Average thermal neutron flux (cm^{-2} s^{-1})	duration (day)	ϕ_R (cm^{-2})
D	–	–	$4.57 \times 10^{18*}$
E	0.6×10^{13}	4.1	2.11×10^{18}

*Data was retrieved from Hall effect measurement

Continued on next page

Table 3.2 – *Continued from previous page*

Sample	Average thermal neutron flux (cm^{-2} s^{-1})	duration (day)	ϕ_R (cm^{-2})
F	0.6×10^{13}	6.8	3.52×10^{18}
G	0.6×10^{13}	6.9	3.57×10^{18}
H,I	0.6×10^{13}	3.5	1.8×10^{18}
J	0.5×10^{13}	6.9	2.98×10^{18}
K,L	0.6×10^{13}	6.8	2.45×10^{18}
M,N	0.6×10^{13}	6.8	2.99×10^{18}
O	2.9×10^{13}	2.1	1.57×10^{18}
P	4.4×10^{13}	2.1	2.39×10^{18}
Q,R	0.6×10^{13}	6.8	3.52×10^{18}
V	1.5×10^{13}	7.8	4.64×10^{18}
W	0.6×10^{13}	6.8	2.28×10^{18}
AA-AD	0.6×10^{13}	12.3	5.49×10^{18}

The irradiated samples were allowed a typical cool-down period of about 45 days.

3.2.1 Estimation of thermal neutron flux from ^{nat}Zr activity

In order to obtain an independent estimate of the thermal neutron flux, ^{nat}Zr is used in some of the irradiations. ^{nat}Zr can be used as thermal and epithermal neutron monitors [107, 108, 109]. ^{nat}Zr contains ^{94}Zr with an isotopic abundance of 17.4 %. The ^{94}Zr isotope produces radioactive ^{95}Zr through (n,γ) reaction which emits characteristics γ-rays of energy 724.2 keV with a half life of 66.032(0.006) days [26]. The neutron fluence ϕ_{Zr} can be obtained from the activity of ^{95}Zr using the following equation

$$\phi_{Zr} = \frac{\lambda N_d t_{ir}}{N_p(1 - e^{-\lambda t_{ir}})\sigma_c} \tag{3.2}$$

where N_p is the number of parent isotope (^{94}Zr), N_d is the number of daughter isotope (^{95}Zr), λ is the decay constant of ^{94}Zr and σ_c = 50 mb is the cross section for the reaction and t_{ir} is the duration of neutron irradiation.

The irradiated ^{nat}Zr samples were counted in the TiLES [104] initially at 10 cm and in a close geometry for higher efficiency. Data was recorded using a commercial CAEN N6724 digitizer (14-bit, 100 MHz). The analysis is performed using LAMPS software and ROOT framework. Figure 3.1 shows the gamma-ray spectra of Zr sample in a close geometry (on face) counted for a period of 6 h in the TiLES. For unambiguous identification, half-life ($T_{1/2}$) of the observed gamma ray is measured and a half-life of 66(3) days was obtained which is in good agreement with the literature value (64.032 d [26]). The thermal neutron flux is estimated from the activity of ^{95}Zr, using equation 3.2. In addition, the ^{124}Sb impurity (119 ± 7

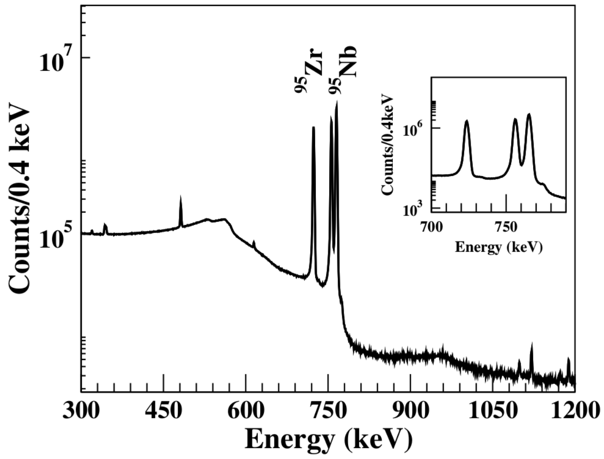

Figure 3.1: Gamma-ray spectra of neutron irradiated Zr sample (N2) in a close geometry in the TiLES (counting time = 6 h). The inset shows the gamma rays of interest.

ppt) is observed in some NTD Ge sample (Grade-I), which is used to estimate the thermal neutron fluence (ϕ_{Sb}) [16]. Also, for a few samples, neutron fluence (ϕ_H) were deduced from Hall Effect measurements [110]. Neutron fluence obtained using different techniques are summarized in Table 3.3 for comparison. Large discrepancies are seen for samples J, M and Q sample. For the samples E and H, ϕ_R is in reasonable agreement ($\sim$ 10 %) with ϕ_H. For M sample neutron flence estimated from ^{124}Sb and from ^{95}Zr activity agrees within 10%. Hence, neutron fluences estimated form Zr/Sb activity are used for carrier concentration estimates.

TABLE 3.3: Neutron fluence estimated from different methods. All the neutron fluence values are in the unit of cm^{-2}

Sample	ϕ_R	ϕ_H	ϕ_{Sb}	ϕ_{Zr}
D	–	4.57×10^{18}	4.26×10^{18}	–
E	2.11×10^{18}	1.8×10^{18}	–	–
F	3.52×10^{18}	–	3.35×10^{18}	–
G	3.57×10^{18}	–	3.88×10^{18}	–
H	1.8×10^{18}	–	1.62×10^{18}	–
I	1.8×10^{18}	1.72×10^{18}	1.73×10^{18}	–
J	2.45×10^{18}	–	8.18×10^{18}	–
M	2.99×10^{18}	–	4.28×10^{18}	3.79×10^{18}
N	2.99×10^{18}	–	–	3.65×10^{18}
Q	3.52×10^{18}	2.9×10^{19}		2.24×10^{19}
R	3.52×10^{18}	–	–	2.18×10^{19}
V	4.64×10^{18}	–	–	8.42×10^{18}
W	2.28×10^{18}	–	–	2.77×10^{18}

3.3 Improvements to sensor fabrication

3.3.1 Chemical etching prior to irradiation

We have earlier reported that the neutron irradiation of the Ge sample leads to significant levels of long-lived radioactive impurities, which can be removed by chemical etching $\sim 50\ \mu m$ of the NTD Ge [16]. However, Ge wafers can have trace impurities due to cutting and polishing process. Therefore Grade-I SSP samples (where polishing is expected to leave more residual impurities) were chemically etched to remove 20-40 μm thickness. Chemical etching of the samples was done using H_2O_2 at 80^0C in an ultrasonic bath. All the Ge samples were then cleaned and prepared for neutron irradiation using the technique as described in section 3.2. Details of various samples are given in Table 3.4.

Table 3.4: Details of Ge samples studied

Name	Grade	ρ (Ω-cm)	Surface	Mass (mg)	Etched depth (μm)
R1	device	30	SSP	556.5	0*
R2	device	30	SSP	1015.0	20
R3	device	30	SSP	1141.6	40
R4	detector	1.6×10^5	-	1429.2	0*

* Etched depth = 0 μm represents not etched samples.

The irradiated Ge samples were counted with an efficiency calibrated standard HPGe detector (30% relative efficiency), shielded with 5 cm thick Pb. Fig. 3.2 shows the gamma-ray spectra of the irradiated Ge samples (R1, R2) counted in a close geometry for a period of 4 h. It can be seen that etching the samples prior to irradiation reduces the level of radioactive nuclides. The comparison of the two different grades of the irradiated Ge samples is shown in Fig. 3.3. Each spectrum has been normalized to

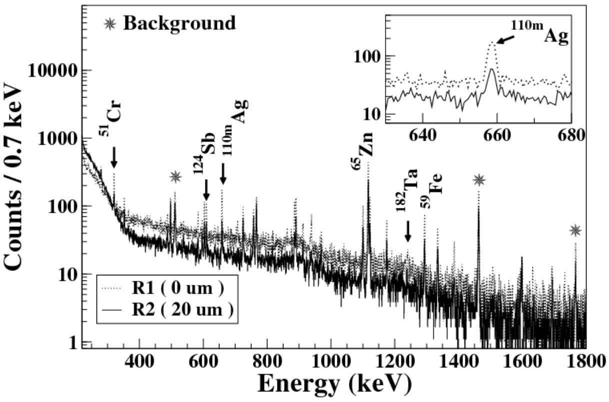

Figure 3.2: Gamma-ray spectra of the irradiated Ge samples (R1, R2) counted in a close geometry. The inset shows the expanded region of ^{110m}Ag

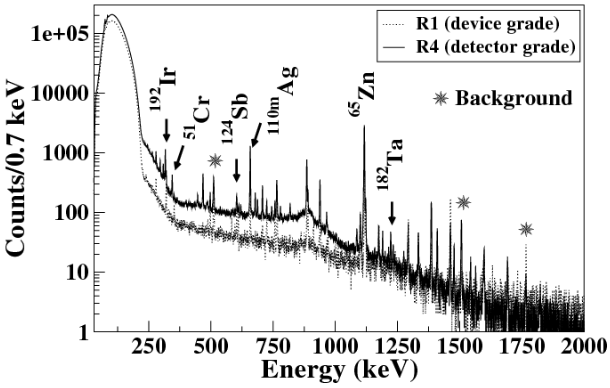

FIGURE 3.3: Gamma-ray spectra of the irradiated Ge samples (R1, R4) counted in a close geometry.

TABLE 3.5: Impurity levels observed in the R2, R3, R4 samples w.r.t. the R1.

Isotope	$T_{1/2}$	E_γ (keV)	A_2	A_3	A_4
^{51}Cr	27.7 d	320.1	0.33(5)	0.30(5)	0.5(3)
^{124}Sb	60.2 d	602.7	0.6(1)	0.6(1)	1.6(3)
^{110m}Ag	249.76 d	657.8	0.25(4)	0.19(3)	4.3 (6)
^{46}Sc	83.79 d	889.3	0.43(4)	0.47(4)	0.58(7)
^{59}Fe	44.5 d	1099.3	0.48(6)	0.40(5)	0.9(1)
^{65}Zn	243.66 d	1115.5	0.56(3)	0.40(2)	3.6(2)
^{60}Co	5.27 y	1173.2	0.62(2)	0.6(1)	72(12)

the mass of the R1 sample. The R4 sample showed overall higher levels of activity and also additional ones like ^{192}Ir ($T_{1/2}$ = 73.8 d). Table 3.5 gives the observed levels of the impurities in the different samples in comparison with R1 (the pristine device grade sample). That is, A_i is the ratio of counts observed in the i th sample w.r.t. the counts in the R1 sample for the corresponding gamma ray. It is evident that the etching of the Ge samples prior to irradiation resulted in reduction of the impurity levels by 40-80%. The detector grade Ge wafer (R4), which has much higher resistivity, showed higher concentrations of long-lived nuclides like

^{110m}Ag, ^{124}Sb, ^{65}Zn, ^{60}Co. However, on etching this sample by 20 μm, no activity above the sensitivity level of the counting setup was observed implying that the activity in irradiated R4 sample is due to the surface impurities. Hence, chemical etching prior to irradiation is required even for the Grade-II samples which are not polished.

3.3.2 Fabrication of NTD Ge sensors

As mentioned in section 3.3.1, the irradiated Ge wafers are chemically etched (~ 50 micron) to remove the radioactive surface impurities. After etching, the samples are annealed at 600 ^{o}C for two hours in a vacuum sealed quartz tube to recover the fast neutron induced damage in the Ge crystal lattice structure [110] before it is taken for further processing. During the course of the work, NTD Ge sensor of different dimension with different electrical contact geometry were made and a schematic along with the mounting scheme is shown in Fig. 3.4. The electrical contacts were made by sputtering ~ 200 nm thick Au-Ge alloy (88% Au + 12% Ge) using a suitable mask. Rapid thermal annealing at 400 ^{o}C for 2 minutes in Ar atmosphere for the Au-Ge atom to make a metalized contact pad. The

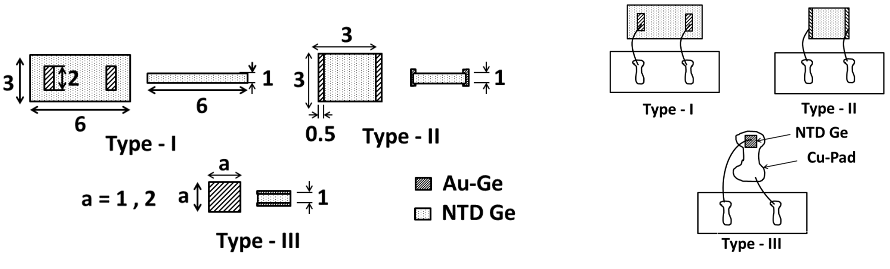

FIGURE 3.4: Schematics for Different types of sensor and their mounting scheme

Type-I sensors are relatively larger in size and are appropriate for R&D in initial stage as it's simpler to make and easy to handle. The electronic heat capacity of NTD Ge sensor varies linearly with temperature ($c = \gamma$ T) and can contribute significantly at mK temperature when used in a small size bolometer [17]. Hence, the reduction of the sensor size is very important for such bolometers, to achieve a better energy resolution. Moreover, the electrical contact in the Type-I sensor is deposited on the same surface which will result in a non uniform electric field when biased. Also, the Type-I sensors are processed individually and this method is therefore economically inefficient. A process aiming for batch fabrication of sensor is required. With this motivation, fabrication and characterization of smaller size sensors (Type-I and Type-II) with contact geometry ensuring parallel electric field was carried out. The impurities on the surface of a NTD Ge can alter the behaviour at mK temperature. Hence, to avoid any surface impurity, NTD Ge sensor is polished to optical finish surface after the chemical etching. Some pictures showing various steps of fabrication are shown in Fig. 3.5.

A schematic picture of the sensor mounting arrangement on a cylindrical gold-plated copper holder (ϕ = 45 mm, h = 13 mm) is shown in Fig. 3.6. The Type I and Type II sensors were mounted on the copper holder using a thin layer of GE-Varnish on a rolling paper to provide electrical insulation. Type III sensors were mounted on copper pad using electrically conducting silver paste which in turn is mounted on the copper housing using a thin layer of araldite. For electrical readouts a circular PCB with 12 pin female SMD connector was mounted on the copper holder. For Type-I and Type-II

FIGURE 3.5: Clockwise from left top, Teflon made fumehood for the chemical etching, mechanical poslishing setup with different smoothness, mask for making Au-Ge contact and the wire bonding machine for making electrical readout with Al wire.

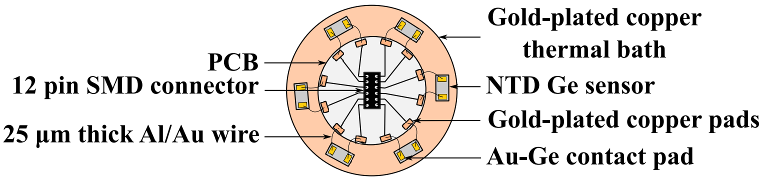

FIGURE 3.6: A schematic picture of the experimental setup used for sensor tests.

sensors, thin Al wires (ϕ = 25 μm) were wedge bonded from each Au-Ge contact pad on the sensor to the PCB, while Al wires were bonded on the top surface and the copper pad in case of Type-III sensor (see Fig. 3.4). Twelve shielded cables, each having a twisted pair of NbTi wire originating from a 24 pin molex connector, were connected to a 12 pin male SMD connector. The setup was enclosed in a gold-plated annular copper cylinder for EMI shielding and mounted on the CFDR 1200 probe which acts as a thermal bath for the sensors. The low-temperature measurements were performed in CFDR-1200 setup as described in Chapter 2.

3.3.3 Characterization of NTD Ge sensors

The block diagram of the electronics using differential I/O stages, implementing the four wire resistance measurement for testing of Type-I sensor is shown in Fig. 3.7. To obtain *V-I* curves, current from a commercial low noise current source (CSE09NV [111], range ± 1 nA) was varied and the corresponding amplified voltage signal (gain = 100) was measured. A low pass digital filter (cutoff = 10 Hz) was used to reduce the noise in the voltage measurements. Type-II and Type-III sensors are characterized using the electronics readout as described in Chapter 2. Measurements were performed with both polarities of the bias current in order to eliminate the voltage offset due to thermoelectric effect. The current source and the voltage amplifier were powered by dc batteries to minimize 50 Hz noise. For studying R as a function of T, mixing chamber was stabilized at a selected temperature (within 0.1 %) with a PID controller and the sensors were allowed to equilibrate thermally. Fig. 3.8 shows *V-I* data of the

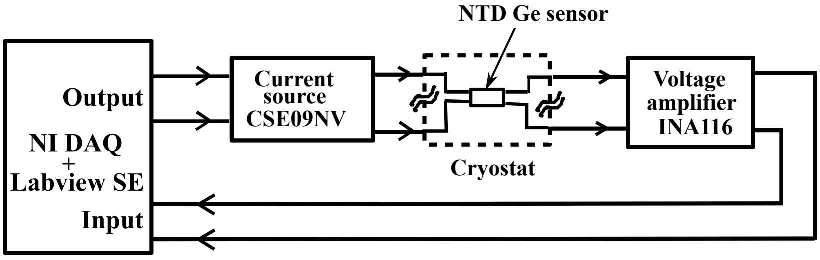

FIGURE 3.7: Block diagram of readout electronics using NI based DAQ for measuring R upto 10 GΩ.

Type-I and Type-II sensor. For Type-III sensors, *V-I* measurement was not performed and the resistance was measured with square wave excitation. Schottky barrier like behavior was observed for higher bias current as seen in Fig. 3.8. This could be due to the self-heating at higher bias current and implies the need for improving thermal contact. Hence resistance values in all measurements were extracted from the slope at the origin (low bias current). It should be pointed out that the nonlinear behavior in the *V-I* curves of NTD Ge sensor was reported earlier by Wang *et al.* [112] and explained in terms of thermal decoupling between the electrons and the phonons.

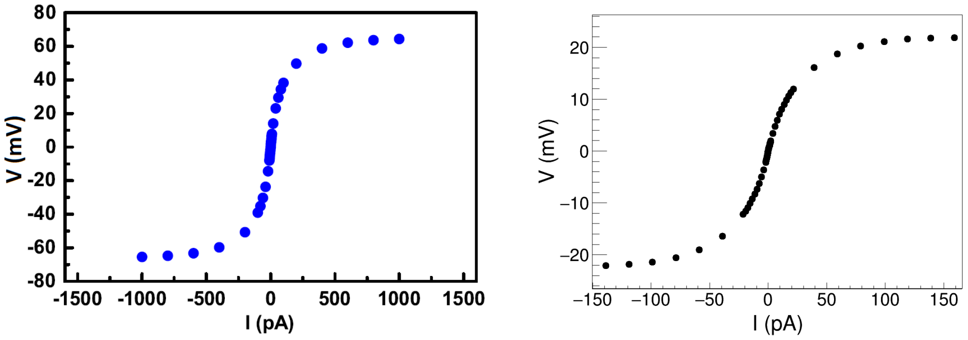

FIGURE 3.8: Voltage as a function of bias current for Type-I sensor at 25 mK and Type-II sensor at 10 mK.

Resistance of different types of sensors are plotted in Fig. 3.9 (*Left panel*). The variation of ln R vs $1/\sqrt{T}$ together with the fitted function (Eq. (3.1)) is shown in Fig. 3.9 (*Right panel*). The extracted parameters T_0 and R_0 are listed in Table 3.6. To check the reproducibility, multiple sensors of Type-II and Type-III were characterized and the T_0 and R_0 values are listed in Table. 3.7.

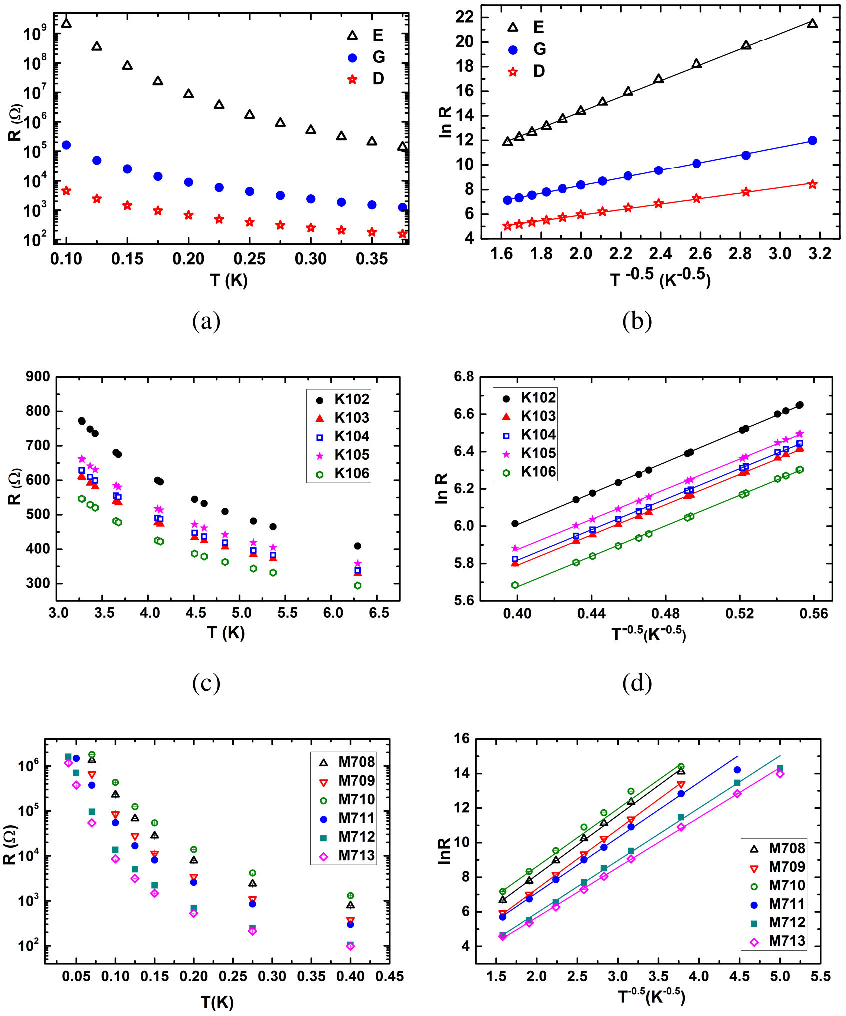

(a) (b)

(c) (d)

(e) (f)

FIGURE 3.9: (a), (c) and (e) are R vs T for Type-I, Type-II and Type-III sensor respectively and (b), (d) and (f) are the corresponding ln R vs $T^{-0.5}$ plot together with fits to Eq. (3.1)

TABLE 3.6: Extracted R_0 and T_0 values for sensors having different carrier concentration

Sample	Carrier concentration (/cm^3)	$R_0(\Omega)$	T_0(K)
D	1.11×10^{17}	4.3 ± 0.3	4.9 ± 0.2
G	8.68×10^{16}	7.9 ± 0.5	9.8 ± 0.2
E	5.13×10^{16}	4.5 ± 0.9	41 ± 1
K	5.95×10^{16}	66 ± 2	16.7 ± 0.5
M	7.26×10^{16}	2.6 ± 1.3	10.2 ± 1.0

TABLE 3.7: verification of constancy of R_0 and T_0 of multiple K sensors (Type-II) and M sensors (Type-III)

Sensor	Area (mm^2)	T_0(K)	$R_0(\Omega)$
K102	3×3	76 ± 1	17.5 ± 0.2
K103	3×3	64 ± 1	16.5 ± 0.2
K104	3×3	65 ± 1	16.3 ± 0.2
K105	3×3	70 ± 1	16.3 ± 0.2
K106	3×3	56 ± 1	16.7 ± 0.3
M708	1×1	3.4 ± 0.4	11.9 ± 0.4
M709	1×1	1.5 ± 0.1	11.9 ± 0.1
M710	1×1	6.9 ± 1.2	11.2 ± 0.5
M711	1×1	2.0 ± 0.4	10.2 ± 0.5
M712	2×2	0.9 ± 0.2	9.2 ± 0.3
M713	2×2	0.9 ± 0.1	8.3 ± 0.2

It can be seen that even though the sensors are of very similar geometry, fitted values of R_0 are different which can arise due to contact, surface effect etc. Also, Wang *et al.* [112] suggested that residual stress, unannealed radiation damage and dislocations may also cause this variation at very low temperatures. It should be pointed out that dR/dT (i.e., T_0) shows expected dependence on doping level. The variation in T_0 for Type-II and Type-III sensors is ± 5 % and ± 15 %, respectively. The behaviour of a Type-II NTD Ge sensor, made from the D-set (DB31) down to 10 mK is shown in Fig. 3.10. It can be seen that ln R can be fitted linearly

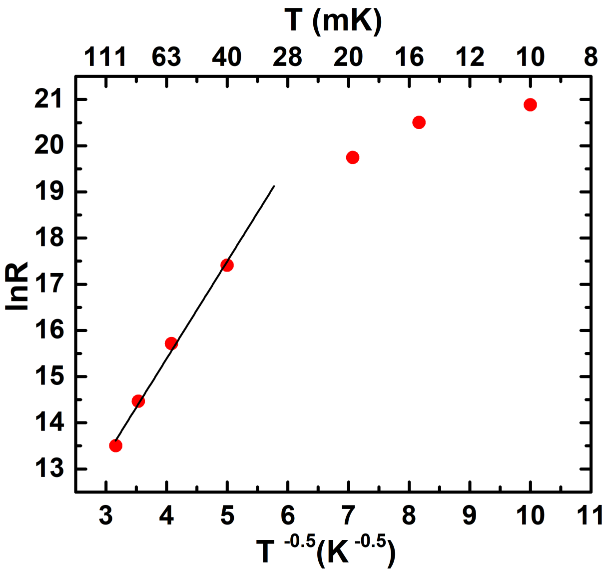

FIGURE 3.10: ln R vs $T^{-0.5}$ together with fits to Eq. (3.1) (shown by *solid line*) for DB31 sensor in the temperature range 10 mK – 100 mK

with $T^{-0.5}$ following equation 3.1 down to ~30 mK. However, below this temperature a deviation from the equation 3.1 is observed. This could be due to surface impurities which can provide leakage path and can alter the measured resistance at low temperature. It should be noted that even though it deviates from the Mott-like behaviour, dR/dT is finite and the sensor can be used upto 10 mK with empirical function. D sensors are used for bolometer tests (described in Chapter 5)

3.4 Summary

Neutron Transmutation Doped (NTD) Ge sensors have been prepared by irradiating device grade Ge with thermal neutrons at Dhruva research reactor, BARC, Mumbai and are intended for use in TIN.TIN. Neutron fluence is estimated from the activity of ^{nat}Zr samples which were irradiated along with Ge samples for few irradiations. For a particular sample the obtained value could be compared with the measurement using ^{124}Sb activity which agrees within 10%. The neutron fluence obtained form Zr/Sb activity was found to be more reliable than that obtained from the reactor power.

It is shown that etching of the Ge samples prior to irradiation resulted in reduction of the surface impurity levels by 40-80%. NTD Ge sensors of different sizes have been fabricated and characterized. A neutron fluence of 4-5 $\times 10^{18}$ is found to be optimum for use as a bolometer sensor operating at temperature of 10 mK. Sensors of smaller dimension (2×2 mm^2 and 1×1 mm^2) have also been made and have shown promising results up to 40 mK. NTD Ge sensors fabricated using improved technique are shown to be useful upto 10 mK with a Mott-like behaviour upto 30 mK.

CHAPTER 4

Heat capacity measurement of polymers

4.1 Introduction

Thermal properties of amorphous organic polymers make them particularly attractive for structural applications at very low temperatures. Compared to metals, the polymers have high strength to weight ratio, low thermal conductivity and smaller heat capacity at cryogenic temperatures. They are particularly suitable for low temperature detectors (operating at $T \sim 10\,\mathrm{mK}$) where polymeric materials are used as structural supports for the detector elements [113, 114, 115, 116]. While thermal conductivity determines the time scale over which the detector element thermalizes with the temperature bath, a high heat capacity material can severely deteriorate the resolution of the detector since one third of the heat capacity of the thermal link contributes to the total heat capacity of the calorimetric detector [20].

However, there is little or no data for thermal conductivity and specific heat for most of the polymers at the detector operating temperature (typically $\sim$ few tens of millikelvin). In the present work the specific heat of Teflon (commercial grade), Torlon - 4203 and Torlon - 4301 (polyamide-imide; Solvay Advanced Polymers) has been measured in the temperature range of 30 - 400 mK. Torlon - 4203 nominally contains 3% TiO_2 and 0.5% fluorocarbon while Torlon - 4301 contains 12% graphite powder and 3% fluorocarbon [117]. Teflon is widely used as polymeric support for massive calorimetric detectors but its specific heat data exists only in the range of 0.3 - 4.2 K [118]. Torlon is studied since it has better mechanical properties like lower thermal expansion coefficient and higher tensile and compressive strength than Teflon. While the specific heat of Torlon - 4203 has been reported in the literature in the temperature range of 0.15 - 4.2 K [119], no such data exist for Torlon - 4301. The present work reports the specific heat of Torlon - 4301 for the first time while extending the calorimetric data to lower temperatures for Teflon and Torlon - 4203.

4.2 Experimental Details

Thermal relaxation calorimetric technique was used to measure the heat capacity of small samples [20, 54, 120, 121, 122]. The setup for measuring the heat capacity is shown in Fig. 4.1. It comprises a sapphire platform (15 mm x 12 mm x 0.4 mm) on which the samples were mounted. The platform was mounted on three hollow cylindrical Teflon supports ($l \sim 5$ mm; $\phi_{outer} = 5$ mm and wall thickness $\sim$ 1 mm) which provided the weak thermal link between the platform and the thermal bath.

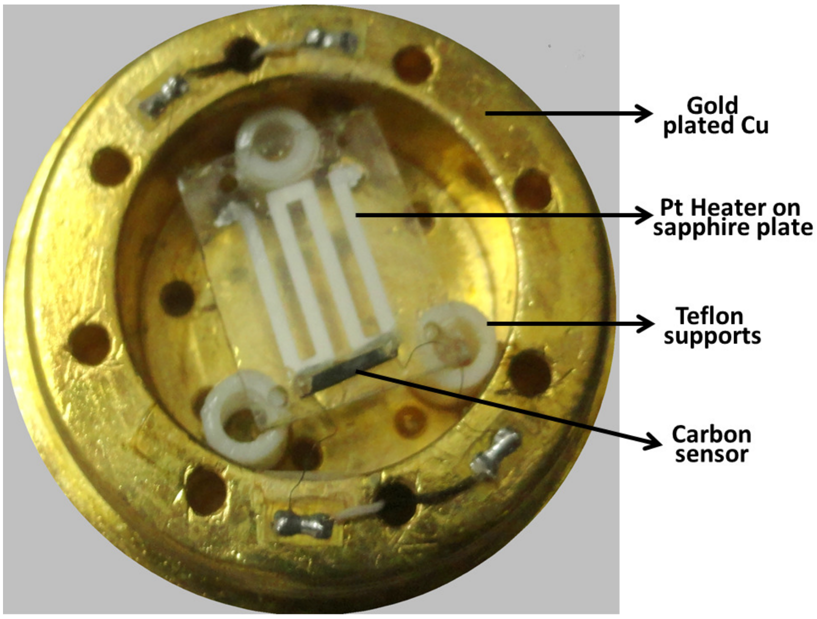

FIGURE 4.1: The setup used to measure the heat capacity of the polymer samples. The sample masses and the Teflon support links were chosen such that the total decay time constant for the relaxation curve was of the order of 5 - 20 secs.

A Platinum thin film of thickness $\sim 50nm$ was deposited on the sapphire platform which acted as a heater. Platinum is used because of it is resistive to oxidation and has better adhesive properties compared to gold. A carbon based thermistor has been fabricated for the temperature sensor as suggested by Samkharadze *et al.* [123]. The phenolic package of a 10 Ω carbon resistor (from Ohmite Manufacturing Co.) is removed and the carbon resistor is thinned down to a thickness of $\sim$ 0.4 mm by polishing. The carbon sensor is stuck to the sapphire using a thin layer of low temperature araldite. Copper cladded NbTi wires (80 micron diameter) are used for making electrical connection to the heater and the sensor. To reduce the heat capacity addendum the copper cladding is etched except at the two ends of the wire. These wires are bump bonded to the heater with indium and attached to sensor with a tiny amount of silver paste. Since NbTi becomes super conducing below ~ 10 K, the power dissipation in the readout wires is negligible.

Fig. 4.2 shows a block diagram of the heat capacity measurement system. The heater current was supplied by a Keithley 220 programmable current source and an AVS 47B a.c resistance bridge was used to measure the change in the resistance (sampling rate ~ 2.5/sec). The measurements were carried out in a high cooling power (1.4 mW at 120 mK) cryogen-free dilution refrigerator setup at TIFR, Mumbai [14] as described in Chapter 2. To calibrate the carbons sensor, the mixing chamber temperature was stabilized at different temperature range of 30-400 mK with an automatic PID controller and the resistance of the carbon sensor (R_C) and temperature of the probe was recorded. The temperature of the probe is measured using a calibrated RuO_2 sensor. To avoid error due to thermal cycle, the carbon sensor was calibrated for both heating and cooling cycle and the data was fitted with a polynomial of order 9 as shown in the Fig. 4.3.

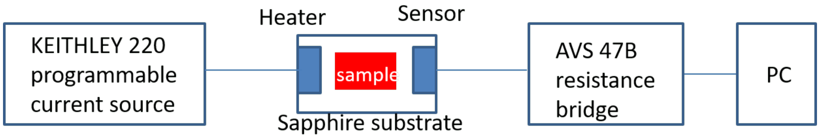

FIGURE 4.2: A block diagram for the measurement system.

Table 4.1 gives details of sample sizes and masses. The samples were stuck on the sapphire platform using a thin layer of GE-Varnish. The contribution

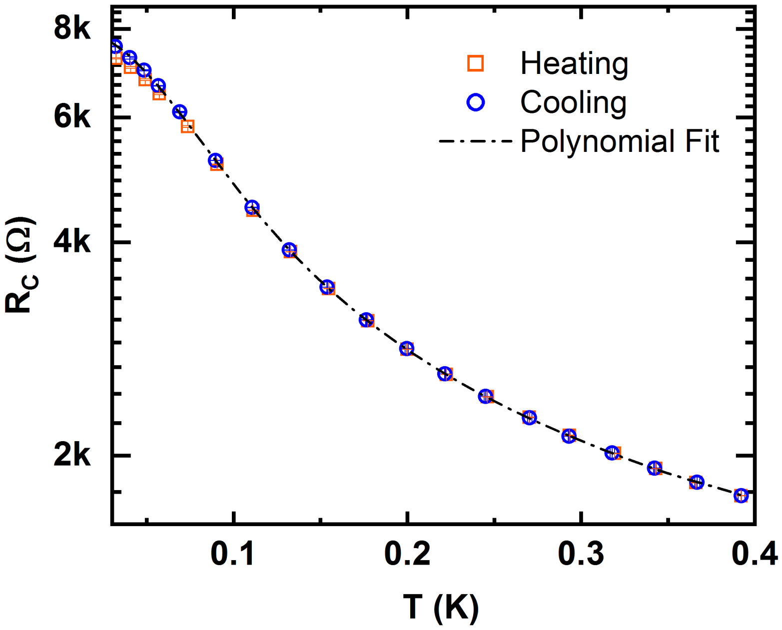

FIGURE 4.3: Calibration of the carbon sensor against the probe temperature.

of the thin layer of GE-Varnish to the measured heat capacity is estimated to be negligible [124]. The thermal conductance of the layer is also estimated to be sufficient for the sample to equilibrate with the sapphire platform when a steady state condition is reached.

TABLE 4.1: Sample Details

Sample	Mass (g)	Size
Teflon	2.5460	12 x 12 x 7 mm^3
Torlon - 4203	1.5267	8 x 7 x 6 mm^3
Torlon - 4301	1.4013	ϕ=12.7 mm; h=8 mm

Fig. 4.4 shows a typical thermal excitation and decay of heat pulse sensed by the platform thermometer. The measured thermal relaxation curves for all the samples showed a double exponential decay indicating a "lumped τ_2 effect" [125]. This can be either due to the poor thermal conductance be-

tween the sample and the platform, or due to the poor thermal conductance of the samples which is expected for non-metallic amorphous materials. The relaxation curve in such a system is given by

$$T = T_0 + A_1 e^{-t/\tau_1} + A_2 e^{-t/\tau_2} \tag{4.1}$$

where T_0 is the heat bath temperature, and

$$A_1 + A_2 = \Delta T = P/K \tag{4.2}$$

$$(A_1\tau_1 + A_2\tau_2)/(A_1 + A_2) = C/K \tag{4.3}$$

K being the thermal conductivity between substrate and the heat bath and C is the total heat capacity. The sample masses and the Teflon support links were chosen such that the total decay time constant for the relaxation curve was of the order of 5 - 20 secs.

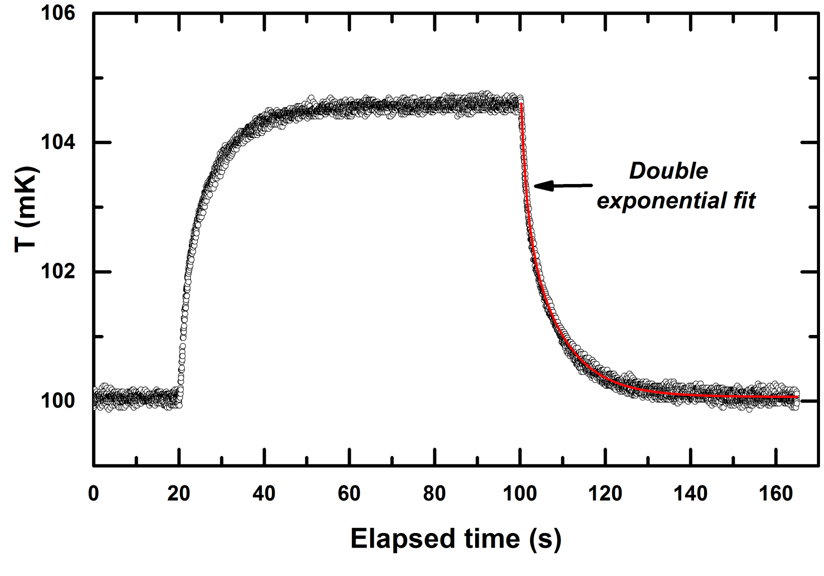

FIGURE 4.4: A typical temperature response of the Carbon sensor in response to a square wave current applied to the heat on the platform (see text for details).

The heat capacity data was fitted to equation 4.1 and the sample heat capacity was extracted following the analysis procedure suggested in Ref. [125]. The relaxation calorimetry measures the heat capacity of the sample together with the addenda. The specific heat of the samples were obtained by subtracting out the addenda contribution and normalizing it to the mass of the sample. The addenda contribution was measured in a separate run when no samples were present on the platform as shown in Fig. 4.5. All the samples were mounted using similar amount of GE-Varnish ensuring the addenda to be constant. The thermal conductivity of the heat link during all the heat capacity measurements is shown in Fig. 4.6. It can be seen the thermal conductivity remained unchanged as expected.

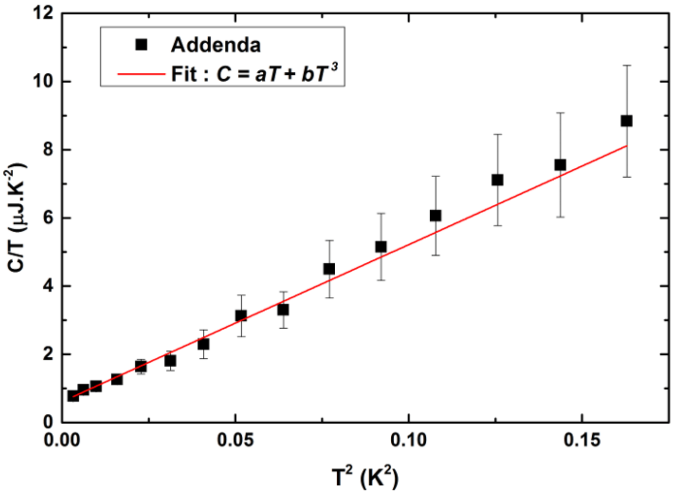

FIGURE 4.5: The measured specific heat of Teflon. The fitted result is in excellent agreement with the values reported by Boyer *et al.* [118] (see text for details).

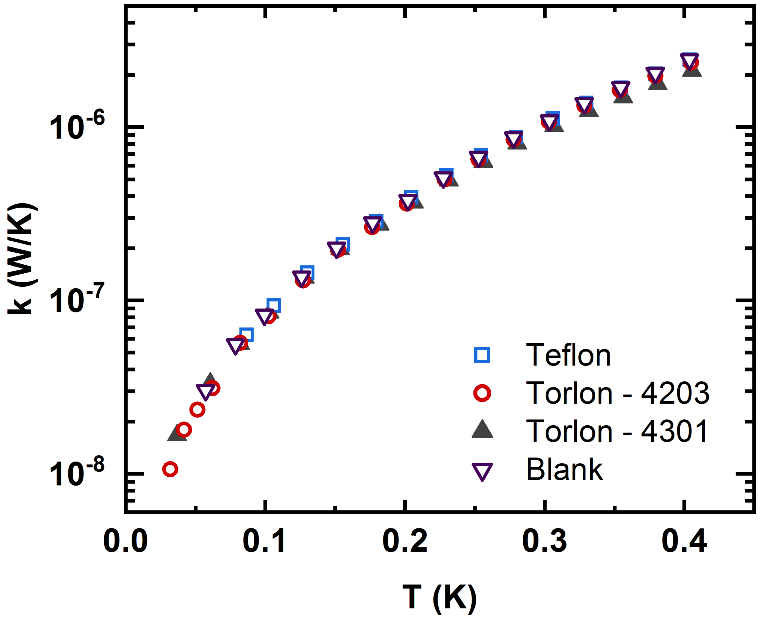

FIGURE 4.6: Thermal conductivity of the heat link in different runs.

4.3 Heat capacity of polymers

The low temperature specific heat of amorphous solids can be described by phenomenological model called the tunneling-state model [126, 127, 128]. The tunneling-state model predicts that specific heat of the amorphous material at low temperature can be described by an anomalous linear behavior with temperature, which is over and above the phonon contribution to the specific heat. This is in clear contrast to the T^3 dependence of specific heat predicted by Debye theory for crystalline solids. The linear term can be attributed to the tunneling transitions of small groups of atoms between two configurations of very similar energy. The experimental data (below 1 K) for various amorphous solids suggests that the specific heat of amorphous solids at very low temperatures can be described as

$$c(T) = a\,T^{(1+\delta)} \;+\; b\,T^3 \tag{4.4}$$

The value of δ ($0 \leq \delta \leq 0.5$) is dependent on the density of the states available for excitation and hence, can be strongly influenced by the structural disorder present in the amorphous solid.

The measured specific heat of Teflon is shown in Fig. 4.7 and can be represented by

$$c(T) = a\,T \;+\; b\,T^3 \tag{4.5}$$

$$\text{where} \begin{cases} a = (0.38 \pm 0.03)\ \mu J.K^{-2}g^{-1} \\ b = (34.7 \pm 1)\ \mu J.K^{-4}g^{-1} \end{cases} \tag{4.6}$$

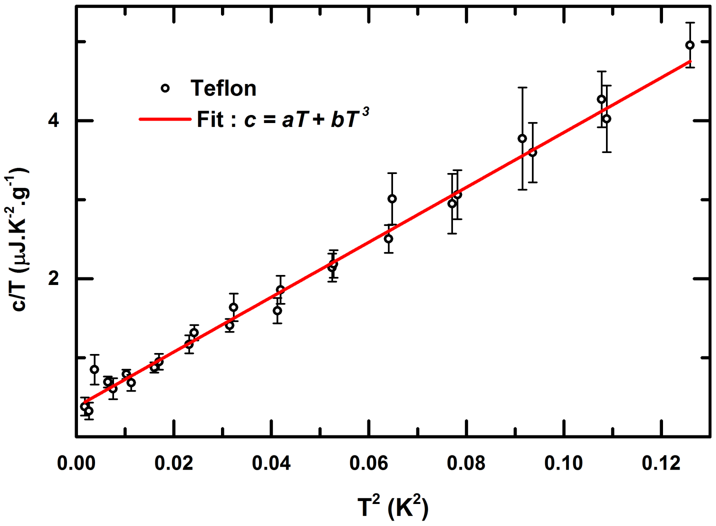

FIGURE 4.7: The measured specific heat of Teflon. The fitted result is in excellent agreement with the values reported by Boyer *et al.* [118] (see text for details).

This is in excellent agreement with the values reported by Boyer *et al.* [118] for Teflon (a = 0.36 $\mu J.K^{-2}g^{-1}$ and b = 34.9 $\mu J.K^{-4}g^{-1}$). The fact that the first term is purely linear (δ=0) indicates that the anomalies associated with structural disorder are nearly absent in the case of Teflon and the excitations would have a constant density of states in the energy range of interest. This can be expected since Teflon, available in high purity, is known to have a simple and well defined structure with a very high degree of polymerization.

The measured specific heats of Torlon - 4203 and Torlon - 4301 are shown in Fig. 4.8 and Fig. 4.9, respectively.

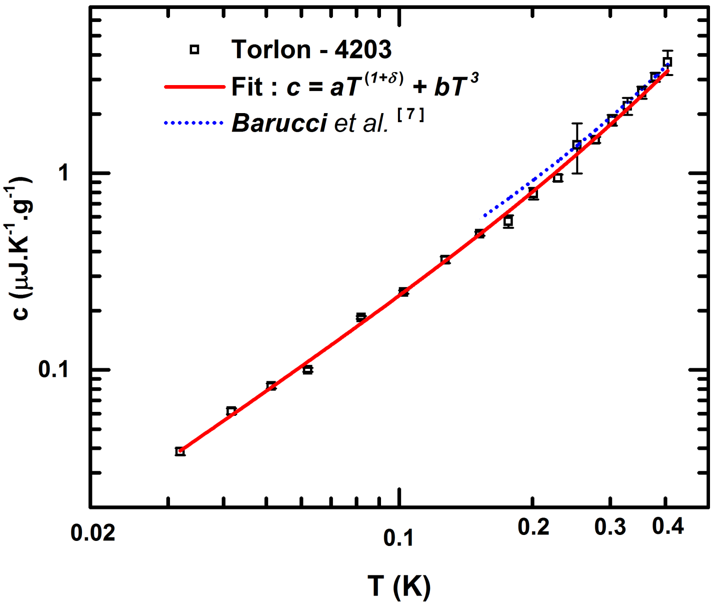

FIGURE 4.8: The measured specific heat of Torlon - 4203 (see text for details).

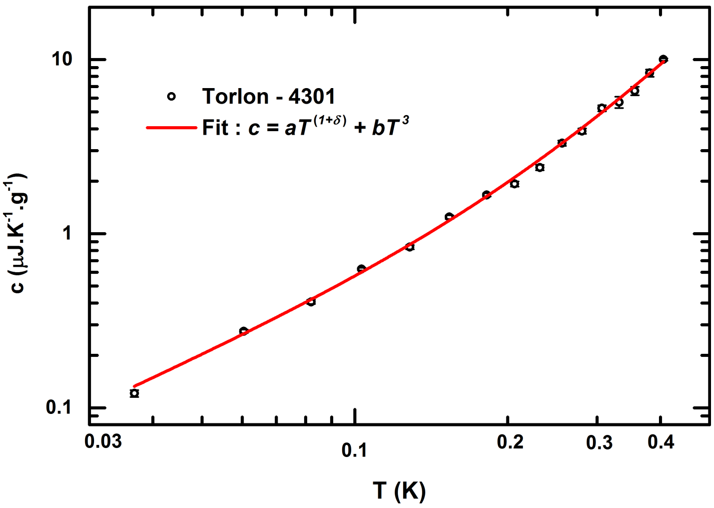

FIGURE 4.9: The measured specific heat of Torlon - 4301 (see text for details).

At low temperatures, the data for Torlon - 4203 and Torlon - 4301 deviates significantly from a straight line in a 'c/T' versus T^2 plot. A better fit to the data was obtained using Eq. 4.4. The structural disorder could be due to the presence of other elements present in the polyamide-imide resin. As mentioned before, Torlon - 4203 nominally contains 3% TiO_2 and 0.5% fluorocarbon and Torlon - 4301 contains 12% graphite powder and 3% fluorocarbon. The presence of these elements can significantly alter the density of states at very low temperatures. The extracted parameter values from the fits are given in Table 4.2.

Table 4.2: Extracted parameter values from the fit of Torlon - 4203 and Torlon - 4301 in the temperature range of 30 - 400 mK.

	a ($\mu J.K^{-(2+\delta)}g^{-1}$)	δ	b ($\mu J.K^{-4}g^{-1}$)
Torlon - 4203	7.2±1.3	0.52±0.06	23±6
Torlon - 4203† (Barucci *et al.* [119])	5.41±0.08	0.28±0.01	28.2±0.3
Torlon - 4301	9.4±1.6	0.30±0.07	102±8

† Data in the range of 0.15 - 1 K.

As evident from Fig. 4.8, the measured data agrees reasonably well with that reported by Barucci *et al.* [119] in the temperature range of 250 - 400 mK but deviates appreciably at lower temperatures. It should be noted that the value for δ obtained for Torlon - 4203 in the present work is significantly different from the value reported by Barucci *et al.*, which was extracted from measurements above 150 mK.

Fig. 4.10 shows the comparison of the specific heat of Teflon, Torlon - 4203 and Torlon - 4301 reported in this work.

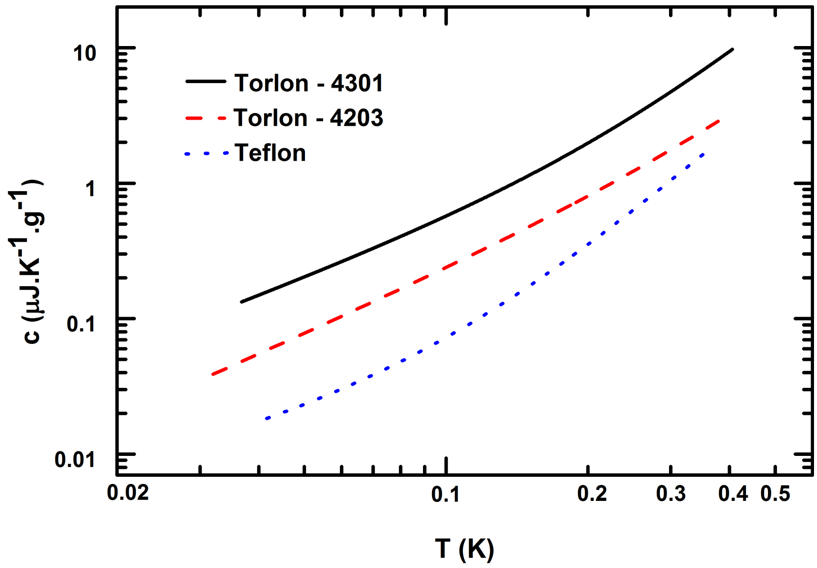

FIGURE 4.10: Comparison of the specific heat of Torlon - 4301, Torlon - 4203 and Teflon reported in this work.

The specific heat of Torlon - 4301 is significantly higher than Torlon - 4203, while Teflon has the lowest specific heat among all three owing to its very small coefficient for the linear term. Given its low specific heat, Teflon seems to be a better choice as a thermal link for low temperature detectors when minimization of heat capacity is a primary consideration. Torlon can be used for applications which require better strength for support structures and better thermal conductivity. In terms of specific heat, Torlon - 4203 is a better candidate for polymeric support structures in cryogenic applications than Torlon - 4301. Teflon is preferred for making support structure which acts as the weak heat link in cryogenic bolometer

4.4 Summary

Calorimetric measurements have been done to determine the specific heat of Torlon - 4301, Torlon - 4203 and Teflon in the range of 30 - 400 mK and has been analyzed in the framework of tunneling state model. The specific heat for Torlon - 4301 has been reported for the first time while the data for Torlon - 4203 and Teflon has been extended down to 30 mK. The data for Teflon is in excellent agreement with the values reported by Boyer *et al.* from 0.3 K to 20 K. The specific heat of Teflon is significantly smaller than Torlon - 4203 and Torlon - 4301 below 100 mK and hence, is more suitable for cryogenic applications which require low heat capacity materials. Torlon would be preferable for applications which require higher mechanical strength. Amongst Torlon, the specific heat of Torlon - 4203 (3% TiO_2 and 0.5% fluorocarbon) is appreciably lower than Torlon - 4301 (12% graphite powder and 3% fluorocarbon) over the entire temperature range investigated in this work.

Chapter 5

Tests with a sapphire bolometer

5.1 Introduction

As described in Chapter 1, the tin based cryogenic bolometer is being developed in India to study NDBD in ^{124}Sn [8]. An introduction to the cryogenic bolometer is given in Chapter 1. In order to understand various systematics affecting the bolometer performance, a sapphire bolometer is studied. The sapphire possesses very low specific heat (20 fJ/K/g at 10 mK), since Debye temperature is large (1042 K [129]) and has been tested at temperature as high as 1.5 K as a bolometer [22]. An understanding of the systematics is essential to study superconducting tin bolometer.

In this chapter, design of a sapphire bolometer test setup is described. A macroscopic thermal model based on Mathematica [21] to simulate thermal response of the bolometer is presented. An off-line pulse shape analysis technique developed for cryogenic bolometer is discussed. Studies on identifying various noise source and its influence on the sapphire bolometer in the CFDR1200 system at TIFR is discussed. Systematic studies on the response of the sapphire bolometer to the phonon pulses generated from a heater and alpha particles are presented.

5.2 Design of the bolometer

A picture along with a schematic view of the sapphire bolometer used for the present study is shown in Fig. 5.1. It consists of a 0.4 mm thick sapphire plate of area 20 mm × 20 mm which acts as the absorber. Two NTD Ge sensors and a heater element are strongly coupled to the sapphire bolometer with the help of a thin layer of low temperature araldite. The heater element is developed by evaporating a 200 nm thick Au meander on a Si substrate. The sapphire plate is connected to the gold plated Cu heat bath using tiny dots of araldite (Dia. ~ 1 mm, Thickness ~ 0.1mm), which provide a weak thermal link. The readout and the DAQ system is described in Chapter 2. The resistance of the heater element (R_H), as measured

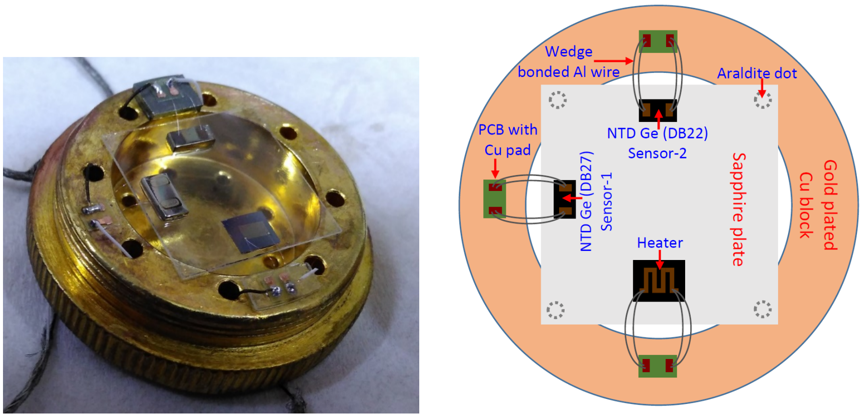

FIGURE 5.1: A picture of the sapphire bolometer setup (*left*) and a schematic view of the same (*right*).

using an AC resistance bridge AVS-47B, is found to be ~ 0.6 kΩ at 1 K and remains constant over the temperature range of 1 K down to 10 mK. Thus, R_H is substantially smaller as compared to the series resistor $\mathrm{R_{L2}}$ ($\mathrm{R_{L2}}/2 = 1\,\mathrm{M\Omega}$), making a constant current pulse of magnitude $\mathrm{I_H} \sim \frac{\mathrm{V_H}}{\mathrm{R_{L2}}}$. The NTD Ge sensor was optimally biased with a DC voltage of 400 mV from one of the DAC output. The other DAC output is used to power the heater in pulsed mode (200 μs wide square wave pulse @ 2 Hz). Both positive and negative heater pulses were used to avoid any error due to zero offset. The sensor output voltage is amplified with a gain of 60 dB using a commercially available differential voltage amplifier from FEMTO and the amplifier output is recorded using an ADC input channel with a sampling rate of 50 kS/s. The thermal response of this bolometer simulated with a macroscopic model is discussed in the following section.

5.3 Thermal modeling of the bolometer

To simulate the thermal response of a cryogenic bolometer a macroscopic model is formulated. This model is used to design various parts of a cryogenic bolometer e.g., the weak heat link, the sensor and the heater coupling etc. aiming to obtain an optimal response with reasonable fall time of the pulse. A schematic representation of a cryogenic bolometer is shown in Fig. 5.2. If power P_1, P_2 and P_3 are applied to the absorber, the sensor and the heater, respectively; then conservation of energy leads to the following matrix equation

$$\mathcal{C}\dot{\mathcal{T}} = -\mathcal{K}\mathcal{T} + \mathcal{P} \tag{5.1}$$

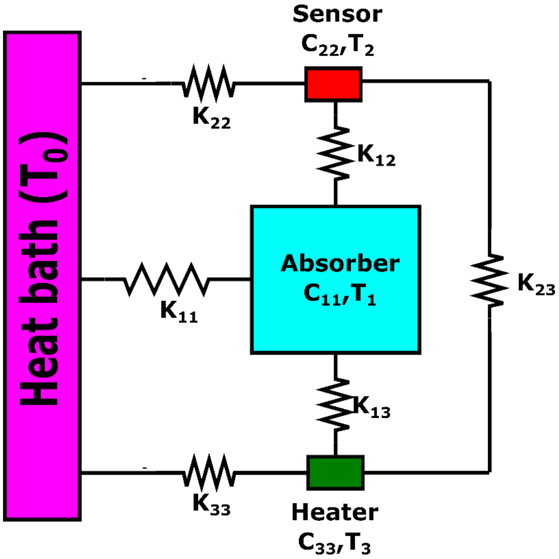

FIGURE 5.2: A schematic representation of a bolometer.

where

$$\mathcal{T} = \begin{pmatrix} T_1 & T_2 & T_3 \end{pmatrix}, \mathcal{C} = diag \begin{pmatrix} C_{11} & C_{22} & C_{33} \end{pmatrix}, \mathcal{P} = \begin{pmatrix} P_1 & P_2 & P_3 \end{pmatrix}$$

and

$$\mathcal{K} = \begin{pmatrix} K_{11} + K_{22} + K_{22} & -K_{12} & -K_{13} \\ -K_{12} & K_{22} + K_{12} + K_{23} & -K_{23} \\ -K_{13} & -K_{23} & K_{33} + K_{13} + K_{23} \end{pmatrix}$$

.

The C_{ii} and K_{ij} are the heat capacity and thermal conductivity, respectively, of different elements as indicated in the Fig. 5.2, and T_i are the corresponding temperatures. The temperature variation of various elements upon energy deposition is obtained by solving the equation 5.1 numerically in Mathematica [21] with the following assumptions:

a) Energy is transferred to the phonons in a time scale which is negligible to the pulse evolution i.e., phonons are thermalized.

b) At every instant the thermal distribution of each component of the system is in thermal equilibrium.

c) Heat capacities and thermal conductance's independent of temperature during pulse evolution.

Various parameters of the bolometer as listed in the Table. 5.1 are used as an input for the numerical calculations.

TABLE 5.1: Parameters of the bolometer setup used as inputs to the thermal model.

Parameter	Material	Dimension	Value at T K	Value 10 mK
C_{11}	Sapphire	20×20×0.4	$1.1 \times 10^{-8}T^3$	11 fJ/K
C_{22}	NTD Ge	3×6×1	$9.9 \times 10^{-9}T$	396 pJ/K
C_{33}	Au meander on Si	4×6×1	$1 \times 10^{-10}T$	11 fJ/K
K_{11}	4 araldite spots	$\phi = 1, h = 0.05$	$1 \times 10^{-3}T^3$	1 nW/K
K_{22}, K_{33}	Al wires	20μm dia	-	40 pW/K
K_{12}, K_{13}	Thin layer of araldite	3×6×0.05	$36 \times 10^{-3}T^{2.65}$	180 nW/K

A smoothly varying and trivially integrable function as given in equation 5.2 was used to generate the heat pulse.

$$P_1(t) = \begin{cases} \frac{Q}{2\,t_p}(1 \; + \; cos\;[\pi(t - t_0)/t_p]) & \text{for } (t_0 - t_p) < t < (t_0 + t_p), \\ 0 & \text{otherwise} \end{cases} \tag{5.2}$$

here, 2 t_p is the width of the heat pulse and Q is the total deposited energy given by

$$Q = \int_{t_0-t_p}^{t_0+t_p} P_1(t)dt \tag{5.3}$$

A heat pulse of width 2 ms having energy of 5 MeV generated using equation. 5.2 is shown in Fig. 5.3 *(left)* . The calculated temperature of the absorber, the sensor and heater when this heater pulse is applied on the absorber at a base temperature of 10 mK is shown in Fig. 5.3 *(right)*. Since $K_{12} >> K_{11}$ and $K_{13} >> K_{11}$ the temperature of the sensor and the heater follows the temperature of the absorber, as expected. The decay time for the simulated pulse is ~0.4 s which is desirable for the current DAQ system having low sampling rate as described in the Chapter 2. This is also acceptable for rare event studies in a low background setup (< 0.01 counts keV^{-1}kg^{-1}year^{-1}) as the pileup is not a concern. The experimentally obtained sensor output for a heater pulse of equivalent energy 5 MeV is shown in Fig. 5.4 As it can be seen that the decay constant for the

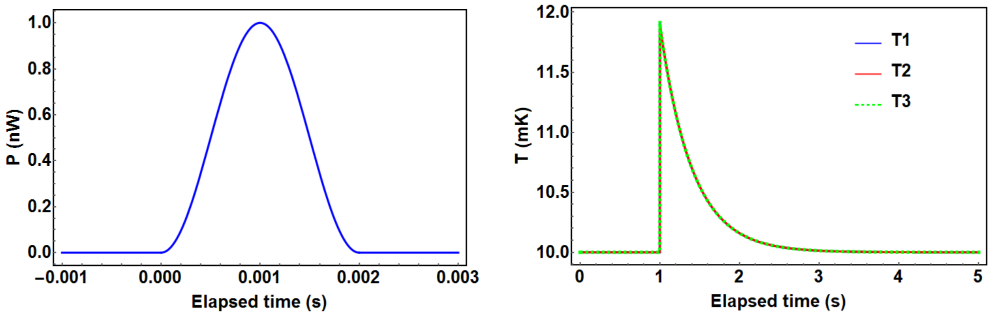

FIGURE 5.3: The input heater pulse of energy 5 MeV *(left)* and the corresponding calculated thermal response *(right)*.

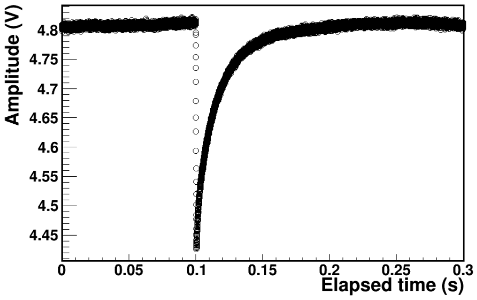

FIGURE 5.4: Experimentally obtained signal for a 5 MeV heater pulse at a base temperature of 10 mK.

experimentally obtained pulse (~13 ms) is significantly less as compared to the calculated thermal response. The reason for this discrepancy could not be ascertained, however this decay time was sufficiently large for further measurements .

5.4 Pulse height analysis program for the bolometer

Unlike other particle detectors e.g. Scintillator detector, HPGe detector etc., the response time of a bolometric detector is comparatively slow. The rise time of a large mass (~100 g) bolometer is ~10 ms and decay time is ~ 0.1 s – 1 s. Commercially available hardware modules with on-line pulse shape analysis are suitable for detectors with fast rise time and fall time (ps to ns). Hence, a pulse analysis program is needed to extract the best possible energy resolution of the bolometer detector. Moreover, if the pulse characteristics varies with temperature which can be easily taken care in an off-line pulse analysis program.

A ROOT based C++ program is developed for off-line pulse shape analysis of the bolometer signal. The program consists of two parts. In the first part, smoothened signal (S0), first derivative (S1) and second derivative (S2) of the digitally sampled raw pulse (S) are derived by applying Savitzky-Golay technique [24] as illustrated in Fig. 5.5 (left). In the second part, when S1 crosses a certain preset threshold, various pulse shape parameters as listed in Table. 5.2, are extracted. The time t_0 defines the arrival time of the

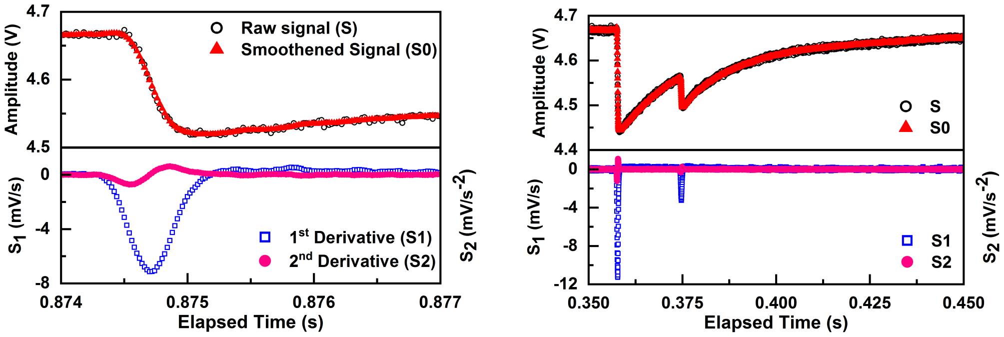

FIGURE 5.5: An example of the pulse processing (left) and pileup pulses (right).

pulse and t_r is a measure of the rise time, t_p and t_d are the peaking time and decay time of the pulse, respectively. P_R, P_H and P_A are related to the pulse height. The timing parameters are used to filter out spurious pulses. The pileup pulses are well separated in S1 yielding efficient pileup rejection (see Fig. 5.5 (right)). The sensor output for input heater pulses of equivalent energy of 0.3 - 5 MeV is shown in Fig. 5.6 and the pulse height (P_A) as a function of heater energy is shown in Fig. 5.7. Though the pulse height (P_A) increases linearly with heater energy at low energy (< 3 MeV), a deviation is observed at higher energy (10 MeV). Hence, the

TABLE 5.2: Pulse shape parameters

Parameter	Definition
t_0	Time when S1 crosses the threshold
t_1	Time when S1 is maximum & S2≥0
t_2	Time when S0 is maximum & S1≥0
t_3	S0 decays 63 % from the maximum
t_r	t_1 - t_0
t_p	t_2 - t_0
t_d	t_3 - t_2
P_R	Height of S0 pulse
P_H	Height of S1 pulse
P_A	Area under S1 pulse

detector is calibrated by fitting the heater energy vs P_A plot using the 2nd order polynomial as

$$E = a_1 P_A + a_2 P_A^2 \tag{5.4}$$

here a_1 and a_2 are constants. It should be mentioned that P_R is extracted

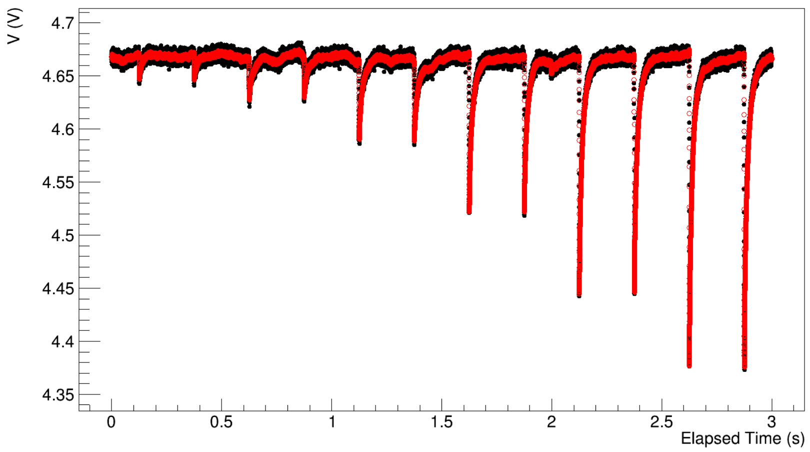

FIGURE 5.6: The sensor output for heater pulses of equivalent energy of 0.3 - 5 MeV at 20 mK.

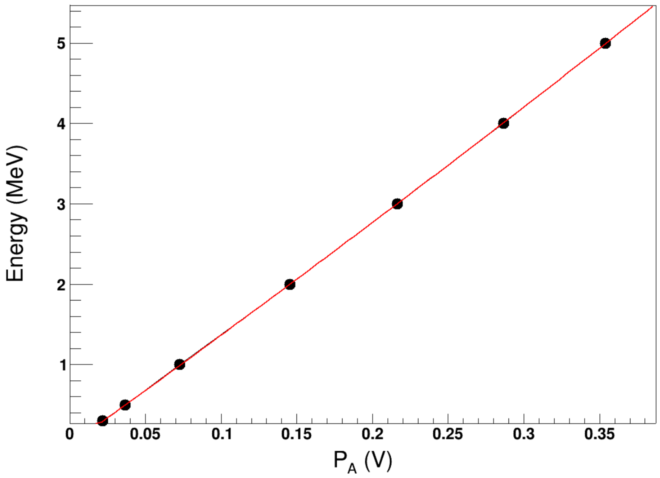

FIGURE 5.7: The pulse height (P_A) as a function of heater energy along with the fit to equation 5.4 at 20 mK.

from the S_0 signal and gets most affected due to baseline noise and results in poorer resolution than P_H or P_A as expected. Since, P_A takes into account the variation in the rise time it results in better resolution than obtained from P_H or P_R as shown in Fig. 5.8. Since, the bolometer

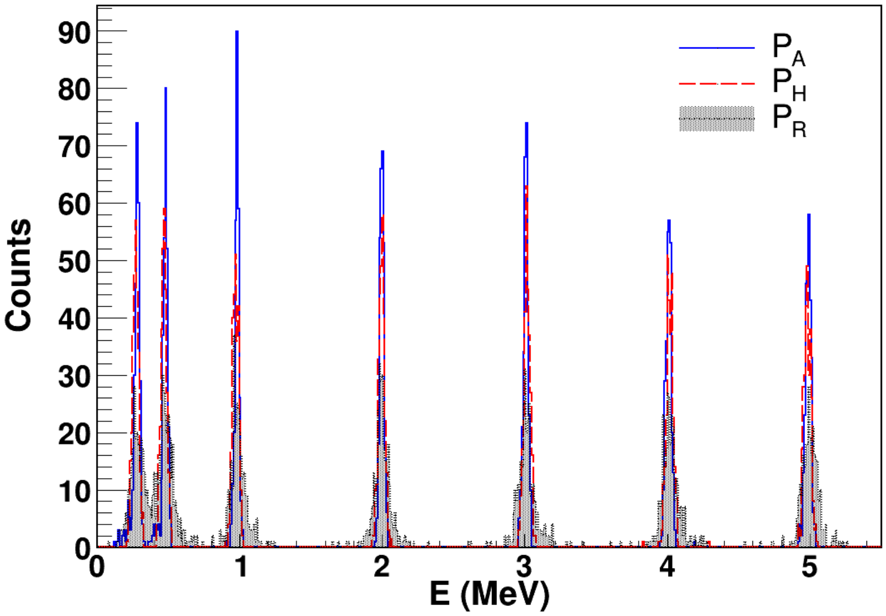

Figure 5.8: The energy spectrum for thermal pulses comparing P_R, P_H and P_A.

signal is strongly dependent on the base temperature, any variation in the baseline would deteriorate the energy resolution. In most of the cases the baseline variation arises due to microphonics which deposits energy in the absorber. Due to this the average temperature of the bolometer increases and the pulse height decreases resulting a tail in the lower energy as shown in Fig. 5.10 (solid blue line). As an example 10 pulses contributing to the low energy tail and the peak of the energy histogram (shown in solid blue line in Fig. 5.10) is displayed in black and red, respectively in Fig. 5.9 (left). Sample points from the baseline of 0-99 ms is taken from from the baseline and the mean vs sigma is plotted in a 2D histogram (see Fig. 5.9 (right)). A suitable rectangular gate is applied to reject the noisy events as result the resolution is improved and is shown in Fig. 5.10.

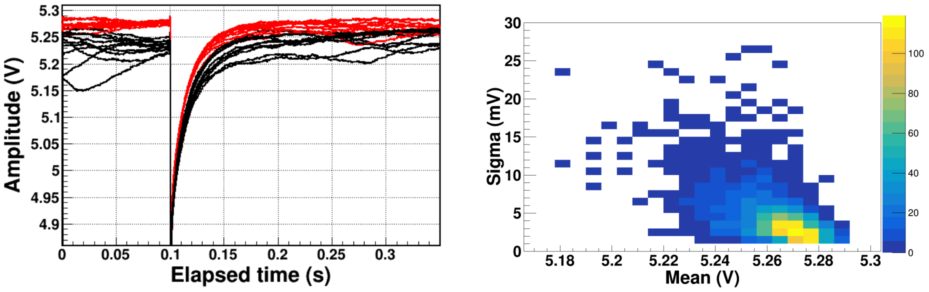

FIGURE 5.9: a) An example of pulses with noise baseline (black) and stable baseline (red). b) The mean vs sigma distribution of the baseline of 0-99 ms.

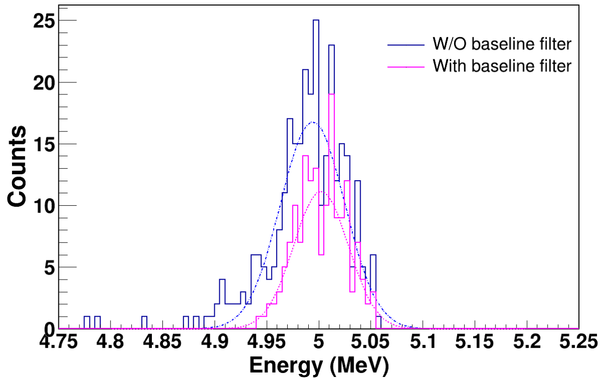

FIGURE 5.10: Comparison between energy spectrum obtained with or without baseline filter for a heater pulse of energy 5 MeV.

5.5 Effect of external noise

The resolution achieved with cryogenic bolometers is often not limited by the intrinsic resolution of the bolometer, but by the external noise sources in the system. The intrinsic resolution of the bolometer depends only on the bolometer temperature and the heat capacity, and is extremely small as compared to the contribution due to external factors [130]. For example, the intrinsic resolution (σ_E) of a TeO_2 bolometer ($5\times5\times5 cm^3$) is expected to be $\sim$ 10 eV at 10 mK, while experimentally the best resolution achieved is $\sim$ 2.13 keV (FWHM $\sim$ 5 keV) [131]. In the case of microbolometer ($< 10\mu$g), resolution $\sim$ few eV has been reported [132]. Therefore, a major challenge for these experiments is to minimize the contribution of external noise originating from the cryogenic system and the associated electronics. Noise induced due to the mechanical vibrations is one of the major drawbacks in a pulse tube based cryogenic system. The effect of mechanical vibrations can propagate to the lowest temperature stage and result in heating of the sensor, thereby affecting the performance of the bolometer. In addition to acting as an additional thermal load, these vibrations can also couple to the signal lines causing microphonic noise pickup in the readout signal. Hence, some attempts to reduce the contribution of pulse tube induced vibrational noise by implementing special vibrational damping measures during the design of the cryostat have been reported [95, 93, 133]. Other major contribution in the external noise sources involves the intrinsic noise of the mK thermometer and that induced by the front-end electronics. Apart from these widely known external factors, there can be system specific noise sources like vacuum pumps and measurement units. An efficient and proper ground connection of the system is necessary in order to minimize the ground loops, which otherwise can result in noise pickups in the operating frequency range. These various sources of pickups can have a detrimental effect on the overall performance of the bolometer and therefore, it is essential to investigate and eliminate the same. With this motivation, we have studied the noise and its influence on a test bolometer in the cryogen free dilution refrigerator (CFDR-1200) system at TIFR [14]. The detailed noise measurements in the frequency span of DC – 25 kHz have been carried out for the entire setup including the system related diagnostics, control systems, NI- based data acquisition (DAQ) system and the readout electronics. An efficient grounding configuration is implemented to minimize the ground loops in the system. Several measures are taken to minimize or eliminate unwanted pickups originating from various control and diagnostic modules of the cryogenic system, mainly the vacuum pumps and vacuum gauges. Consequently, an improvement in the minimum achievable base temperature and in the temperature of NTD sensor have been observed. The resolution of the bolometer is also evaluated at 15 mK by applying external heater pulses. Significant improvement has been observed in the resolution of the bolometer. Details of various noise sources, measured noise levels over a wide frequency range and corrective measures implemented to improve the performance of a cryogenic bolometer is discussed in this section.

5.5.1 Effect of external noise on the bolometer

In the present experiment, only Sensor-1 (DB27) is used for assessing the performance of the bolometer. The resistance (R_S) for the DB27 has been measured as a function of mixing chamber temperature (T_{MC}) in the range of 10–400 mK. It was observed that the measured resistance of DB27 showed a deviation from the Mott behaviour below 50 mK and saturated at $\sim$ 250 MΩ, even though the mixing chamber cools down to 10 mK. Since the sensor is coupled to the heat bath via a weak heat link, heat load from the external factors such as various noise pickups and the pulse tube induced mechanical vibrations, can affect the sensor cool down. To understand the impact of external noise on sensor temperature and bolometer performance, noise spectra have been recorded using NI based DAQ system and FFT analysis was done to understand different noise sources. All noise measurements are done at the MC temperature (T_{MC}) of 10 mK and the voltage gain of the amplifier is fixed at 80 dB. As mentioned earlier, one of the major factors limiting the bolometer performance can be inefficient ground connections involving several ground loops. A schematic block diagram showing the optimized grounding scheme of different modules of the setup is shown in Fig. 5.11. Along with the CFDR cryostat, the NTD sensor readout system consisting of differential amplifier and DAQ signal box, the AVS preamplifier for diagnostic thermometry of different stages of the cryostat and the AVS preamplifier for the NTD sensor readout at 300 K are enclosed within a Faraday Cage. The CFDR controls for ^{3}He-^{4}He gas handling system (GHS) and accessories are routed through an optically isolated USB – RS232 interface. The other modules such as PXI chassis, AVS resistance bridges and PCs for acquisition and control are fitted in an anodized metallic rack (outside the Faraday cage). The PXI is connected to the PC with an optical link to reduce external EMI pickups. For minimizing the ground loops, a specially designated clean earth pit is set up in the laboratory and ground connections are fanned out from this hub to

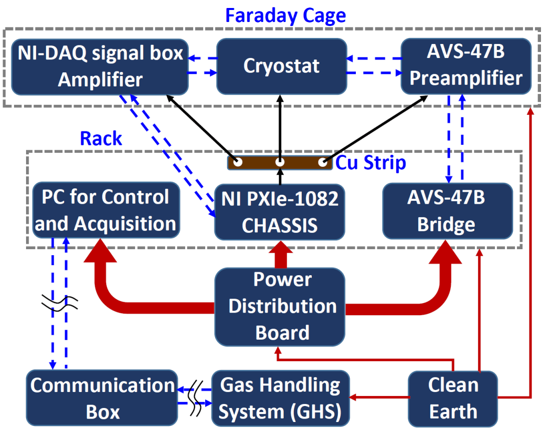

FIGURE 5.11: Schematic representation of optimized grounding scheme for the measurement setup in CFDR-1200. Thick red lines- ground connections through power distribution board; thin red lines- ground connections taken directly from the clean earth pit; thin black lines- ground connections taken from the NI PXI Chassis; blue dashed lines- communication link between different modules; blue dashed lines with break- optically isolated communication link; Communication between GHS and cryostat is not shown in the figure.

various units as shown in Fig. 5.11. The power line ground for different PCs for control and acquisition, PXI chassis and AVS resistance bridge is also derived from the clean earth pit. The PXI chassis acts as a master ground for the DAQ signal box, the differential amplifier, the AVS preamplifier box as well as the cryostat. The instrument rack, which is directly grounded, is also kept isolated from the body of the different extension boards used for power connections to various instruments. Fig. 5.12 shows the noise spectra in the frequency range of 0 to 500 Hz for an optimal and a sub-optimal ground configuration. As an example of a ground loop in the sub-optimal grounding, the master ground is assigned to the cryostat body, which results in multiple ground connections for DAQ – through the cryostat body as well as through the power connection. In this configuration, the peak at 50 Hz with a magnitude of -50 dB is clearly visible.

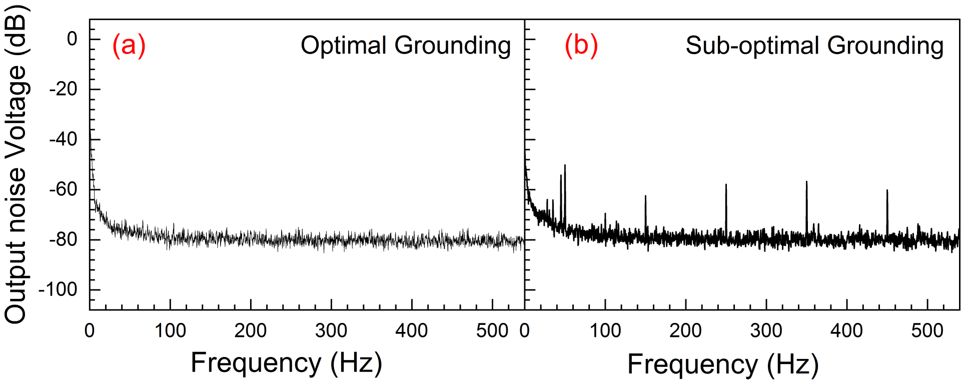

FIGURE 5.12: FFT spectra of the output of the amplifier for DB27 showing the effect of ground loops on 50 Hz noise. Measurements are done with a voltage amplifier gain of 80 dB, $T_M C$ = 15 mK, I_{Still} = 20 mA and pulse tube operating in a linear drive mode.

Higher order harmonics of 50 Hz are also visible in the sub-optimal ground configuration. In the optimized configuration, the 50 Hz noise component is below the sensitivity of the measurement, namely, -76 dB. It is observed that the T_{MC} could not be stabilized at 10 mK in the sub-optimal ground configuration. Therefore, T_{MC} is stabilized at a higher temperature of 15 mK with still current (I_{Still}) of 20 mA. It should be pointed out that both the sensor resistance and the resolution of the bolometer are very sensitive to the ground configuration. Further noise measurements have been carried out with optimal grounding at T_{MC} = 10 mK for four configurations: Case-I: pulse tube operating with a normal drive, motor head mounted on the cryostat Case-II: pulse tube operating with a linear drive, motor head detached from the cryostat Case-III: pulse tube operating with the linear drive, motor head detached from the cryostat, electronics of IVC (Inner Vacuum Chamber) vacuum gauge disconnected Case-IV: pulse tube operating with the linear drive, motor head detached from the cryostat, electronics of all vacuum gauges disconnected. Noise spectra for the above four configurations are measured with a fixed voltage gain of 80 dB and are shown in Figures 5.13 to 5.16. The FFT spectra are taken over a wide frequency range of 0 – 25 kHz and are divided into four blocks with the frequency range of 20 Hz, 500 Hz, 2 kHz and 25 kHz. Initially, the noise spectra for DB27 are recorded with the pulse tube in normal drive mode to assess the impact of the pulse tube motor vibration. In Fig. 5.13, noise peaks at 9.75 Hz, 11.25 Hz and a broad peak at 140 Hz are mainly contributed by the harmonics of 1.4 Hz, pulse tube induced noise. Pickups at frequency 827 Hz and 985.5 Hz are contributed by vacuum pumps of the CFDR. There are several peaks in the 25 kHz window, with a dominant pair of peaks around 16 kHz with an output voltage of -55 dB. This pickup

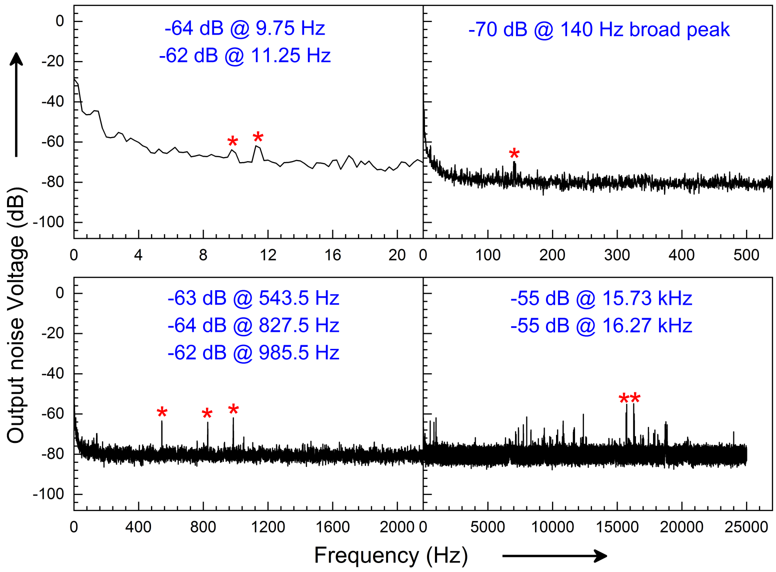

FIGURE 5.13: FFT spectra of the amplifier output for DB27 sensor for Case I (See text for details).

around 16 kHz is found to originate from the vacuum gauges in the CFDR system. It was noticed that this noise at 16 kHz is also sensitive to the ground loop and found to increase to -32 dB in the sub-optimal ground configuration compared to -55 dB in the optimal grounding. As mentioned earlier, the linear drive mode for the pulse tube operation is preferable at low temperature for reducing the vibrational noise. Additionally, the pulse tube motor head is isolated from the cryostat for further reduction in vibration. In the noise spectra for Case II (Fig. 5.14) reduction in noise peaks at 9.75 Hz, 11.25 Hz and 140 Hz is evident. Thus operating the pulse tube in linear drive helps in cooling the DB27 sensor, which is also reflected in the higher saturation value of the resistance of 370 MΩ as compared to 250 MΩ for Case I.Fig. 5.15, corresponding to the Case III, shows that the noise peak at 16 kHz almost vanishes after disconnecting the IVC gauge electronics and the measured resistance of the sensor was 440 MΩ.

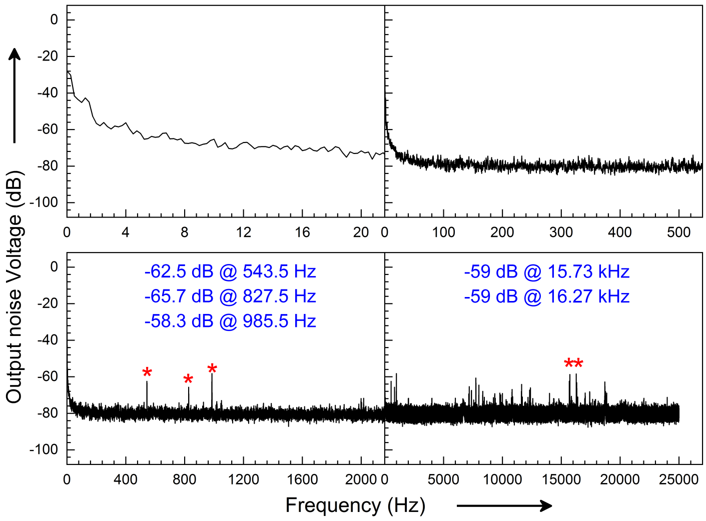

FIGURE 5.14: FFT spectra of the amplifier output for DB27 sensor for Case II (See text for details).

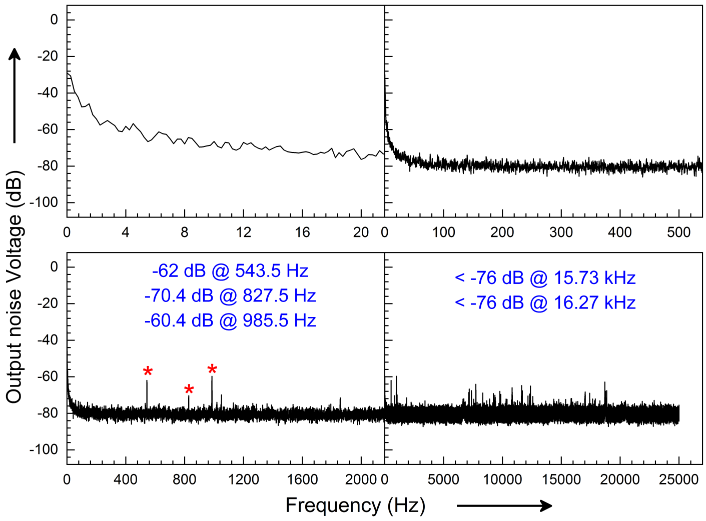

FIGURE 5.15: FFT spectra of the amplifier output for DB27 sensor for Case III (See text for details).

The heat load in the system is further reduced after disconnecting all other vacuum gauge electronics (Outer Vacuum Chamber, Probe and Still) of the CFDR system. The FFT spectra of the amplifier output corresponding to Case IV is shown in Fig. 5.16. No significant changes are observed in the FFT spectra of Case III and Case IV, but its effect is seen on the cooling of the sensor. The resistance of the sensor now saturates at 594 MΩ as compared to 440 MΩ in Case III. Details of the various frequency components of the noise pickups at different stages of system improvements (Cases I to IV) are summarised in Table I. Except for the Case I, where the pulse tube is operating in normal drive mode, the pulse tube noise is not visible in the FFT spectra.

The noise spectrum continues to show several frequency peaks, albeit small. The residual noise is seen to be generated by the pulse tube system,

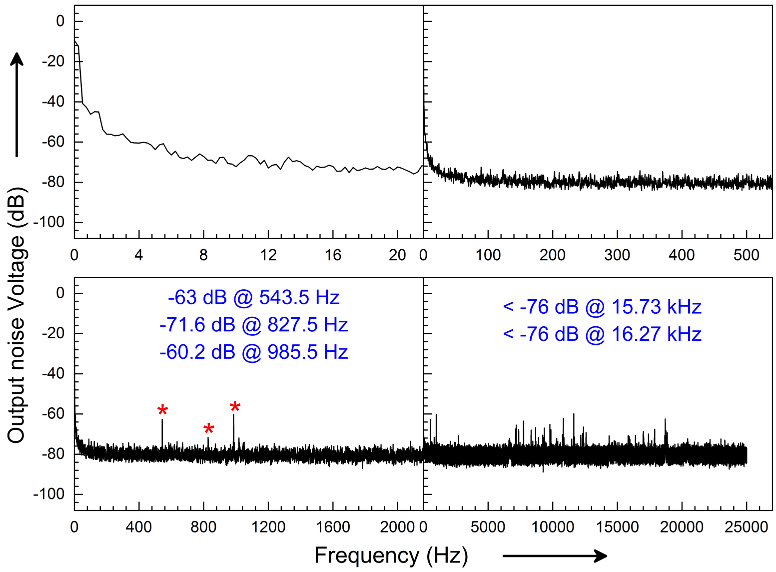

Figure 5.16: FFT spectra of the amplifier output for DB27 sensor for Case IV (See text for details).

which is verified by momentarily shutting off the pulse tube cryocooler. The measured resistances in the temperature range of 10 – 400 mK for the above mentioned cases are shown in Fig. 5.17, where the effect of eliminating different noise sources is evident. It can be seen from the figure that the DB27 sensor resistance has increased substantially in case IV as compared to that obtained in Case I. However, it still shows a deviation from the standard Mott curve, but the temperature at which deviation occurs is lower indicating a net improvement in the cooling of sensor. The effect of ground loops was also reflected in the minimum temperature achieved at MC and in the measured resolution of the bolometer. In the best configuration (Case-IV), the lowest temperature of ~ 5 mK (as measured with CMN) could be achieved as compared to 6.7 mK in the sub-optimal ground configuration.

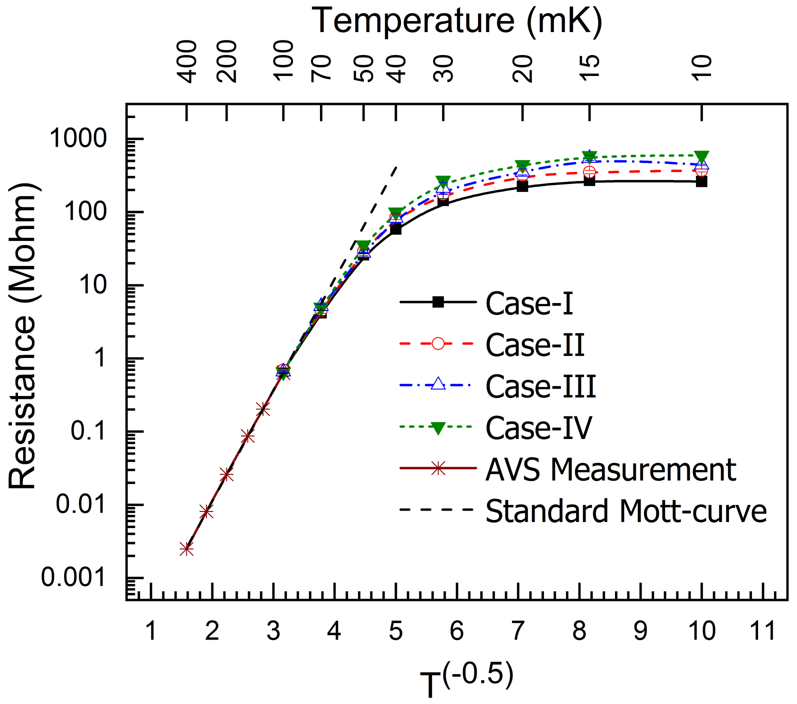

FIGURE 5.17: Measured resistance of the NTD Ge sensor DB27 for Case-I to Case-IV in the temperature range of 10 – 400 mK. The fit to data in 100 – 400 mK range with the standard Mott curve (R 0 = 10.2 (0.5) Ω and T 0 = 12.2 (0.2) K) is also shown for comparison.

A comparison of bolometer resolution for the case-IV configuration with sub-optimal and optimal grounding is shown in Fig. 5.18. It is observed that resolution of the bolometer worsens by ∼ 80% (from 15 keV to 27 keV) in case of a sub-optimal ground configuration. The resolution of the bolometer is found to improves by ∼ 30% when the pulse tube is switched from the normal drive (Case-I) to the linear drive (Case-II). However, different configurations with the pulse tube in linear drive mode (i.e. Case-II to Case-IV) yield similar results within measurement errors (∼ 15 keV) for the bolometer resolution.

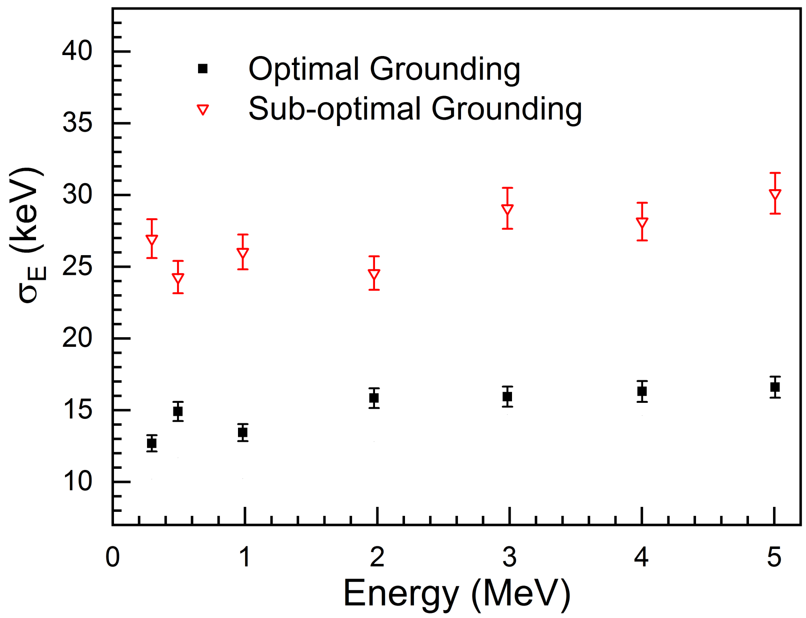

FIGURE 5.18: Measured resolution of the sapphire bolometer in the energy range of 300 keV to 5 MeV, at 15 mK.

5.6 Response to phonon pulses

As mentioned earlier, in order to understand various systematics affecting the bolometer performance, the response of the sapphire bolometer in the temperature range of 10-100 mK is measured with phonon pulses generated by a heater. An understanding of the systematics will be useful to study superconducting tin bolometer. Energy resolution (σ) of the sapphire bolometer is measured with heater pulses of equivalent energy of 0.3-10 MeV in the temperature range 10 -100 mK. At each temperature pulse height vs bias current measurement was done and an optimum bias current (20 nA-1 μA) was chosen for the energy calibration measurement. The rise time and the decay time of the bolometer signal at 10 mK are ~1 ms and ~ 15 ms, respectively.

- Though the energy calibration is linear at low energy (< 3 MeV), a deviation of ~8 % is observed at higher energy (10 MeV).
- It is found that energy resolution (σ_0) decreases as function of the MC temperature. However, in the range of 10-25 mK the energy resolution is found to be nearly independent of the temperature.

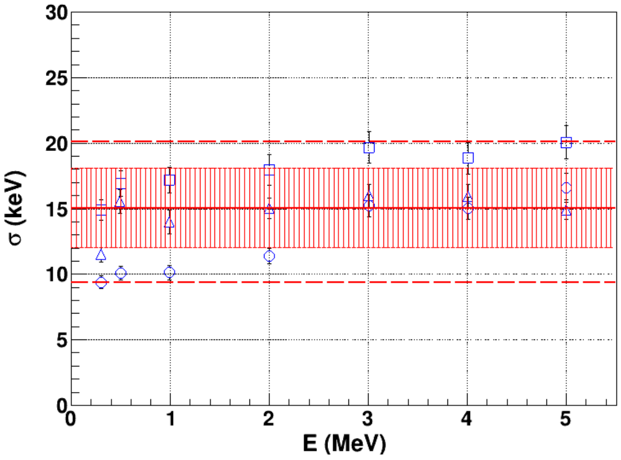

FIGURE 5.19: Energy resolution of the sapphire bolometer at 15 mK with phonon pulses in three different sets of measurements

- The energy resolution in this temperature range was repeated over three different thermal cycles. A good reproducibility is observed and data are shown in Fig. 5.19.
- It can be seen that the energy resolution of the bolometer(σ_0) is nearly constant ~ 15 ± 3 keV over the energy range of 0.3-5 MeV.
- Measurements were also performed with heater energy ranging upto 10 MeV where a non linear dependence of resolution (σ_0 at 10 MeV = 30 keV ± 2 keV) with energy could be seen for energies E>3MeV.

- A moderate size tin sample of mass 0.6 g was mounted on the sapphire substrate using N-Grease and the energy resolution (σ_{Sn}) in the temperature range of 15 - 25 mK is compared with that for the blank sapphire. No significant difference could be noted on the decay time and the linearity of the energy calibration. It is observed that for E<3 MeV, the σ_{Sn} is comparable to σ_0 but at higher energies σ_{Sn} increases with E. This is surprising as thermal noise is temperature dependent and not energy dependent. Also, most of other external noise factors are expected to be independent of energy.

5.7 Response to alpha pulses

For tests with alpha particles, a weak ^{239}Pu-^{241}Am alpha source (~ 10 dps) electroplated on a SS disk is mounted with a brass collimator (1 mm dia). The mounting setup is shown in Fig. 5.20. Expected energies form the two major peaks are 5.156 MeV and 5.485 MeV [26]. The energy spectrum of

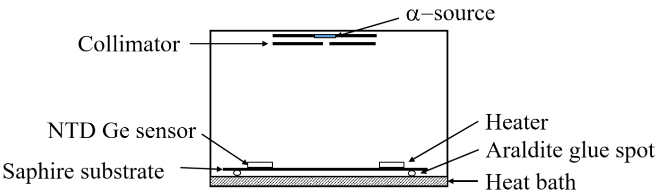

FIGURE 5.20: A schematic of the sapphire bolometer setup with the alpha source

the source with the collimator was recorded using a silicon surface barrier detector for reference. The alpha pulses were acquired for a duration of ~ 6-10 hours at different MC temperatures of 15 mK, 20 mK and 25 mK. A LabView program was used to record the amplified voltage signal in leading edge trigger mode with a sampling rate of 50 kHz. The acquired data was analyzed using the analysis technique as described earlier and the spectrum is shown in Fig. 5.21. Although two peaks are visible, they are not very well separated. The peak at low energy (pulse height ~ 0.035 V) can arise due to energy deposition of cosmic muons. It is puzzling to note that E_α estimated from the heater calibration, namely, 3.3 MeV and 3.6 MeV, are significantly lower than the actual source energies (5.156 MeV and 5.485 MeV, respectively). Discrepancy in the heater calibration and radiation energy was earlier reported in Ref [27], but has not been understood. The resolution $\sigma \sim$ 70-180 keV estimated from the energy difference in peaks Δ E = 330 keV and is considerably worse than the σ_0. It should be mentioned that baseline/peak drifts over larger acquisition period could contribute to worsening of the resolution. Further investigation with γ sources and/or muons will be required.

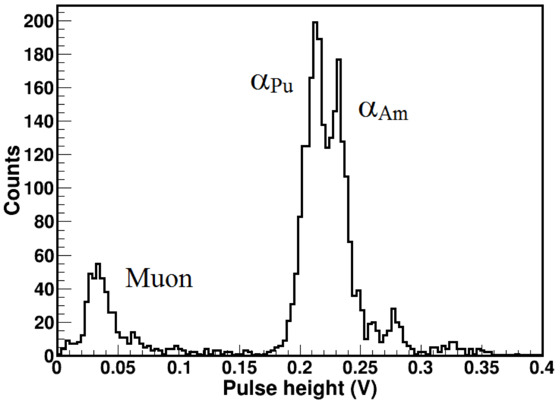

FIGURE 5.21: Pulse height spectrum obtained with the alpha source

5.8 Tests with a conventional wet dilution refrigerator

In order to study the impact of vibration on the performance, the bolometer is also tested in a Leiden Cryogenics make conventional wet dilution refrigerator (DRS 1000) at TIFR [25], where the vibrational noise is expected to be less as compared to the CFDR1200. The lnR vs $T^{-1/2}$ graph along with the fit to Eq.3.1 for the DB27 sensor at DRS 1000 is shown in Fig. 5.22. The value of T_0 (15.4±1.2) is consistent with that obtained at CFDR1200 within error. However, a discrepancy in the absolute value of the resistance at a particular temperature is observed the reason to which could not be identified. It should be noted that the maximum resistance obtained at DRS 1000 is $\sim$ 16 GΩ at a mixing chamber temperature of 11 mK which translates to a sapphire temperature of ~30 mK. In contrary, the maximum resistance obtained at CFDR1200 is 600 MΩ at 10 mK mixing

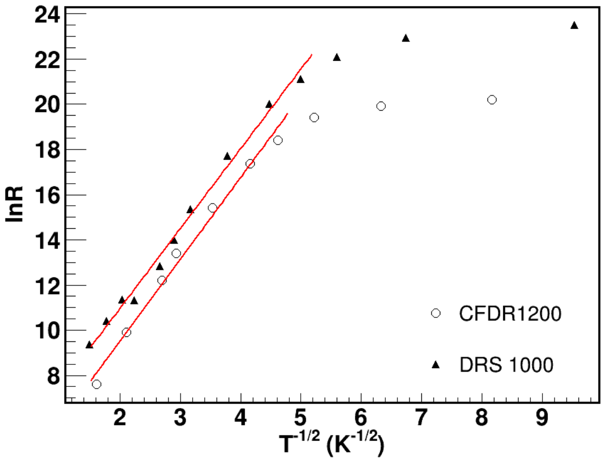

FIGURE 5.22: lnR vs $T^{-1/2}$ graph along with the fit to Eq.xx for the DB27 sensor at DRS 1000.

chamber temperature which indicates to a sapphire temperature of ~40 mK. This implies that an improvement of ~10 mK is observed in DRS 1000 in terms of cooling. The noise V_{rms} is related to sqrt R. The noise spectrum obtained at 50 mK at DRS 1000 and ~10 mK at CFDR is compared where the resistance values are similar and is shown in Fig. 5.23. There is no prominent peak above the background could be seen in the frequency range of DC-20 Hz. The rms noise is ~2.5 times less in the DRS 1000 as compared to CFDR1200 in the frequency range of 1-5 Hz. The bolometer is studied with heater pulse as explained in the earlier section. The best achieved energy resolution of the bolometer in the wet dilution refrigerator is about a factor of 2 better as compared to that obtained in the CFDR1200. The energy spectrum obtained with the same ^{239}Pu-^{241}Am alpha source is shown in Fig. 5.24 Using the energy calibration obtained from the heater pulses the alpha peak corresponds 5.4 MeV with a resolution of 130 keV. The absence of one of the two peak could be due to shift in the alignment of the collimator with the source.

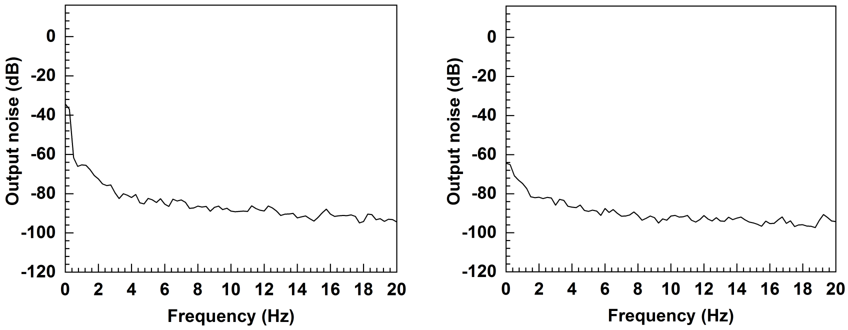

FIGURE 5.23: Comparison of noise spectrum in the frequency range of DC-20 Hz. CFDR1200 (left panel) and DRS 1000 (right panel).

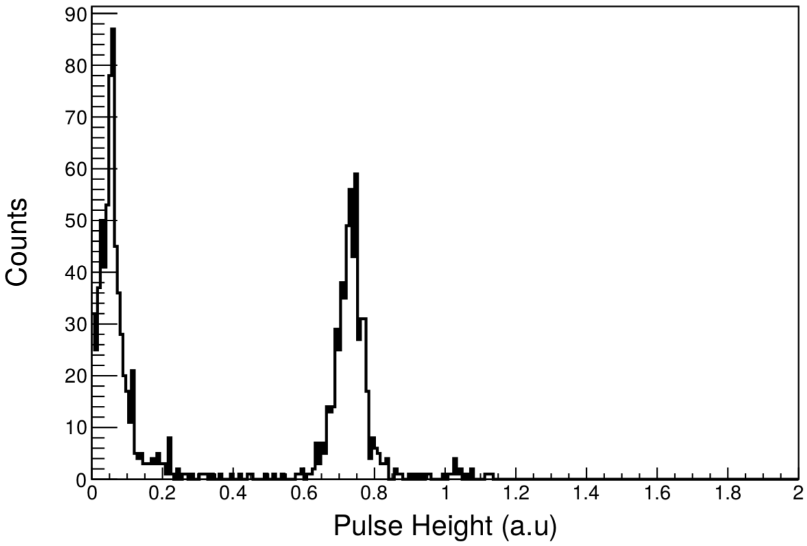

FIGURE 5.24: Pulse height spectra obtained with alpha source at 22 mK at DRS 1000.

5.8.1 Summary

A thermal model for simulating thermal response of bolometer using Mathematica is formulated. A pulse height analysis program for analyzing bolometer signal using ROOT and C++ is developed. An electronics readout and DAQ system employing LabView software is setup for bolometer R&D and tested with a sapphire bolometer. Impact of various noise sources on the performance of the bolometer in the CFDR system inclusive of control, diagnostic thermometry and NI PXI DAQ. It is shown that the presence of ground loops can worsen the performance of bolometer by $\sim$ 80%. Further, the noise pickup from vacuum pumps and vacuum gauge readout units also introduces thermal load on the NTD Ge sensor. The first test of a cryogenic sapphire bolometer with indigenously made NTD Ge sensor is carried out. Response of the sapphire bolometer is studied with phonon pulses and a energy resolution of 15 keV ± 3 keV is obtained in the temperature range of 15 – 25 mK. Compared to CUORE TeO_2 bolometer, this needs to be improved by a factor of 5. The energy resolution of the sapphire bolometer with a Sn of mass ~ 0.6 g does not show appreciable change below 3 MeV. The spectrum of alpha particles is also measured with the cryogenic bolometer. This work provides key inputs for the fabrication of tin superconducting bolometers to be used in the *TinTin* experiment.

CHAPTER 6

Summary and future outlook

6.1 Summary

Double beta decay (DBD) is a second order spontaneous weak nuclear transition in which two neutrons of an even-even nuclei simultaneously decays into two protons by emitting two electrons along with two antineutrinos. Since the neutrino is a neutral spin half fermion and has mass, it can either be a Majorana particle (neutrino is it's own antiparticle) or Dirac particle (neutrino and antineutrino are distinguishable). If the neutrionos are Majorana in nature, then there is a finite probability that the neutrinos are virtually annihilated in the DBD process and only two electrons are emitted in the final state resulting a neutrinoless double beta decay (NDBD). This process violates lepton number conservation by two units ($\Delta L = 2$). Hence, if observed, apart from conclusively establishing Majorana nature of neutrinos NDBD will pave an way to new physics beyond the standard model of particle physics and can contribute in understanding the matter-antimatter asymmetry observed in the universe. Furthermore, the half-life of this process would provide an measurement of the absolute effective electron neutrino mass.

DBD have been observed in 12 nuclei out of 35 naturally occurring potential candidates with half-lives ranging from 10^{18} to 10^{24} year. In contrast, the NDBD is not yet observed. The half-life of the NDBD process is related to the nuclear transition matrix element which involves large uncertainties. Hence, it is important to pursue NDBD experiment in different nucleus. Many experiments are ongoing worldwide in search of this rare decay in different nuclei using different detection techniques. Experimentally, a sharp peak at the Q value along with a continuum background arising from the DBD events would signify a NDBD event. A large mass detector having good energy resolution and good efficiency is desirable. In addition, an extremely low background environment (0.01 counts keV^{-1}kg^{-1}year^{-1}) and a long runtime (few years) is necessary to achieve a reasonable sensitivity. Cryogenic bolometer is a particle detector in which the energy deposition due to an impinging radiation is measured in terms of temperature rise. Insulators and superconductors are ideal as bolometer material owing to small specific heat at low temperatures. Since the bolometer detects phonon signal it is possible to obtain very good energy resolution ($< 0.1\%$) and almost 100% efficiency which makes it a suitable detector for NDBD experiment. Also, if a bolometer is made from a material containing the NDBD isotope then a large mass detector can be made by employing arrays of bolometers to increase the sensitivity.

Till date, the best achieved limit on the half life is reported by KamlandZen collaboration to be $T_{1/2} > 1.07 \times 10^{26}$ year at 90% C.L. for ^{136}Xe. CUORE collaboration have reported a half-life limit of $T_{1/2} > 1.5 \times 10^{25}$ year at 90% C.L. on ^{130}Te using a TeO_2 bolometer of mass $\sim$ 1 ton. Motivated by it's importance, a NDBD experiment on ^{124}Sn (*Tin.Tin*) has been initiated in India. Reasonably high Q value of 2292.6±0.39 keV and moderate isotopic abundance of ~5% makes ^{124}Sn a suitable candidate for this experiment. Moreover, tin becomes superconducting at a transition temperature of 3.7 K, a cryogenic tin bolometer can be made having very good energy resolution when operated at temperature ~10 mK. In this thesis R&D for the development of cryogenic bolometer related to the *Tin.Tin* experiment is carried out.

Development of a prototype tin cryogenic bolometer is underway at TIFR, Mumbai. For this purpose, a custom made high cooling power (1.4 mW at 120 mK) cryogen-free dilution refrigerator (CFDR1200) having a large sample space (30×30 mm^2) in the mixing chamber, capable of supporting ~100 kg of mass, is installed. As a part of this thesis, various troubleshooting and repair on the CFDR1200 is performed. Systematic diagnosis and subsequent repair of two major issues, a) A blockage in the secondary impedance b) A leak was developed in the solder joint near the sintered silver heat exchanger to the IVC, is discussed. The *still* was replaced with a new generation *still* having pressure dependent impedances which are less prone to blockage. Detailed cooling power measurements are performed to assess the performance of the CFDR after repair. A cooling power of 1.36 mW at 120 mK is recorded after repair which is close to the factory supplied value of 1.4 mW at 120 mK.

Currently NTD Ge sensor are developed which are to be used as a temperature sensor in the tin bolometer. For this, high purity Ge wafers of 1 mm thick are irradiated from Dhruva reactor BARC, Mumbai. Earlier work has reported NTD Ge sensors with good performance upto 75 mK. In this thesis various improvements in the NTD Ge sensor fabrication process are done. It is shown that chemical etching of the Ge samples prior to irradiation results in reduction of the surface impurity levels by 40-80%. A method of estimating thermal neutron fluence the activity of ^{nat}Zr is discussed. For a particular sample the neutron fluence obtained by this method could be compared with that obtained form ^{124}Sb activity and an agreement within 10% is found. Neutron fluence obtained from ^{nat}Zr or ^{124}Sb activity is found to be more reliable than that obtained from the reactor power. Optical finished mechanical polishing is performed at the final stage i.e., prior to post irradiation chemical etching in order to improve the surface quality of the sensor. NTD Ge sensors of different size are fabricated and characterized. A neutron fluence of 4-5 $\times 10^{18}$ is found to be optimum for use as a bolometer sensor operating at temperature of 10 mK. Sensors of area 3$\times$3 mm^2 are fabricated with wrap around contact. Smaller size sensor (2$\times$2 mm^2 and 1$\times$1 mm^2 area) owing to have less heat capacity addendum is fabricated and tested upto 40 mK and a mott-like behaviour in the investigated temperature is seen. A variation of 15% in T_0 is found in such sensors. The NTD Ge sensor fabricated using improved fabrication method have shown Mott-like behaviour down to 30 mK and a deviation below this is observed. However a finite dR/dT below this temperature makes it useful upto 10 mK with an empirical function.

Polymers are widely used as structural application in cryogenics due to it's strength to weight ratio as compared to metal and reasonable thermal conductivity. In bolometer it commonly used as a support structure material which also acts as weak link between heat bath. Thermal properties of such polymers play important role in designing a bolometer with optimum performance. Little or no data were available at detector operating temperature region. Comparative study on the heat capacity on polymers (Teflon, Torlon 4203 and Torlon 4301) are done in the temperature range of 30-400 mK using relaxation calorimetric technique. The specific heat for Torlon - 4301 has been reported for the first time while the data for Torlon - 4203 and Teflon has been extended down to 30 mK. The results show Teflon has significantly low specific heat as compared to Torlon 4203 and Torlon 4301. Hence, Teflon is preferred as a bolometer support structure material. Torlon would be preferred for application where more mechanical strength is required. Among Torlon, Torlon 4203 has appreciably less heat capacity than Torlon 4301 in the investigated temperature range.

A sapphire bolometer is being studied to understand various systematics affecting the performance of a cryogenic bolometer. Since sapphire has a very high Debye temperature (1042 K) it has tested as a bolometer operating at a relatively higher temperature ($\sim$1.5 K). An understanding of the various systematics affecting the performance of a cryogenic bolometer is essential for making a tin superconducting bolometer. A Mathematica based thermal model for bolometer is formulated. Using this a sapphire bolometer is designed with tiny aradite glue spots acting as weak thermal link between the absorber and the heat bath. Employing LabView software an NI based DAQ is setup with a low noise electronics readout. An output voltage noise Vpp$\sim$10 mV with gain 60 dB is achieved at T<50 mK. A ROOT and C++ based pulse shape analysis program for the bolometer is developed. This thesis reports the first test of a cryogenic sapphire bolometer with indigenously developed NTD Ge sensor in India. The effect of various noise sources and it's influence on the performance of a cryogenic bolometer is assessed. About 20-30 % improvement on the resolution is observed. Systematic study on a cryogenic bolometer working at 10-100 mK is performed. A resolution of $\sim$15 keV is obtained with the phonon pulse. Compared to CUORE about a factor of $\sim$5 improvement is needed. Sapphire bolometer with a 0.6 g Sn sample is studied. No appreciable change is observed for E<3MeV. Alpha spectrum with a cryogenic bolometer with the indigenously made NTD Ge sensor is measured.

6.2 Future outlook

Thermal properties of NTD Ge have a key role in understanding the performance of cryogenic bolometers. The energy resolution and the decay time of a bolometer depends on the total heat capacity of the detector system. The electronic heat capacity arising from the dopant in NTD Ge contributes significantly to the total heat capacity for small size (few g) bolometers. E. Olivieri et al. [17] have observed a metal like behavior of a NTD Ge having carrier density close to the metal-insulator transition region and reported the temperature dependence of heat capacity for the same in the temperature range of 20–80 mK. Shklovskii et.al predicts a dependence of Sommerfeld constant (γ) on carrier concentration (N_C) as $\gamma \propto N_C^{1/3}$. However, no experimental evidence has been reported yet. NTD Ge samples with a wide range of carrier density ranging from 3.8×10^{16} to 32.9×10^{16} have been made during the R&D of Tin.Tin NTD Ge sensor. A measurement of heat capacity of NTD Ge samples with different dopant density would be beneficial for bolometer development employing NTD Ge as a temperature sensor.

The energy resolution obtained using heater pulse needs to be improved atleast by a factor of 5. Various factors affecting the bolometer resolution needs to be investigated. Currently, the most dominant contribution comes from the vibrational noise caused due to the PT, which has been reduced to the extend possible. Further reduction can be done using the following techniques.

- Attaching a load ($\sim$ 50 kg of lead) on the mixing chamber for dampening the vibration.
- Mounting the bolometer on a passive vibration isolation platform [134].
- Employing a mass-spring vibration isolation system as discussed in Ref. [135].
- In the current configuration the PT is rigidly mounted on the plates at the room temperature, 40 K, and 3 K stages. The PT can be lifted a few cm and placed on the room temperature plate with edge welded below and supported from the celling. The the 40 K and 3 K

stage can then be connected with high conductivity copper braids for thermalization.

Apart form this the electronic noise can be improved by employing a preamplifier stage at 50 K stage. Development of such a preamplifier along with a two stage low noise amplifier working at room temperature is in progress. Also, an optimal filtering technique can be incorporated in the pulse analysis program for improving the energy resolution.

Tests with beta or gamma source needs to be done for better energy calibration. A two stage bolometer (one top of the other) can be made for reducing the cosmic muon background by implementing an anti-coincidence between the two detectors.

A finite size (few g) tin bolometer needs to be made and the effect on the energy resolution due to trapped energy in the quasiparticle of super conducting tin needs to be investigated.

Bibliography

[1] R. Wendell et al. “Atmospheric neutrino oscillation analysis with subleading effects in Super-Kamiokande I, II, and III”. In: *Phys. Rev. D* 81 (9 2010), p. 092004. DOI: `10.1103/PhysRevD.81.092004`.

[2] B. Aharmim et al. “Combined analysis of all three phases of solar neutrino data from the Sudbury Neutrino Observatory”. In: *Phys. Rev. C* 88 (2 2013), p. 025501. DOI: `10.1103/PhysRevC.88.025501`.

[3] Frank T. Avignone, Steven R. Elliott, and Jonathan Engel. “Double beta decay, Majorana neutrinos, and neutrino mass”. In: *Rev. Mod. Phys.* 80 (2 2008), pp. 481–516. DOI: `10.1103/RevModPhys.80.481`.

[4] Ruben Saakyan. “Two-Neutrino Double-Beta Decay”. In: *Annual Review of Nuclear and Particle Science* 63.1 (2013), pp. 503–529.

DOI: `10.1146/annurev-nucl-102711-094904`. eprint: `https://doi.org/10.1146/annurev-nucl-102711-094904`.

[5] A. Gando et al. “Search for Majorana Neutrinos Near the Inverted Mass Hierarchy Region with KamLAND-Zen”. In: *Phys. Rev. Lett.* 117 (8 2016), p. 082503. DOI: `10.1103/PhysRevLett.117.082503`.

[6] M. Agostini et al. “Improved Limit on Neutrinoless Double-β Decay of ^{76}Ge from GERDA Phase II”. In: *Phys. Rev. Lett.* 120 (13 2018), p. 132503. DOI: `10.1103/PhysRevLett.120.132503`.

[7] C. Alduino et al. “First Results from CUORE: A Search for Lepton Number Violation via $0\nu\beta\beta$ Decay of ^{130}Te”. In: *Phys. Rev. Lett.* 120 (13 2018), p. 132501. DOI: `10.1103/PhysRevLett.120.132501`.

[8] V. Nanal. “Search for neutrinoless double beta decay in 124Sn”. In: *EPJ Web of Conferences* 66 (2014), p. 08005. DOI: `10.1051/epjconf/20146608005`.

[9] A. Kumar et al. “Invited review: Physics potential of the ICAL detector at the India-based Neutrino Observatory (INO)”. In: *Pramana* 88.5 (2017), p. 79. ISSN: 0973-7111. DOI: `10.1007/s12043-017-1373-4`.

[10] M. K. Bacrania et al. “Large-Area Microcalorimeter Detectors for Ultra-High-Resolution X-Ray and Gamma-Ray Spectroscopy”. In: *IEEE Transactions on Nuclear Science* 56.4 (2009), pp. 2299–2302. ISSN: 0018-9499. DOI: `10.1109/TNS.2009.2022754`.

[11] D. McCammon. “Thermal Equilibrium Calorimeters – An Introduction”. In: *Cryogenic Particle Detection*. Ed. by Christian Enss. Berlin, Heidelberg: Springer Berlin Heidelberg, 2005, pp. 1–34. DOI: `10.1007/10933596_1`.

[12] A. Garai et al. “Development of NTD Ge Sensors for Superconducting Bolometer”. In: *Journal of Low Temperature Physics* 184.3 (2016), pp. 609–614. ISSN: 1573-7357. DOI: `10.1007/s10909-015-1379-6`.

[13] V. Singh et al. “Specific heat of Teflon, Torlon 4203 and Torlon 4301 in the range of 30–400mK”. In: *Cryogenics* 67 (2015), pp. 15 –18. ISSN: 0011-2275. DOI: `https://doi.org/10.1016/j.cryogenics.2015.01.001`.

[14] V. Singh et al. “Cryogen-free dilution refrigerator for bolometric search of neutrinoless double beta decay ($0\nu\beta\beta$) in ^{124}Sn”. In: *Pramana* 81.4 (2013), pp. 719–725. ISSN: 0973-7111. DOI: `10.1007/s12043-013-0601-9`.

[15] S. Mathimalar et al. “Development of NTD Ge sensors for low temperature thermometry”. In: *2014 11th International Workshop on Low Temperature Electronics (WOLTE)*. 2014, pp. 13–16. DOI: `10.1109/WOLTE.2014.6881014`.

[16] S. Mathimalar et al. “Study of radioactive impurities in neutron transmutation doped germanium”. In: *Nuclear Instruments and Methods in Physics Research Section A: Accelerators, Spectrometers, Detectors and Associated Equipment* 774 (2015), pp. 68 –73.

ISSN: 0168-9002. DOI: `https://doi.org/10.1016/j.nima.2014.11.056`.

[17] E. Olivieri et al. “Excess Heat Capacity in NTD Ge Thermistors”. In: *Journal of Low Temperature Physics* 143.3 (2006), pp. 153–162. ISSN: 1573-7357. DOI: `10.1007/s10909-006-9214-8`.

[18] *National Instruments*. `http://www.ni.com/en-in.html`. Accessed: 2019-01-16.

[19] D. McCammon. “Semiconductor Thermistors”. In: *Cryogenic Particle Detection*. Ed. by Christian Enss. Berlin, Heidelberg: Springer Berlin Heidelberg, 2005, pp. 35–62. ISBN: 978-3-540-31478-3. DOI: `10.1007/10933596_2`.

[20] R. Bachmann et al. “Heat Capacity Measurements on Small Samples at Low Temperatures”. In: *Review of Scientific Instruments* 43.2 (1972), pp. 205–214. DOI: `10.1063/1.1685596`. eprint: `https://doi.org/10.1063/1.1685596`.

[21] *WOLFRAM MATHEMATICA*. `https://www.wolfram.com/mathematica/`. Accessed: 2019-01-16.

[22] A von Kienlin et al. “High resolution detection of energetic heavy ions with a calorimetric low temperature detector”. In: *Nuclear Instruments and Methods in Physics Research Section A: Accelerators, Spectrometers, Detectors and Associated Equipment* 368.3 (1996), pp. 815 –818. ISSN: 0168-9002. DOI: `https://doi.org/10.1016/0168-9002(95)00562-5`.

[23] Abraham. Savitzky and M. J. E. Golay. “Smoothing and Differentiation of Data by Simplified Least Squares Procedures.” In: *Analytical Chemistry* 36.8 (1964), pp. 1627–1639. DOI: `10.1021/ac60214a047`. eprint: `https://doi.org/10.1021/ac60214a047`.

[24] Peter A. Gorry. “General least-squares smoothing and differentiation by the convolution (Savitzky-Golay) method”. In: *Analytical Chemistry* 62.6 (1990), pp. 570–573. DOI: `10.1021/ac00205a007`. eprint: `https://doi.org/10.1021/ac00205a007`.

[25] H. R. Naren et al. “Setting up of a MicroKelvin refrigerator facility at TIFR”. In: *AIP Conference Proceedings* 1447.1 (2012), pp. 503–504. DOI: `10.1063/1.4710099`. eprint: `https://aip.scitation.org/doi/pdf/10.1063/1.4710099`.

[26] *National Nuclear Data Center*. `https://www.nndc.bnl.gov/`. Accessed: 2019-01-16.

[27] G. Forster et al. “Calorimeters with proximity-effect thermometers and lead and tin absorbers”. In: *Journal of Low Temperature Physics* 93.3 (1993), pp. 219–224. ISSN: 1573-7357. DOI: `10.1007/BF00693423`.

[28] W. Pauli. “Dear radioactive ladies and gentlemen”. In: *Phys. Today* 31N9 (1978), p. 27.

[29] E. Fermi. “Versuch einer Theorie der β-Strahlen. I”. In: *Zeitschrift für Physik* 88.3 (1934), pp. 161–177. ISSN: 0044-3328. DOI: `10.1007/BF01351864`.

[30] C. L. Cowan et al. “Detection of the Free Neutrino: a Confirmation”. In: *Science* 124.3212 (1956), pp. 103–104. ISSN: 0036-8075. DOI: `10.1126/science.124.3212.103`. eprint: `http://science.sciencemag.org/content/124/3212/103.full.pdf`.

[31] Pablo F. de Salas et al. “Neutrino Mass Ordering from Oscillations and Beyond: 2018 Status and Future Prospects”. In: *Frontiers in Astronomy and Space Sciences* 5 (2018), p. 36. ISSN: 2296-987X. DOI: `10.3389/fspas.2018.00036`.

[32] M. A. Acero et al. “New constraints on oscillation parameters from ν_e appearance and ν_μ disappearance in the NOvA experiment”. In: *Phys. Rev. D* 98 (3 2018), p. 032012. DOI: `10.1103/PhysRevD.98.032012`.

[33] K. Abe et al. “Measurement of neutrino and antineutrino oscillations by the T2K experiment including a new additional sample of ν_e interactions at the far detector”. In: *Phys. Rev. D* 96 (9 2017), p. 092006. DOI: `10.1103/PhysRevD.96.092006`.

[34] Yu-Feng Li et al. “Unambiguous determination of the neutrino mass hierarchy using reactor neutrinos”. In: *Phys. Rev. D* 88 (1 2013), p. 013008. DOI: `10.1103/PhysRevD.88.013008`.

[35] M. Goeppert-Mayer. “Double Beta-Disintegration”. In: *Phys. Rev.* 48 (6 1935), pp. 512–516. DOI: `10.1103/PhysRev.48.512`.

[36] Vandana Nanal. “Is neutrino its own antiparticle?” In: *CURRENT SCIENCE* 112.7 (2017), p. 10.

[37] Ettore Majorana. “Teoria simmetrica dell’elettrone e del positrone”. In: *Nuovo Cimento* 14.4 (1937), p. 171. ISSN: 1827-6121. DOI: `10.1007/BF02961314`.

[38] Giulio Racah. “Sulla Simmetria Tra Particelle e Antiparticelle”. In: *Il Nuovo Cimento* 14.7 (1937), p. 322. ISSN: 1827-6121. DOI: `10.1007/BF02961321`.

[39] W. H. Furry. “On Transition Probabilities in Double Beta-Disintegration”. In: *Phys. Rev.* 56 (12 1939), pp. 1184–1193. DOI: `10.1103/PhysRev.56.1184`.

[40] H. Primakoff. “Angular Correlation of Electrons in Double Beta-Decay”. In: *Phys. Rev.* 85 (5 1952), pp. 888–890. DOI: `10.1103/PhysRev.85.888`.

[41] J D Vergados, H Ejiri, and F Simkovic. “Theory of neutrinoless double-beta decay”. In: *Reports on Progress in Physics* 75.10 (2012), p. 106301.

[42] VLADIMIR I TRETYAK and YURI G ZDESENKO. “TABLES OF DOUBLE BETA DECAY DATA-AN UPDATE”. In: *Atomic Data and Nuclear Data Tables* 80.1 (2002), pp. 83 –116. ISSN: 0092-640X. DOI: `https://doi.org/10.1006/adnd.2001.0873`.

[43] Mark G. Inghram and John H. Reynolds. “Double Beta-Decay of Te^{130}”. In: *Phys. Rev.* 78 (6 1950), pp. 822–823. DOI: `10.1103/PhysRev.78.822.2`.

[44] S. R. Elliott, A. A. Hahn, and M. K. Moe. “Direct evidence for two-neutrino double-beta decay in ^{82}Se”. In: *Phys. Rev. Lett.* 59 (18 1987), pp. 2020–2023. DOI: `10.1103/PhysRevLett.59.2020`.

[45] Werner Maneschg. “Review of neutrinoless double beta decay experiments: Present status and near future”. In: *Nuclear and Particle Physics Proceedings* 260 (2015). The 13th International Workshop on Tau Lepton Physics, pp. 188 –193. ISSN: 2405-6014. DOI: `https://doi.org/10.1016/j.nuclphysbps.2015.02.039`.

[46] C. E. Aalseth et al. “Search for Neutrinoless Double-β Decay in ^{76}Ge with the Majorana Demonstrator”. In: *Phys. Rev. Lett.* 120 (13 2018), p. 132502. DOI: `10.1103/PhysRevLett.120.132502`.

[47] J. B. Albert et al. “Search for Neutrinoless Double-Beta Decay with the Upgraded EXO-200 Detector”. In: *Phys. Rev. Lett.* 120 (7 2018), p. 072701. DOI: `10.1103/PhysRevLett.120.072701`.

[48] S. P. Langley. “The Bolometer and Radiant Energy”. In: *Proceedings of the American Academy of Arts and Sciences* 16 (1880), pp. 342–358. ISSN: 01999818. DOI: `10.2307/25138616`.

[49] F. SIMON. “Application of Low Temperature Calorimetry to Radioactive Measurements”. In: *Nature* 135 (1935), p. 763. DOI: `10.2307/25138616`.

[50] D. H. Andrews, R. D. Fowler, and M. C. Williams. “The Effect of Alpha-particles on a Superconductor”. In: *Phys. Rev.* 76 (1 1949), pp. 154–155. DOI: `10.1103/PhysRev.76.154.2`.

[51] N. Coron, G. Dambier, and J. Leblanc. "A New Type of Helium-Cooled Bolometer". In: *Infrared Detection Techniques for Space Research*. Ed. by V. Manno and J. Ring. Dordrecht: Springer Netherlands, 1972, pp. 121–131. ISBN: 978-94-010-2885-1. DOI: `10.1007/978-94-010-2885-1_15`.

[52] T.O. Niinikoski and F. Udo. "Cryogenic detection of neutrinos". In: *CERN/NP Internal Report*. 74-6. 1974.

[53] E. Fiorini and T.O. Niinikoski. "Low-temperature calorimetry for rare decays". In: *Nuclear Instruments and Methods in Physics Research* 224.1 (1984), pp. 83 –88. ISSN: 0167-5087. DOI: `10.1016/0167-5087(84)90449-6`.

[54] Frank Pobell. *Matter and Methods at Low Temperatures*. Springer, Berlin, Heidelberg, 2007. DOI: `/10.1007/978-3-540-46360-3`.

[55] K.D. Irwin and G.C. Hilton. "Transition-Edge Sensors". In: *Cryogenic Particle Detection*. Ed. by Christian Enss. Berlin, Heidelberg: Springer Berlin Heidelberg, 2005, pp. 63–150. ISBN: 978-3-540-31478-3. DOI: `10.1007/10933596_3`.

[56] Boris I. Shklovskii and Alex L. Efros. "Variable-Range Hopping Conduction". In: *Electronic Properties of Doped Semiconductors*. Berlin, Heidelberg: Springer Berlin Heidelberg, 1984, pp. 202–227. ISBN: 978-3-662-02403-4. DOI: `10.1007/978-3-662-02403-4_9`.

[57] E. E. Haller et al. "NTD Germanium: A Novel Material for Low Temperature Bolometers". In: *Neutron Transmutation Doping of*

Semiconductor Materials. Ed. by Robert D. Larrabee. Boston, MA: Springer US, 1984, pp. 21–36. DOI: `10.1007/978-1-4613-2695-3_2`.

[58] A. Fleischmann, C. Enss, and G.M. Seidel. “Metallic Magnetic Calorimeters”. In: *Cryogenic Particle Detection*. Ed. by Christian Enss. Berlin, Heidelberg: Springer Berlin Heidelberg, 2005, pp. 151–216. ISBN: 978-3-540-31478-3. DOI: `10.1007/10933596_4`.

[59] P. Lerch and A. Zehnder. “Quantum Giaever Detectors: STJ’s”. In: *Cryogenic Particle Detection*. Ed. by Christian Enss. Berlin, Heidelberg: Springer Berlin Heidelberg, 2005, pp. 217–266. ISBN: 978-3-540-31478-3. DOI: `10.1007/10933596_5`.

[60] T. C. P. Chui et al. “Temperature fluctuations in the canonical ensemble”. In: *Phys. Rev. Lett.* 69 (21 1992), pp. 3005–3008. DOI: `10.1103/PhysRevLett.69.3005`.

[61] John C. Mather. “Bolometer noise: nonequilibrium theory”. In: *Appl. Opt.* 21.6 (1982), pp. 1125–1129. DOI: `10.1364/AO.21.001125`.

[62] R. Maisonobe et al. “Vibration decoupling system for massive bolometers in dry cryostats”. In: *Journal of Instrumentation* 13.08 (2018), T08009.

[63] Christian Enss (ed.) “Cryogenic Particle Detection”. In: *Topics in Applied Physics* 99 (2005). ISSN: 978-3-540-20113-7. DOI: `10.1007/b12169`.

[64] B. Sadoulet. “Science with low temperature detectors”. In: *Nuclear Instruments and Methods in Physics Research Section A: Accelerators, Spectrometers, Detectors and Associated Equipment* 370.1 (1996). Proceedings of the Sixth International Workshop on Low Temperature Detectors, pp. 1 –7. ISSN: 0168-9002. DOI: `https://doi.org/10.1016/0168-9002(95)01030-0`.

[65] Philippe Camus, Alexandre Juillard, and Alessandro Monfardini (eds.) “Proceedings, 16th International Workshop on Low Temperature Detectors (LTD 16)”. In: *J. Low. Temp. Phys.* 184.1-4 (2016), pp.1–978.

[66] S. Pirro and P. Mauskopf. “Advances in Bolometer Technology for Fundamental Physics”. In: *Annual Review of Nuclear and Particle Science* 67.1 (2017), pp. 161–181. DOI: `10.1146/annurev-nucl-101916-123130`. eprint: `https://doi.org/10.1146/annurev-nucl-101916-123130`.

[67] L Cardani et al. “Performance of a large TeO_2 crystal as a cryogenic bolometer in searching for neutrinoless double beta decay”. In: *Journal of Instrumentation* 7.01 (2012), P01020.

[68] Jules Gascon. “Direct dark matter searches review”. In: *EPJ Web of Conferences* 95 (2015), p. 02004. DOI: `10.1051/epjconf/20149502004`.

[69] R. Agnese et al. “Search for Low-Mass Weakly Interacting Massive Particles with SuperCDMS”. In: *Phys. Rev. Lett.* 112 (24 2014), p. 241302. DOI: `10.1103/PhysRevLett.112.241302`.

[70] E. Armengaud et al. “Performance of the EDELWEISS-III experiment for direct dark matter searches”. In: *Journal of Instrumentation* 12.08 (2017), P08010. DOI: `10.1088/1748-0221/12/08/P08010`.

[71] G. Angloher et al. “Results on light dark matter particles with a low-threshold CRESST-II detector”. In: *The European Physical Journal C* 76.1 (2016), p. 25. ISSN: 1434-6052. DOI: `10.1140/epjc/s10052-016-3877-3`.

[72] F. Reindl et al. “Results of the first NaI scintillating calorimeter prototypes by COSINUS”. In: *15th International Conference on Topics in Astroparticle and Underground Physics (TAUP 2017) Sudbury, Ontario, Canada, July 24-28, 2017*. 2017. arXiv: `1711.01482 [astro-ph.IM]`.

[73] D.R. Artusa et al. “Enriched TeO_2 bolometers with active particle discrimination: Towards the CUPID experiment”. In: *Physics Letters B* 767 (2017), pp. 321 –329. ISSN: 0370-2693. DOI: `https://doi.org/10.1016/j.physletb.2017.02.011`.

[74] J. W. Beeman et al. “The LUCIFER Project: Achievements and Near Future Prospects”. In: *Journal of Low Temperature Physics* 184.3 (2016), pp. 852–858. ISSN: 1573-7357. DOI: `10.1007/s10909-015-1423-6`.

[75] E. Armengaud et al. “Development and underground test of radiopure ZnMoO 4 scintillating bolometers for the LUMINEU $0\nu\beta\beta$

project". In: *Journal of Instrumentation* 10.05 (2015), P05007. doi: `10.1088/1748-0221/10/05/P05007`.

[76] I Kim et al. "Application of metallic magnetic calorimeter in rare event search". In: *Superconductor Science and Technology* 30.9 (2017), p. 094005.

[77] Garai A et al. "A pulse height analysis technique for cryogenic bolometers". In: *Proceedings of the DAE-BRNS International Symp. on Nucl. Phys.* Vol. 63. 2018, p. 1140.

[78] Garai A et al. "Study of the effect of external noise pickups on the performance of a cryogenic bolometer". In: *(Submitted to JINST)*.

[79] H. London, G. R. Clarke, and Eric Mendoza. "Osmotic Pressure of He^3 in Liquid He^4, with Proposals for a Refrigerator to Work below 1°K". In: *Phys. Rev.* 128 (5 1962), pp. 1992–2005. doi: `10.1103/PhysRev.128.1992`.

[80] London H. "Proc. Int. Conf. on Low Temp. Phys." In: *Clarendon Press Laboratory*. Dordrecht: Oxford, 1951, p. 157.

[81] P. Das, R. Bruyn de Ouboter, and K. W. Taconis. "A Realization of a London-Clarke-Mendoza Type Refrigerator". In: *Low Temperature Physics LT9*. Ed. by J. G. Daunt et al. Boston, MA: Springer US, 1965, pp. 1253–1255. isbn: 978-1-4899-6443-4.

[82] G. Frossati. "Experimental techniques: Methods for cooling below 300 mK". In: *Journal of Low Temperature Physics* 87.3 (1992), pp. 595–633. issn: 1573-7357. doi: `10.1007/BF00114918`.

[83] K. Uhlig and W. Hehn. “3He/4He dilution refrigerator with Gifford-McMahon precooling”. In: *Cryogenics* 33.11 (1993), pp. 1028 – 1031. ISSN: 0011-2275. DOI: `https://doi.org/10.1016/0011-2275(93)90204-2`.

[84] Kurt Uhlig. “3He/4He dilution refrigerator with pulse-tube refrigerator precooling”. In: *Cryogenics* 42.2 (2002), pp. 73 –77. ISSN: 0011-2275. DOI: `https://doi.org/10.1016/S0011-2275(02)00002-4`.

[85] C. Ligi et al. “The CUORE Cryostat: A 1-Ton Scale Setup for Bolometric Detectors”. In: *Journal of Low Temperature Physics* 184.3 (2016), pp. 590–596. ISSN: 1573-7357. DOI: `10.1007/s10909-015-1389-4`.

[86] G Batey, A J Matthews, and M Patton. “A new ultra-low-temperature cryogen-free experimental platform”. In: *Journal of Physics: Conference Series* 568.3 (2014), p. 032014. DOI: `10.1088/1742-6596/568/3/032014`.

[87] K Uhlig. “Cryogen-free dilution refrigerators”. In: *Journal of Physics: Conference Series* 400.5 (2012), p. 052039.

[88] E. Olivieri et al. “Vibrations on pulse tube based Dry Dilution Refrigerators for low noise measurements”. In: *Nuclear Instruments and Methods in Physics Research Section A: Accelerators, Spectrometers, Detectors and Associated Equipment* 858 (2017), pp. 73 –79. ISSN: 0168-9002. DOI: `https://doi.org/10.1016/j.nima.2017.03.045`.

[89] Rachpon Kalra et al. "Vibration-induced electrical noise in a cryogen-free dilution refrigerator: Characterization, mitigation, and impact on qubit coherence". In: *Review of Scientific Instruments* 87.7 (2016), p. 073905. DOI: `10.1063/1.4959153`. eprint: `https://aip.scitation.org/doi/pdf/10.1063/1.4959153`.

[90] S Pirro et al. "Vibrational and thermal noise reduction for cryogenic detectors". In: *Nuclear Instruments and Methods in Physics Research Section A: Accelerators, Spectrometers, Detectors and Associated Equipment* 444.1 (2000), pp. 331 –335. ISSN: 0168-9002. DOI: `https://doi.org/10.1016/S0168-9002(99)01376-5`.

[91] S. Pirro. "Further developments in mechanical decoupling of large thermal detectors". In: *Nuclear Instruments and Methods in Physics Research Section A: Accelerators, Spectrometers, Detectors and Associated Equipment* 559.2 (2006). Proceedings of the 11th International Workshop on Low Temperature Detectors, pp. 672 –674. ISSN: 0168-9002. DOI: `https://doi.org/10.1016/j.nima.2005.12.197`.

[92] C. Lee et al. "Vibration isolation system for cryogenic phonon-scintillation calorimeters". In: *Journal of Instrumentation* 12.02 (2017), pp. C02057–C02057. DOI: `10.1088/1748-0221/12/02/c02057`.

[93] A. M. J. den Haan et al. "Atomic resolution scanning tunneling microscopy in a cryogen free dilution refrigerator at 15 mK". In: *Review of Scientific Instruments* 85.3 (2014), p. 035112. DOI: `10.`

1063/1.4868684. eprint: https://doi.org/10.1063/1.4868684.

[94] S. Caparrelli et al. "Vibration-free cryostat for low-noise applications of a pulse tube cryocooler". In: *Review of Scientific Instruments* 77.9 (2006), p. 095102. DOI: 10.1063/1.2349609. eprint: https://doi.org/10.1063/1.2349609.

[95] Yuki Ikushima et al. "Ultra-low-vibration pulse-tube cryocooler system âĂŞ cooling capacity and vibration". In: *Cryogenics* 48.9 (2008), pp. 406 –412. ISSN: 0011-2275. DOI: https://doi.org/10.1016/j.cryogenics.2008.04.001.

[96] M. Pelliccione et al. "Design of a scanning gate microscope for mesoscopic electron systems in a cryogen-free dilution refrigerator". In: *Review of Scientific Instruments* 84.3 (2013), p. 033703. DOI: 10.1063/1.4794767. eprint: https://doi.org/10.1063/1.4794767.

[97] *Emerson & Cuming Microwave Products*. http://www.eccosorb.com/products-eccosorb-high-loss-absorbers.html. Accessed: 2019-02-03.

[98] *RV-Elektroniikka Oy PICOWATT*. http://www.picowatt.fi/avs47b/avs47b.html.

[99] E.E. Haller. "Physics and design of advanced IR bolometers and photoconductors". In: *Infrared Physics* 25.1 (1985), pp. 257 –266. ISSN: 0020-0891. DOI: https://doi.org/10.1016/0020-0891(85)90088-0.

[100] R.B Firestone et al. In: *The 8th edition of the Table of Isotopes*. Vol. 1. Hungary: Springer, 1997.

[101] A. L. Woodcraft et al. “Hopping Conduction in NTD Germanium: Comparison Between Measurement and Theory”. In: *Journal of Low Temperature Physics* 134.3 (2004), pp. 925–944. ISSN: 1573-7357. DOI: `10.1023/B:JOLT.0000013209.08494.01`.

[102] Sheng S. Li. “Metal–Semiconductor Contacts”. In: *Semiconductor Physical Electronics*. Ed. by Sheng S. Li. New York, NY: Springer New York, 2006, pp. 284–333. ISBN: 978-0-387-37766-7. DOI: `10.1007/0-387-37766-2_10`.

[103] Jeffrey W. Beeman William L. Hansen V. I. Ozhogin Eugene E. Haller K. M. Itoh. *Neutron transmutation doped natural and isotopically engineered germanium thermistors*. 1994. DOI: `10.1117/12.176771`.

[104] N. Dokania et al. “Characterization and modeling of a low background HPGe detector”. In: *Nuclear Instruments and Methods in Physics Research Section A: Accelerators, Spectrometers, Detectors and Associated Equipment* 745 (2014), pp. 119 –127. ISSN: 0168-9002. DOI: `https://doi.org/10.1016/j.nima.2014.01.064`.

[105] *University Wafer*. https://order.universitywafer.com/.

[106] *Umicore Electro-Optic Materials*. https://eom.umicore.com/en/.

[107] Gupta G et al. “Estimation of thermal neutron flux from natZr activity”. In: *Proceedings of the DAE-BRNS International Symp. on Nucl. Phys.* 61 (2015), p. 914.

[108] M. Kim and G. Kang. “Precise Control of Neutron Irradiation Fluence in the Neutron Transmutation Doping Process at HANARO Using SPND and Zirconium Foils”. In: *IEEE Transactions on Nuclear Science* 63.3 (2016), pp. 1625–1629. ISSN: 0018-9499. DOI: `10.1109/TNS.2016.2556718`.

[109] P. M. Prajapati et al. “Measurement of Neutron-Induced Reaction Cross Sections in Zirconium Isotopes at Thermal, 2.45 MeV and 9.85 MeV Energies”. In: *Nuclear Science and Engineering* 171.1 (2012), pp. 78–84. DOI: `10.13182/NSE11-02`. eprint: `https://doi.org/10.13182/NSE11-02`.

[110] S. Mathimalar et al. “Characterization of Neutron Transmutation Doped (NTD) Ge for low temperature sensor development”. In: *Nuclear Instruments and Methods in Physics Research Section B: Beam Interactions with Materials and Atoms* 345 (2015), pp. 33 –36. ISSN: 0168-583X. DOI: `https://doi.org/10.1016/j.nimb.2014.12.020`.

[111] *RDM-Apps*. `https://www.rdm-apps.com/`. Accessed: 2019-02-20.

[112] Ning Wang et al. “Electrical and thermal properties of neutron-transmutation-doped Ge at 20 mK”. In: *Phys. Rev. B* 41 (6 1990), pp. 3761–3768. DOI: `10.1103/PhysRevB.41.3761`.

[113] C Arnaboldi et al. “CUORE: a cryogenic underground observatory for rare events”. In: *Nuclear Instruments and Methods in Physics Research Section A: Accelerators, Spectrometers, Detectors and Associated Equipment* 518.3 (2004), pp. 775 –798. ISSN: 0168-9002. DOI: `https://doi.org/10.1016/j.nima.2003.07.067`.

[114] F. Ferroni. “LUCIFER: A new technique for Double Beta Decay”. In: *Il Nuovo Cimento* 33.5 (2010), pp. 27–34. ISSN: 20374909. DOI: `10.1393/ncc/i2011-10696-1`.

[115] J.W. Beeman et al. “A next-generation neutrinoless double beta decay experiment based on $ZnMoO_4$ scintillating bolometers”. In: *Physics Letters B* 710.2 (2012), pp. 318 –323. ISSN: 0370-2693. DOI: `https://doi.org/10.1016/j.physletb.2012.03.009`.

[116] H Bhang et al. “AMoRE experiment: a search for neutrinoless double beta decay of100Mo isotope with $^{40}Ca^{100}MoO_4$ cryogenic scintillation detector”. In: *Journal of Physics: Conference Series* 375.4 (2012), p. 042023. DOI: `10.1088/1742-6596/375/1/042023`.

[117] *Torlon Resins Engineering Data Solvay Advanced Polymers*. `https://www.solvay.com/en/products/brands/torlon-paiData-Sheets`. Accessed: 2019-02-03.

[118] James D. Boyer et al. “The low-temperature specific heat of PTFE (Teflon) at pressures to 5.2 kbar”. In: *Journal of Non-Crystalline*

Solids 55.3 (1983), pp. 413 –432. ISSN: 0022-3093. DOI: `https://doi.org/10.1016/0022-3093(83)90046-7`.

[119] M. Barucci et al. "Very-low temperature specific heat of Torlon". In: *Cryogenics* 46.11 (2006), pp. 767 –770. ISSN: 0011-2275. DOI: `https://doi.org/10.1016/j.cryogenics.2006.05.006`.

[120] G. R. Stewart. "Measurement of low-temperature specific heat". In: *Review of Scientific Instruments* 54.1 (1983), pp. 1–11. DOI: `10.1063/1.1137207`. eprint: `https://doi.org/10.1063/1.1137207`.

[121] M. Brando. "Development of a relaxation calorimeter for temperatures between 0.05 and 4 K". In: *Review of Scientific Instruments* 80.9 (2009), p. 095112. DOI: `10.1063/1.3202380`. eprint: `https://doi.org/10.1063/1.3202380`.

[122] V. Singh et al. "Heat Capacity Setup for Superconducting Bolometer Absorbers below 400 mK". In: *Journal of Low Temperature Physics* 175.3 (2014), pp. 604–613. ISSN: 1573-7357. DOI: `10.1007/s10909-013-1081-5`.

[123] Nodar Samkharadze, Ashwani Kumar, and Gábor A. Csáthy. "A New Type of Carbon Resistance Thermometer with Excellent Thermal Contact at Millikelvin Temperatures". In: *Journal of Low Temperature Physics* 160.5 (2010), pp. 246–253. ISSN: 1573-7357. DOI: `10.1007/s10909-010-0192-5`.

[124] R. B. Stephens. “Low-Temperature Specific Heat and Thermal Conductivity of Noncrystalline Dielectric Solids”. In: *Phys. Rev. B* 8 (6 1973), pp. 2896–2905. DOI: `10.1103/PhysRevB.8.2896`.

[125] John P. Shepherd. “Analysis of the lumped τ_2 effect in relaxation calorimetry”. In: *Review of Scientific Instruments* 56.2 (1985), pp. 273–277. DOI: `10.1063/1.1138343`. eprint: `https://doi.org/10.1063/1.1138343`.

[126] P. w. Anderson, B. I. Halperin, and c. M. Varma. “Anomalous low-temperature thermal properties of glasses and spin glasses”. In: *The Philosophical Magazine: A Journal of Theoretical Experimental and Applied Physics* 25.1 (1972), pp. 1–9. DOI: `10.1080/14786437208229210`. eprint: `https://doi.org/10.1080/14786437208229210`.

[127] W. A. Phillips. “Tunneling states in amorphous solids”. In: *Journal of Low Temperature Physics* 7.3 (1972), pp. 351–360. ISSN: 1573-7357. DOI: `10.1007/BF00660072`.

[128] Anjan Bhattacharyya. “A tunnelling-state model for the specific heat capacity and thermal conductivity of amorphous materials at low temperatures”. In: *Contemporary Physics* 22.1 (1981), pp. 117–127. DOI: `10.1080/00107518108231517`. eprint: `https://doi.org/10.1080/00107518108231517`.

[129] R. Viswanathan. “Heat capacity of sapphire between 2 and 10 K by ac technique”. In: *Journal of Applied Physics* 46.9 (1975),

pp. 4086–4087. doi: `10.1063/1.322119`. eprint: `https://doi.org/10.1063/1.322119`.

[130] C. Enss and D. McCammon. "Physical Principles of Low Temperature Detectors: Ultimate Performance Limits and Current Detector Capabilities". In: *Journal of Low Temperature Physics* 151.1 (2008), pp. 5–24. issn: 1573-7357. doi: `10.1007/s10909-007-9611-7`.

[131] K. Alfonso et al. "Search for Neutrinoless Double-Beta Decay of ^{130}Te with CUORE-0". In: *Phys. Rev. Lett.* 115 (10 2015), p. 102502. doi: `10.1103/PhysRevLett.115.102502`.

[132] R. L. Kelley et al. "Development of microcalorimeters for high resolution X-ray spectroscopy". In: *Journal of Low Temperature Physics* 93.3 (1993), pp. 225–230. issn: 1573-7357. doi: `10.1007/BF00693424`.

[133] A. D'Addabbo et al. "An active noise cancellation technique for the CUORE Pulse Tube cryocoolers". In: *Cryogenics* 93 (2018), pp. 56 –65. issn: 0011-2275. doi: `https://doi.org/10.1016/j.cryogenics.2018.05.001`.

[134] *CRYO VIBRATION ISOLATION PLATFORM*. `https://www.janssenprecisionengineering.com/page/cryo-vibration-isolation-platform-cvip/`. Accessed: 2019-02-27.

[135] C. Lee et al. "Vibration isolation system for cryogenic phonon-scintillation calorimeters". In: *Journal of Instrumentation* 12.02

(2017), pp. C02057–C02057. DOI: `10.1088/1748-0221/12/02/c02057`.